CHIRAL INDUCED SPIN SELECTIVITY EFFECT: FUNDAMENTAL STUDIES AND APPLICATIONS

by

Supriya Ghosh

B.Sc., University of Calcutta, 2010

M.Sc., IIT Bombay, 2012

M.Sc., University of Alberta, 2015

Submitted to the Graduate Faculty of the
Dietrich School of Arts and Sciences in partial fulfillment
of the requirements for the degree of
Doctor of Philosophy

University of Pittsburgh

2021

UNIVERSITY OF PITTSBURGH

DIETRICH SCHOOL OF ARTS AND SCIENCES

This dissertation was presented

by

Supriya Ghosh

It was defended on

April 5, 2021

and approved by

Dr. Haitao Liu, Professor, Department of Chemistry

Dr. Sean Garrett-Roe, Associate Professor, Department of Chemistry

Dr. Andrew Gellman, Professor, Chemical Engineering, Carnegie Mellon University

Dissertation Advisor: Dr. David Waldeck, Professor, Department of Chemistry

Copyright © by Supriya Ghosh

2021

CHIRAL INDUCED SPIN SELECTIVITY EFFECT: FUNDAMENTAL STUDIES AND APPLICATIONS

Supriya Ghosh, PhD

University of Pittsburgh, 2021

Since the discovery, chiral induced spin selectivity effect or CISS effect, which refers to the preferential transmission of electron of one spin over another through a chiral molecule/material, has generated significant interest due to its versatile application in different branches of science. Over the years, a large number of theoretical and experimental studies have been performed to understand the mechanism for the CISS effect and also to utilize the effect in different fields of science; such as memory devices, electrocatalytic experiments, chiral separations etc. In this dissertation, fundamental studies of chiral molecules at ferromagnetic interfaces are investigated through surface potential and magnetic measurements. Experiments are also done to study the spin filtering properties of chiral thin films and explore their electrocatalytic activity. In the first study chiral molecule induced magnetization of the superparamagnetic particles was shown. This experiment shows a novel method to create a ferromagnetic domain of 10 nm size from superparamagnetic particles using CISS. In the second study, spin dependent charge penetration into chiral molecules from a ferromagnetic substrate is presented by measuring surface potential using Kelvin probe method. In the third study, spin dependent electron transmission through chiral cobalt oxide thin films was performed by using magnetic conductive AFM and magnetoresistance measurements. In the fourth study the electrocatalytic efficiency for water splitting was studied using chiral and magnetic thin cobalt oxide film. The finding of these

studies serve to advance the CISS field and may help in developing new CISS based spintronics device and electrocatalysts.

TABLE OF CONTENTS

LIST OF TABLES

LIST OF FIGURES

LIST OF EQUATIONS

PREFACE

I am fortunate enough to receive a lot of help and support from so many people in the past few years that has made my dream come to fruition.

First of all, I would like to thank my academic advisor Dr. David Waldeck. He is a brilliant scientist and an exceptional human being. Dr. Waldeck has always supported me and helped me become a better scientist. He has given me the much needed freedom so that I can conduct my research thoroughly. Every time I faced any kind of problem related to my research, he was always there to give me advice. His patience with me has instilled a sense of calmness in my mind that has helped me in a lot of ways during my most vulnerable moments. I am so grateful to have Dr. Waldeck as my advisor. I can't thank him enough for his invaluable presence in my life.

I would also like to thank my committee members Prof. Haitao Liu, Prof. Sean Garrett-Roe, Prof. Andrew Gellman for their valuable time and suggestions. I was fortunate enough to collaborate with some great people during my research including Prof. Ron Naaman (Weizmann Institute of Science), Prof. Yossi Paltiel (The Hebrew University of Jerusalem), Dr. Suryakant Mishra (Argonne National lab). Their insight and support has made my endeavors successful.

I have also had the opportunity to have so many great people as my lab mates, including Dr. Brian Bloom, Jenny Georgieva, Caleb Clever, Yiyang Lu, Simon Wei, Dr. Gouranga Debhnath, Mary Molitoris. Brian has been like a big brother to me from the very beginning. He has encouraged me in so many ways during the past 5 years. I have bothered him so much, called him at late hours, during weekends, even during holidays – but he never once showed me any reluctance or disdain, and welcomed my overzealous and unrelenting queries with open heart. I am forever grateful to Brian for all his support. Jenny is like a breath of fresh air in my journey.

She is a great friend and always fun to hang around. Dr. Brittney Graff, who has helped me in so many ways when I first joined. Dan has been a good friend and taught me a lot of things, for which I am forever grateful.

It is hard to find selfless people in the world today. But I have been fortunate in that front. I made some great friends during my college back in India. Dr. Manas Sajjan, who is literally the most selfless, helpful, honest and grounded person I have ever met – I am honored to have him as one of my best friends. He has always inspired me, motivated me when I felt lost; our long talks about science during weekends or late nights, even when we were going on vacations has been superbly insightful. Dr. Prakash Shee, who is one of the most fun and energetic people I have ever met. His positive attitude towards life has always uplifted my mood, his counsels has been really helpful during the past years. Dr. Kalyan Santra, who has been a good friend of mine from the very beginning. In Pittsburgh, Anirban, who was my roommate and like a brother to me for the past 5 years; Zack, Ellen, Paul – three of my closest friends in Pittsburgh; Shilpa, Srijani – two of the sweetest friends I have ever had; and Dr. Pravat Mondal and Munmun di – every one of them are like family to me. The love, loyalty and support I got from these friends of mine is nothing less than a blessing.

Words would not be enough to describe what a fortunate person I am for having the family that I have. My father, Mr. Monoranjan Ghosh, has been the greatest support of my life. He made sure to provide me the tools to pursue my dreams and goals. He guided me through thick and thin, disciplined me whenever needed and supported my ambitions whole heartedly. He made sure that I take every ambitious step without any hesitation, walk my path with my head held high. My mother, Mrs. Jayanti Ghosh, her selfless and cautious nature has made me a pragmatic person. She has taught me that even if we soar high, we should never forget where we came from and never to forget our roots. My elder sister Manasi and my younger brother Sudip the two constant pillars of my life. I learned a lot of life lessons from my elder sister and my younger brother has shown me how to unwaveringly support a person throughout, as he has been supporting my choices his entire life. My brother-in-law Dibakar da is one of the most supportive people in my life. His help and support is nothing short of a blessing to me. I would also mention Babu kaku, my childhood tutor. He is truly an inspiring person. His passion for knowledge had me moved and I can proudly say that I owe him a great gratitude for making my science lessons that much interesting that I chose this path and walked so far. Last but not the least, I would like to thank my wife for being by my side throughout these years. She has loved me unconditionally and has always supported me every step in the way. Thank you so much Srijeeta, for tolerating me throughout and being by my side with all the love, care and faith. Having all this people as my family is truly a blessing. Their support, affection and faith upon me has given me the strength to pursue my dreams and goals. I am proud to have them as my family and I hope to make them proud of me as well.

1.0 INTRODUCTION

1.1 CHIRAL INDUCED SPIN SELECTIVITY EFFECT (CISS EFFECT)

In 1999, an important discovery was made that connects electron spin transport and chirality. In this experiment spin polarized photoelectrons were used to study the transmission of electrons through a chiral film comprised of L or D chiral amino acids.[1] It was found that the quantum yield of the photoelectrons depends on both the chirality of the film and the polarization of the light. This phenomenon of spin polarized transmittance of electrons through chiral molecules is called the Chirality Induced Spin Selectivity effect, or CISS effect.[2, 3]

Since the discovery of CISS, a large number of theoretical and experimental studies have been performed in different systems, and using different techniques, to study the effect.[2-11] The CISS effect has been shown to have important implications in all branches of science from biology to chemistry and physics. Over the last few years, CISS has generated significant research interest due to the potential that it has, in different avenues, such as chiral recognition/ separation[12, 13], spintronics devices,[3, 14-16] and spin controlled chemical reaction etc.[17-19] Recent progress in this field has focused on fundamental studies to understand the mechanisms of CISS, as well as, developing new methods and utilizing CISS for important applications. In this chapter, the basic concept of CISS, some important experiments and methods that were used throughout the years, and some applications of CISS, are discussed.

1.2 BASIC PRINCIPLE AND UNDERSTANDING OF CISS EFFECT

To explain the CISS effect a model has been proposed. A chiral molecule creates a helical potential for the electron inside it and this helical potential is responsible for the CISS effect.2, 3 As an electron moves through a molecule, it experiences the electrostatic potential of the molecule. For a chiral molecule, the moving electron experiences a chiral or a helical potential and its movement produces a magnetic field in the rest frame of the electron. The strength of this magnetic field depends on the coupling between the electron momentum and its spin, the spin orbit coupling (SOC). Because an electron has a magnetic dipole associated with its spin, the degeneracy of the two spin states will break when the SOC is high. The Hamiltonian for the SOC can be written as equation 1.1.[2]

$$H_{SOC} = \lambda\vec{\sigma}\cdot(\vec{p}\times\vec{E}chiral)$$ **Equation 1.1**

where $\lambda= (e\hbar)/(4m^2c^2)$, $\vec{p}$ is the momentum of electron, m is the mass of electron, and $\vec{\sigma}$ is a vector whose components are the Pauli matrices $(\sigma_x, \sigma_y, \sigma_z)$. The coupling of the electron spin and momentum plays an important role in the transport of charge through a chiral helix. To explain this, an energy scheme of a propagating electron moving through a chiral helix is shown in Figure 1.1.[2] According to the figure 1-1 there can be four states associated with a freely propagating electron, which are denoted by I+,+>, I-,->, I+,->, I-,+>, where the first variable represents the direction of the velocity and the second represents the spin. When an electron moves in the positive direction through a left-handed helix, its spin up state (+) is more stabilized than the spin down state(-) by an amount $2H_{SOC}$, where H_{SOC} is the spin orbit coupling energy. Similarly, when an electron moves in the negative direction, its spin down state (-) is more stabilized than the spin up state (+) by the same amount of energy. Thus, a spin polarization can be generated.

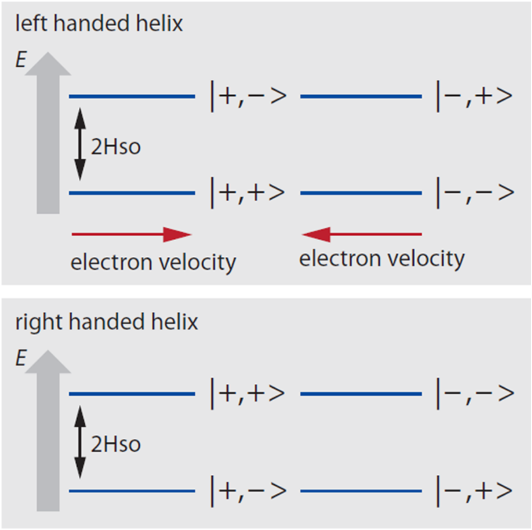

Figure 1.1 Shows an energy scheme of the momentum-spin states |momentum, spin > for a electron traveling in a helical potential.[2] This figure is taken from reference 2.

From the above discussion, it is clear that the efficiency of the spin polarization depends on the strength of the magnetic field that is generated due to the propagation of electrons through the chiral electric field or more specifically on the strength of the SOC.[3] The magnetic field strength inside the helix can be roughly calculated by considering that the force must be large enough to keep the electron inside the helix. This is similar to a cyclotron motion; the effective magnetic field can be written as equation 1.2.[3]

$$|B_{eff}| = \frac{mV}{qr} \qquad \textbf{Equation 1.2}$$

where m is the mass, v is the velocity, q is the charge of the electron, and r is the radius of the helix. One can calculate H_{SOC} by using the formula given by equation 1.3.[3]

$$H_{SOC} = \frac{g}{2}\mu_B|B_{eff}| = \frac{g\mu_B mv}{2qr} \qquad \textbf{Equation 1.3}$$

where g is the g-factor of the electron and μ_B is the Bohr magneton. If one considers an electron with kinetic energy 1 eV ($v = 6\times10^5$ m/s) and uses a radius for the helix of 0.5 nm the H_{SOC} will be equal to 360 meV. Thus, the energy splitting between the states, which is double H_{SOC}, is large enough to explain the CISS effect. A number of theoretical studies has been proposed to explain the CISS effect. Previously, Mujica et al. proposed a constructive interference from multiple scattering can be the reason for enhanced spin-filtering in helices.[9] Recently, Michaeli and Naaman has proposed the spin polarization for the tunneling processes through a barrier can be increased due to the electric field applied on a molecule.[8] Although, other theoretical studies present in the literature qualitatively explains the experimental spin polarization, there is still a lack in a concrete theoretical model which can explain the experimental results more quantitively.[4, 20]

1.2.1 Measurements Methods and Detection Thereof

Over the years, many different techniques and methods have been used to study the CISS effect. Some of those techniques are more direct and measure the spin of the transmitted electrons from the chiral materials; such as photoemission study using Mott polarimeter,[21] and others are indirect where conductance or resistance are measured through chiral material with spin polarized electrons. Some of the important methods that are often used are discussed below.

1.2.1.1 Photoemission Study

In this method, the spin of the ejected electrons from the surface of the chiral molecule/material is directly measured by using a Mott polarimeter.[21] Figure 1.2 shows the experimental set up of a Mott Polarimeter. This kind of experiment is done in an ultrahigh vacuum at a pressure of ~ 10^{-9} mbar. An ultraviolet (UV) laser pulse of a couple of hundreds of picoseconds pulse duration is impinged normal to the sample which results in ejection of photoelectrons from the chiral surface. The resulting spin polarized photoelectrons are then guided by an electrostatic 90^o bender. As a result, the longitudinally polarized photoelectrons are converted into a transverse polarized one, which is then detected by the Mott detector. The spin polarization is then calculated by the equation 1.4, where N_+ and N_- are the scattering count rate in the upper and lower counter of the Mott polarimeter.

$$P = \frac{(N_+ - N_-)}{N_+ + N_-} \qquad \textbf{Equation 1.4}$$

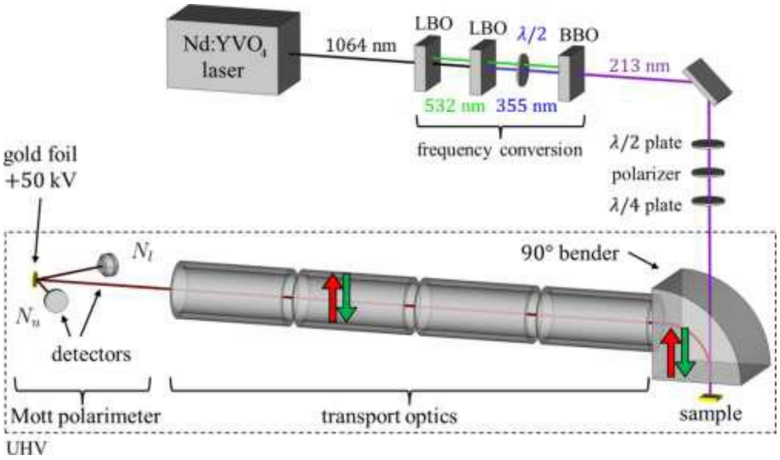

Figure 1.2 Shows the experimental set up for the spin-resolved photoemission experiment.[17]This figure is taken from reference 17.

1.2.1.2 Magnetic Conductive Probe AFM

Magnetic conductive probe AFM (MCP-AFM) is an important technique that is extensively used to study the spin-dependent transport of electrons through chiral molecules/materials. MCP-AFM is similar to conductive AFM, except in this case the substrate is made of a ferromagnetic layer, which is magnetized during the measurement. In this case, a voltage is applied to the substrate containing the chiral molecule/material and the current is measured through the ferromagnetic substrate (Ni) to the chiral molecule/material to the Pt tip of the AFM.

A ultrathin gold layer is often used as a protective layer as nickel is susceptible to oxidation. The measurements are done with two opposite magnetic poles (north and south) pointing toward the nickel substrate. Upon applying a magnetic field, the spin of the Ni layer will be either parallel or antiparallel to the direction of the current. Now because of the CISS effect the conduction of spin current will be favorable for one spin over the other when transiting through the chiral material. As a result, an asymmetry in the current-voltage (I-V) curve is observed for two opposite magnetizations, from which a spin polarization can be obtained. A schematic of the MCP-AFM setup is shown in Figure 1.3 a. Alternatively, MCP-AFM is also done where instead of a ferromagnetic layer a magnetic AFM tip is used as a source of spin polarized electrons (figure 1-3b)

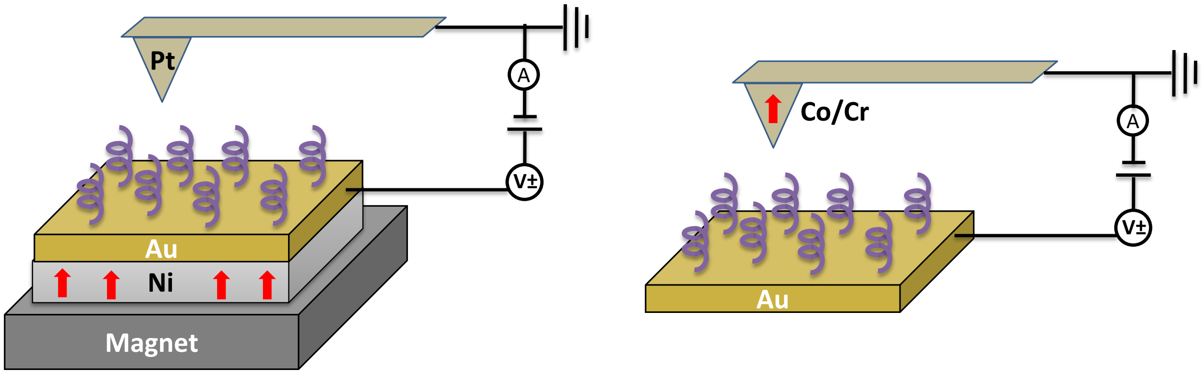

Figure 1.3 Shows schematic for the magnetic conductive AFM where a ferromagnetic layer act as a source for spin current a) or a magnetic probe is used as a spin current source b).

1.2.1.3 Magnetoresistance Measurements

This kind of measurement uses a device which has the same structure as a giant magnetoresistance (GMR) based spin valve, except the ferromagnetic reference layer and the insulating barrier is replaced with a chiral tunneling barrier. Generally, a thin film of an achiral insulating barrier such as MgO is used to block the leakage current. The magnetoresistance measurements are performed in a four-probe configuration inside a cryogenic cryostat equipped with a superconducting magnet. When the applied magnetic field, which magnetizes the ferromagnetic layer, has the same preferred spin as the spin polarization preferred by the chiral layer, the resistance of the system will be lower than the opposite magnetic field. As a result, an antisymmetric magnetoresistance response is observed with the applied magnetic field.

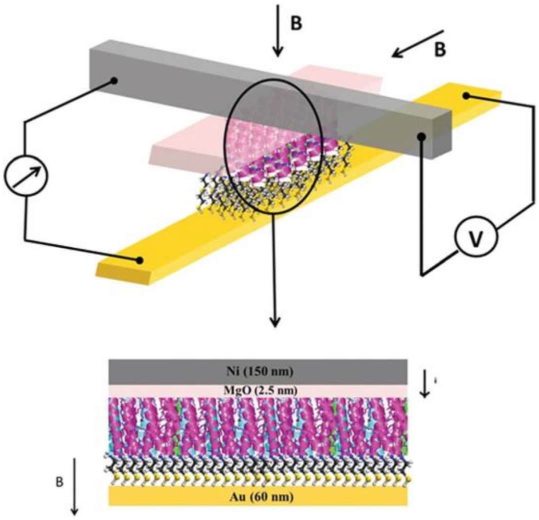

Figure 1.4 Shows a cross section geometry of a spin valve type magnetoresistance device.22 Here B is the applied magnetic field. This figure is taken from reference 22.

1.2.1.4 Electrochemistry

Spin polarization through chiral molecules has also been explored by studying electrochemical redox reactions. In this case, the working electrode is made of a ferromagnetic layer coated with chiral SAM/material and an achiral molecule such as cytochrome C or ferrocene is used as redox species (Figure 1.5). Electrochemical reactions are studied by varying the magnetization of the ferromagnetic layer. Due to the CISS effect the electron transfer rate through the chiral layer depends on the spin of the electrons and as a result the electrochemical current for the redox reaction was found to depend on the magnetization direction. For this kind of experiment, Spin polarization (P) can be determined by using the following formula.

$$P = (I_{up}-I_{down})/(I_{up}+I_{down})$$

where I_{up} and I_{down} are the currents for up and down magnetization respectively.

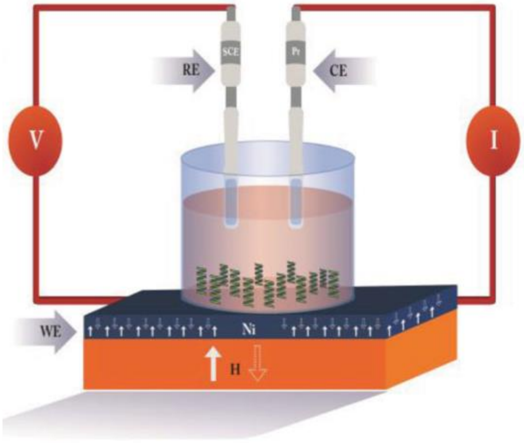

Figure 1.5 Shows a schematic for a electrochemical setup for CISS measurement.[23] Here the Ni is the working electrode and the Pt and saturated calomel electrodes are the counter and reference electrode respectively. The molecules are adsorbed on the Ni surface which is magnetized with a external magnetic field (H). This figure is taken from reference 23.

1.2.1.5 Hall Device

Another way of measuring spin polarization is by using a Hall effect based electrochemical cell. The Hall effect says, when current flows between two electrodes in a magnetic field perpendicular to the electron flow, an electric potential arises in the perpendicular to both the electric and magnetic field directions. For a CISS measurement, a modified Hall device is used where a constant current/voltage is driven between the source (S) and the drain (D) through the device, and a Hall voltage is measured in the perpendicular direction between H1 and H2. (Figure 1.6) To study the spin polarization of the chiral molecules, a monolayer is prepared on the surface of the device. Next a voltage is applied between the device and a gate, or counter, electrode. This applied voltage creates an electrostatic field across the molecules, which induces a charge polarization. Because of the CISS effect, this charge polarization is accompanied by a spin polarization and a voltage is generated between H1 and H2. Generally, a linear correlation is observed between the applied field and the Hall voltage, the slope of which tells about the degree of the spin polarization.

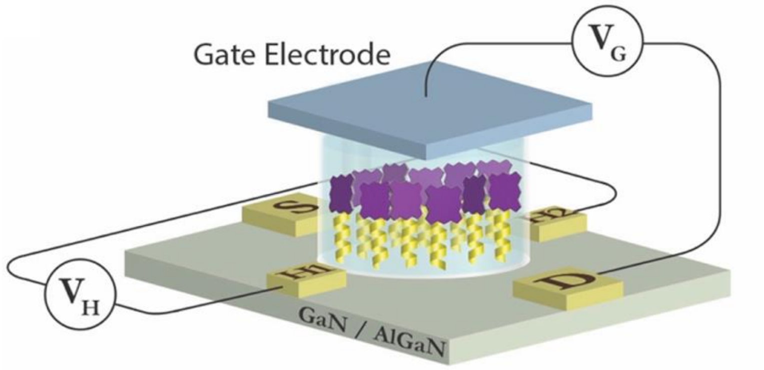

Figure 1.6 Shows a schematic of a Hall effect based device for spin polarization measurement [24]. This figure is taken from reference 24.

1.2.2 Timeline of Initial Experiments and Findings

Over the years, a wide range of experiments have been done to examine the CISS effect. Some of the important experiments are discussed here. The first CISS experiment was done in 1999 where CISS experiment was shown on chiral Langmur-Blodgett films comprised of chiral L or D stearoyl lysine (on Au substrate) using low-energy photoelectron transmission (LEPET) spectroscopy.[1] Circularly polarized light was used to eject the photoelectron from the gold electrode; the results show that quantum yield of the photoelectrons depend on both the chirality of the film and polarization of the light (which was used to control the initial spin polarization of the photoelectrons). Although this study indirectly proves the spin selectivity in the photoelectron's transmission through chiral molecule, a more direct method of measuring spin polarization was implemented later by using a Mott polarimeter.[21] In the Mott polarimeter, angular distribution of the electrons, which depends on the initial spin, are measured and was used to study the spin-filtering by a double-stranded DNA coated gold substrate. (Figure 1.7)

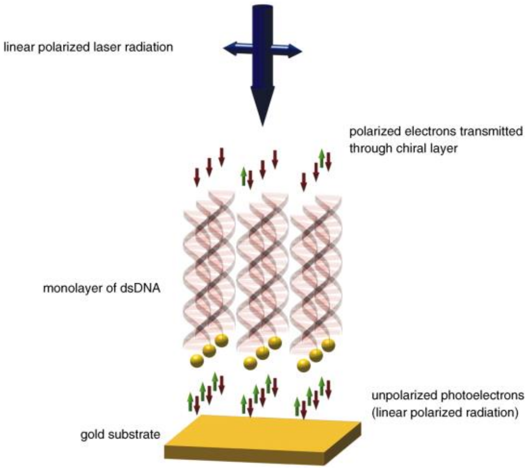

Figure 1.7 Shows schematic of the monolayer of ds-DNA as a spin filter for the photoemission experiment. In this case, linear polarized light ejects unpolarized electrons from the gold surface, which then get spin polarized after transmitting through DNA.[21] This figure is taken from reference 21.

The CISS effect has also been shown in electron transport and electron transfer processes. Electron transport in the tunneling regime was studied by measuring single molecule conductance of double-standard DNA by using magnetic conductive-AFM technique. In this study, spin polarized electrons from the nickel are injected from either parallel or antiparallel to the helical axis and the results show that the conduction of electrons through the DNA is spin selective.[25] The importance of the CISS effect was also shown in electron transfer processes. In one of the recent studies, it was shown that the electron transfer from photoexcited nanoparticles through a chiral system was more efficient than transfer through an achiral system.[26] For this study, CdSe nanoparticles are attached to the chiral and achiral SAM coated on a gold substrate. Upon excitation of the NP, there will be a charge transfer between the NP and the gold surface, which resulted in formation of a dipole in the surface. By measuring the contact potential difference using a Kelvin probe method,[26] the difference in the work function between the probe surface and gold surface was examined. In another study, a photoelectrochemical measurement was done, in which a porphyrin chromophore was attached to chiral SAM coated on a gold substrate. In this case, circularly polarized light was used to photo-excite the chromophore and the dependence of the photocurrent was examined with the polarization of the light and the chirality of the SAM. An asymmetry in photocurrent was observed with different circularly polarized light, which changes with molecular chirality.[27] CISS based electron transfer has also been studied by different methods, such as magnetoresistance,[28] spin dependent electrochemistry,[29] and by capacitance measurements.[30] All of these experiments show the importance of the CISS effect on electron transfer processes in the tunneling regime.

Very recently, another important experiment was done by Kumar et. al who used Hall measurements to show that within a chiral molecule a charge polarization accompanies spin polarization and that it happens without any external electron transfer and charge flow.[13] These results show that spin polarization can happen within the chiral molecules, even without any net electron transfer or electron transport. Some other important experiments on CISS can be found in the recent CISS based review papers.[3, 11]

1.2.3 Spin Polarization Through Different Chiral Material

Earlier studies on CISS effect were mostly done on either chiral peptides or DNAs in gold substrate. In 2013, spin polarization studies examined purple membranes containing bacteriorhodospin deposited on gold, aluminium/aluminum oxide, and nickel substrates. Although the spin polarization obtained from that system is only 15 %, it shows that the CISS effect originates from the chiral system itself irrespective of the substrate.[29] Since CISS effect tells that chiral molecules or chiral materials can act as a spin filter, it is important to study spin polarization through different chiral materials for future applications in a spintronics device. Recently, spin polarization efficiency was studied with different chiral materials. In 2015 Prakash et al. studied spin selective electron transport through a chiral polymer (poly{[methyl N -(tert-butoxycarbonyl)-

S-3-thienyl- L - cysteinate]-cothiophene) and observed spin polarizations as high as 50%.[23] Spin filtering properties were also studied with molecules without a stereogenic carbon center but possessing a dissymmetric secondary structure; namely with helicenes as done by Kiran et. al.[31] They have also shown the importance of molecular orientation of the film for efficient spin polarization, where they were able to increase the spin polarization from 4 % to ~ 50 % by making a uniform film. Other bioorganic molecules such as multiheme cytochromes and ethylene-bridged (porphinato) zinc structures were also shown to act as efficient spin filters.[24, 32] Recently, spin polarization through chiral π-conjugated fibers[33, 34] show a high spin polarization (close to 85 %) for conducting polyaniline of micron size fiber and show that spin selectivity can be observed even in micron distances.

While most work has examined spin polarization through organic molecules, workers have also done experiments with chiral hybrid inorganic/organic material. Bloom *et. al.* have shown spin selective electron transfers through chiral CdSe quantum dots coated with cysteine molecules.[35] Other organic/inorganic material such as 2D perovskite has also shown very high spin polarization (86%) for electron transport.[36] Spin polarization study was also done by chiral CuO thin film using photoemission experiment. A very weak spin polarization (5 %) was obtained with the film.[17] Recently, chiral induced spin transport was also studied through pure inorganic monoaxial chiral dichalcogenide $CrNb_3S_6$.[37] By measuring the spin phenomenon as inverse spin Hall signal, they were able to show the spin signal can be observed in a micrometer length scale, which is important since spin generally depolarizes within nanometer distance.

1.3 MAGNETIC AND THE CHIRAL INDUCED SPIN SELECTIVITY EFFECT

Chiral induced spin selectivity tells that chiral molecules can be used as a source of spin polarized electrons; similar to a ferromagnetic material. This property of chiral molecules can be utilized for different applications in memory devices. For example, in traditional spin based memory devices, spin current is used to magnetize the magnetic storage domains utilizing the spin-transfer torque (STT) effect. Two main problems of using STT effect to make a spintronic device are that 1) it requires complicated device structure and 2) it requires a high current density to operate. Another problem of using ferromagnetic material in a spin-based memory device is the limitation in miniaturization of the device. Use of ferromagnets limits the size reduction that is possible due to the magnetic property of ferromagnets, which depend on the size of the material. We and others have showed how CISS can be used to circumvent these issues. In this section, details about magnetic properties of materials, magnetism induced by CISS and also some CISS based memory devices are discussed.

1.3.1 Size Dependent Magnetic Properties

Magnetic nanoparticles exhibit magnetic properties that depend on their size and shape, as well as their composition.[38] Before discussing about the size dependent magnetic properties let us consider different kinds of magnetic properties. Depending upon its response to a magnetic field, a material can be divided mainly into four types: diamagnetic, paramagnetic, ferromagnetic, and superparamagnetic. These material types differ by their different magnetization, their magnetic susceptibility, and their magnetic permeability. The magnetization (M) of a sample is defined as $\frac{\Sigma \vec{m}}{V}$, where $\vec{m}$ is magnetic moment of each atom and V is the volume. The magnetic susceptibility

(χ) quantifies a material's response to an applied magnetic field and the magnetization it generates. It is defined as $\chi = (M/H)$, where H is the applied magnetic field. The permeability (μ) of a substance is a response function that reports on how the magnetic induction B changes with the applied magnetic field H i.e., $\mu = B/H$. The relative permeability (μ_r) is the ratio of the permeability of any material to the permeability of vacuum (μ_0) i.e., $\mu_r = \mu/ \mu_0$. The susceptibility and the permeability are related through the formula, $\mu= \mu_0 (1+ \chi)$.

Diamagnetism: A diamagnetic substance has a very weak interaction with an external magnetic field due to an absence of unpaired electrons. For such materials the relative permeability $\mu_r \leq 1$ and the magnetic susceptibility is very small (10^{-6}–10^{-3}).

Paramagnetism: Paramagnetic substances have a net magnetic moment due to the presence of unpaired electrons. Like diamagnetic substances, the magnetization is also zero for paramagnetic substances in the absence of a magnetic field. For these materials the relative permeability is $\mu_r \geq 1$ and the susceptibility is very small (10^{-3}–10^{-5}).

Ferromagnetism: Unlike paramagnetic or diamagnetic materials, ferromagnetic substances exhibit strong magnetization even in the absence of an external magnetic field. Most ferromagnets have multiple magnetic domains that are separated by domain walls. In magnetism, domain walls are interfacial regions between volumes of a ferromagnetic material that have different magnetic moments. In a particular domain all the magnetic dipoles align in the same direction. The magnetization of a ferromagnetic substance with an external magnetic field gives a hysteresis curve as shown in Figure 1.8. When the magnetic field strength is increased in the positive direction, the magnetization of a ferromagnetic substrate increases until it reaches the saturation point (M_s). If the magnetic field strength is then decreased, the magnetization does not follow the same trajectory; instead, it falls down more slowly. In fact, when the magnetic field strength is returned to zero the magnetization does not go back to zero, there will be a remanent magnetization (M_r). In order for magnetization to become zero, a reverse magnetic field must be applied and at some value (H_c') the magnetization will become zero. The point H_c' (or H_c) in the diagram is the coercive field or coercivity, which quantifies the ability of a ferromagnetic material to resist an external magnetic field without being demagnetized. If the reverse magnetic field is increased further the magnetization will continue to decrease until it reaches the saturation point ($M_s^{'}$) oriented in the opposite direction. If the magnetic field is then again increased in the positive direction, the magnetization will pass through zero (H_c) and then will return to M_s. This resulting loop is called a hysteresis loop.

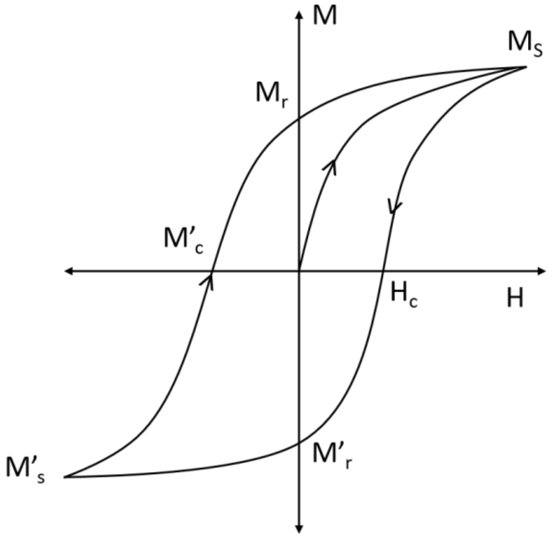

Figure 1.8 Magnetization curve of ferromagnetic material.

The magnetic properties of a ferromagnetic substance change drastically as the size goes from bulk to nanometer scale (Figure 1-9). As the size of the material decreases, it goes from having a multi-domain structure to a single domain structure. The critical diameter at which this transition happens, depends on the shape and the material type. Table 1.1 shows the critical diameter of a few substances.[39]

Table 1.1 Estimated critical diameter for single domain magnetic nanoparticles.[39]Table is taken from reference 39

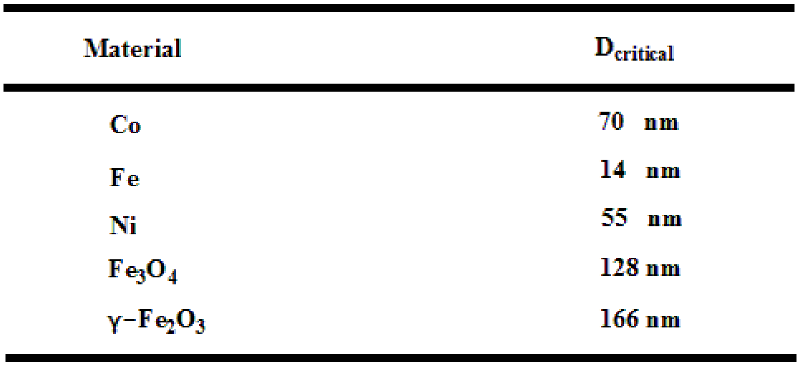

Material	$D_{critical}$
Co	70 nm
Fe	14 nm
Ni	55 nm
Fe_3O_4	128 nm
$\gamma-Fe_2O_3$	166 nm

The reversal in magnetization of a multidomain material happens by the movement of the domain wall, whereas the magnetization reversal for a single domain structure can only be realized by rotating the magnetic moments of the particle. Because the latter is energetically more demanding, the single domain structure often has a higher coercivity as shown by the blue line of the Figure 1.9 (right).

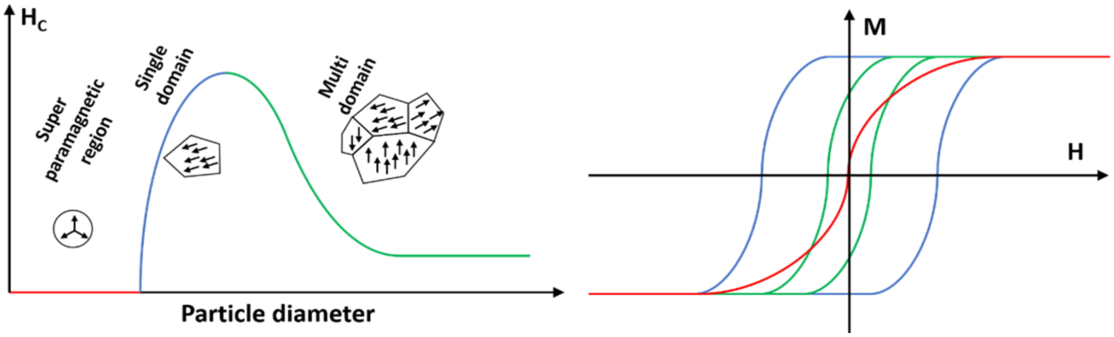

Figure 1.9 The diagram on the left shows the generic dependence of a magnetic material's coercivity H_c on its physical size: multidomain (green), single domain (blue) and superparamagnetism (red). The diagram on right shows magnetization hysteresis loops for the different domain size behaviors.

Superparamagnetism: If the size of a ferromagnetic substance is decreased even further in the single domain, it can enter into a special regime where the magnetization response is like that of the paramagnetic particles but with a much higher magnetic susceptibility.[40] For this regime, magnetization is susceptible to thermal energy fluctuations, i.e., the magnetization will flip back and forth spontaneously. The time between two flips is called the Neel relaxation time and is often described by the Néel-Arrhenius equation (equation 1.6).[40]

$$\tau_N = \tau_0 e^{\frac{KV}{k_B T}}$$ **Equation 1.5**

where τ_N is the average time that it takes for the magnetization to flip, τ_0 is the attempt time, which is characteristic of the material, K is magnetic anisotropy energy, V is the volume of the material, k_B is Boltzmann constant, and T is the temperature. When the time of a measurement is larger than the Neel relaxation time, the average magnetization will appear to be zero and the particles are said to be in a superparamagnetic state. Superparamagnetism sets a limit for the minimum size of the particles that can be used in magnetic memory applications, such as hard drives.

1.3.1.1 Magnetic Measurement

Magnetic Force Microscopy: Magnetic force microscopy (MFM) technique is a variant of atomic force microscopy where the scanning tip is coated with a magnetic material that allows for the imaging of the spatial distribution of the magnetic fields of magnetic substances. For films of magnetic material, there will be a magnetic interaction between the magnetic tip and the material in addition to the mechanical and electrostatic interactions between the tip and the surface. To minimize the mechanical forces, MFM measurements are done at a large tip-to-sample distance. In general, MFM measurements are done using an "interleave" scan mode, in which two scans are performed on the surface. In the first scan, the tip scans the surface in non-contact mode to obtain the topography of the surface, and for the second scan the tip-sample distance is increased to a particular value and scans are performed along the topography line to maintain a constant height between tip and the sample (Figure 1.10).

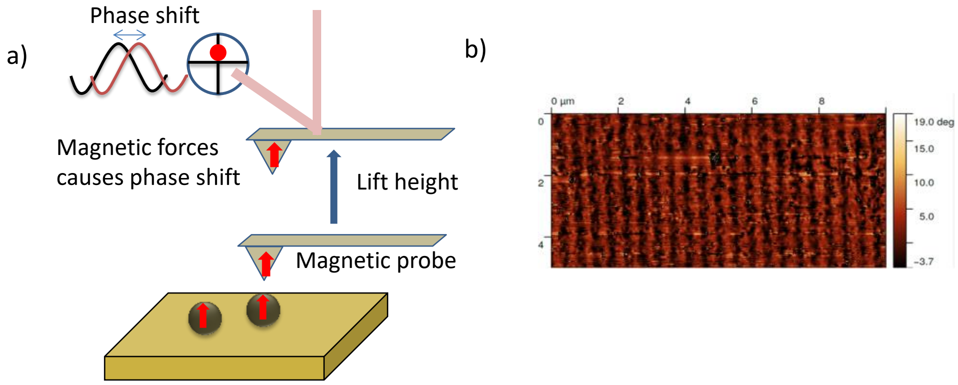

Figure 1.10 a) The schematic diagram illustrates a magnetic force microscopy (MFM) measurement. MFM uses a combination of tapping mode and lift mode (or interleave mode). b) The diagram on the right shows the magnetic phase signal of a magnetic test sample that was measured with our instrument. Dark and bright lines show different domains in the sample.

During the second scan, the tip will be affected by the magnetic force; the magnetic force shifts the cantilever oscillation, and this change is measured as a phase shift (shown in Figure 1.10).

SQUID Magnetometer: A superconducting quantum interference device, or SQUID, is a very sensitive magnetometer, based on superconducting loops with Josephson junctions; and it can be used to measure very small magnetic fields. This device is based on two principles: Josephson effect at a superconductor- insulator- superconducting junction and magnetic flux quantization on a superconducting loop. The Josephson effect is the flow of a constant current between two superconductors even if they are separated by a tunneling barrier. A SQUID incorporates Josephson junctions in a ring structure (Figure 1.11). An important property of a superconductor ring is magnetic flux quantization, i.e., a superconducting ring allows only certain magnetic flux values which are an integer multiple of the flux quantum Φ_0. In a SQUID the current flow through the Josephson junction is very sensitive to the magnetic field in the ring. Because of the quantum nature of the flux, the current (hence the voltage of the whole SQUID) varies periodically with the magnetic field applied to the ring. The period of this oscillation is related to the flux quantum Φ_0. Thus, by measuring this variation it can be determined how many Φ_0 flow through the rings.

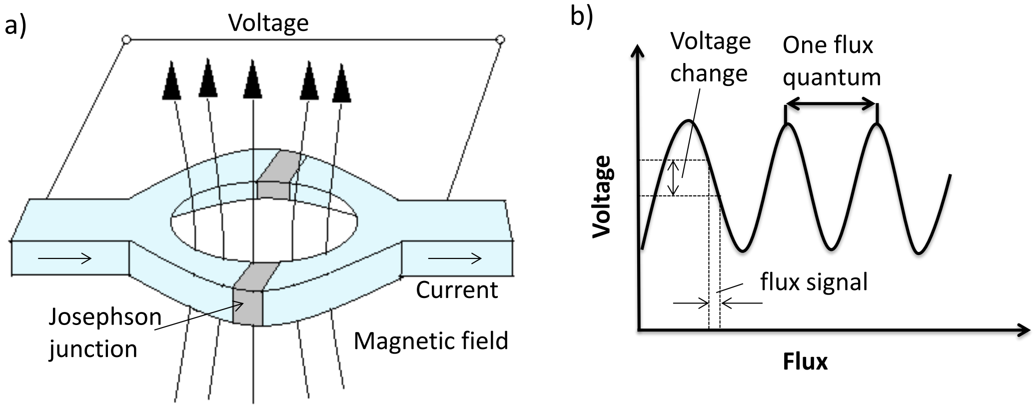

Figure 1.11 a) Schematic diagram shows a DC SQUID where two Josephson junction are connected in parallel. b) The plot shows the output voltage signal with magnetic flux. As can be seen from the diagram a small flux signal produces a corresponding voltage swing across the SQUID.

1.3.2 Magnetism Induced by Proximity of Chiral Molecules

The formation of a self-assembled monolayer (SAM) of chiral molecules on a gold surface can magnetize the surface.[41-43] This effect is called magnetism induced by proximity of adsorbed chiral molecules, or MIPAC effect. It originates from SAM formation and the CISS effect. When a SAM of chiral molecules with large dipole moments is adsorbed on a metal surface, charge transfer occurs to equalize the electrochemical potential between the adsorbed layer and the metal surface. Because of the CISS effect, the charge transfer through the chiral molecules is spin selective. Thus, spin polarized electrons are produced on the metal surface, and magnetize it. Alternatively, one can view the phenomenon as arising from the excess electron density on the Au surface which becomes spin polarized because the wavefunction penetration into the chiral molecule is spin dependent. This leads to an imbalance in spin-up and spin-down populations on the metal and magnetizes it.

Recently Dor, *et al* showed this effect for the adsorption of chiral polyalanine (AHPA) on Au-coated ferromagnetic (FM) films. They showed that the FM substrate film could be magnetized by polyalanine adsorption and that the switching of the magnetization direction can be controlled by the handedness of the chiral molecules.[44]

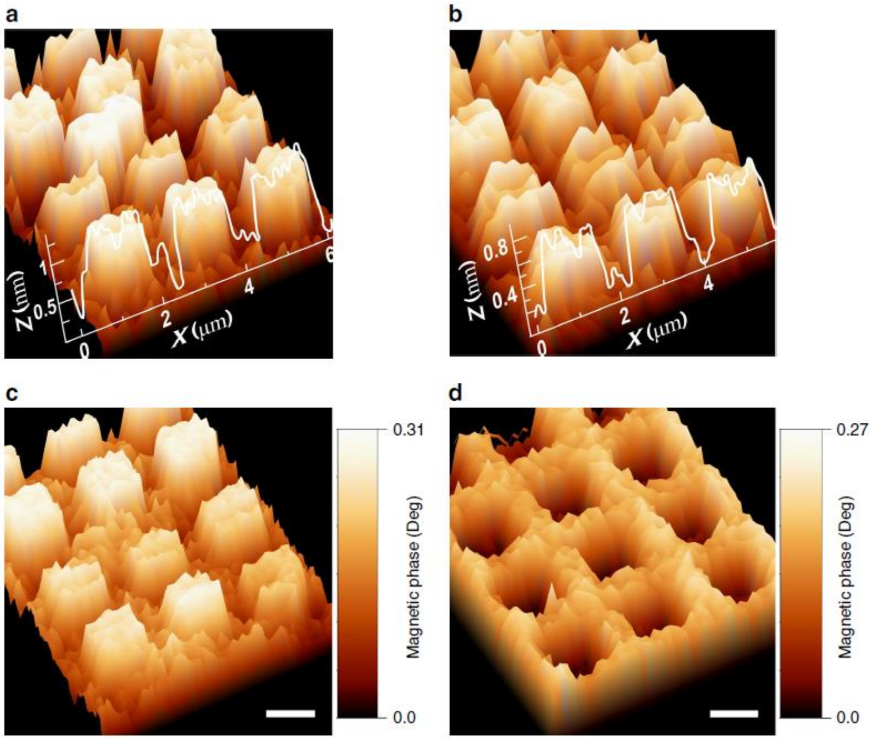

Figure 1.12 Panel a and b show the topography images of the SAM of AHPA-L (a) and AHPA-D (b) adsorbed onto a lithographically patterned ferromagnetic layer. Panel c and d show their corresponding magnetic phase signal. As can be seen from the diagram, the L and D chiral molecules show opposite magnetic field directions.[44] This figure is taken from reference 44.

Figure 1.12 shows the topography images and magnetic phase signals of a patterned substrate covered with either L-polyalanine (left) or D- polyalanine (right) monolayers. In this image the bright region in the magnetic phase indicates a repulsive interaction and the dark region indicates an attractive interaction. As can be seen from the figure, even though topography signals are the same for both AHPA enantiomers; the magnetic phase signals are opposite.

1.3.3 CISS Based Memory Devices

Spintronics based memory devices are important because of their increased data processing speed and decreased electric power consumption compared to conventional semiconductor devices.[45] Conventional semiconductor devices use the charge properties of the electrons, whereas spintronics devices use the spin properties of electrons.[3, 45] In general spintronics based magnetic memory devices are made of two magnetic layers; one permanent magnetic layer and another ferromagnetic layer called a “free layer” (Figure 1.13).[15] Most of these devices are based on a spin filter concept in which the free layer is magnetized either by a current loop or by transferring spin alignment to it. In this kind of system, spin polarized current is produced by passing it through the permanent magnet layer. When the ferromagnetic layer and the permanent magnet are aligned, the electrical resistance will be low (top image in figure 1.13a) and when they are antiparallel to each other the electrical resistance will be high (bottom image figure 1.13a). As can be seen from the diagram for the case of the parallel configuration, the majority spin (up) electrons and minority spin (down) electrons from the permanent magnetic layer can easily transfer to the second ferromagnetic layer and fill majority spin (up) and minority spin (down) electronic states respectively and will result in a large conductance or low resistance state. Whereas in the case of the anti-parallel state, the majority spin (up) electrons and minority spin (down) electrons from the first ferromagnetic layer fill the minority (up) and majority (down) states in the second ferromagnetic layer, respectively. This will result in a lower conductance or higher resistive state. Thus, 0 and 1 state can be controlled by changing the direction of the “free” layer magnetization. Although spintronics devices are already in use, their reliance on a permanent magnet restricts the device size and imposes structural requirements.

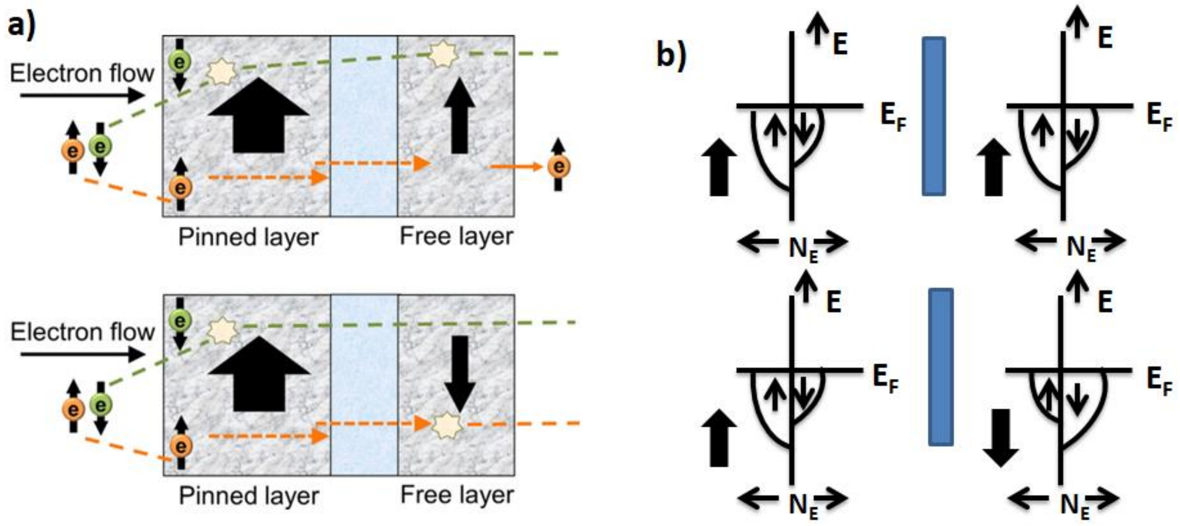

Figure 1.13 The above diagram (a) illustrates the spin dependence of conductance in spintronics based memory devices. Diagram b) shows a schematic of the density of electronic states for the corresponding parallel and antiparallel configuration (E is the energy, E_F is the Fermi level energy, N_E is the density of states).

Recently, a new type of magnetic memory device without a permanent magnet has been demonstrated. In those devices the CISS effect was utilized, where a chiral molecular layer was used as a spin filter to produce spin polarized current.[3, 14] In the first demonstration, a chiral polyalanine self-assembled monolayer film (AHPA in Figure 1.14) on Au replaces the permanent magnet layer, but a ferromagnetic free layer is retained. In this device, the resistivity or the current flow is changed by changing the magnetization of the free layer. With this concept the device size was decreased to 30-40 nm by using single domain ferromagnetic nanoparticles (FMNP).[16] That structure displays a threefold increase in the resistivity between the one and zero resistance states.

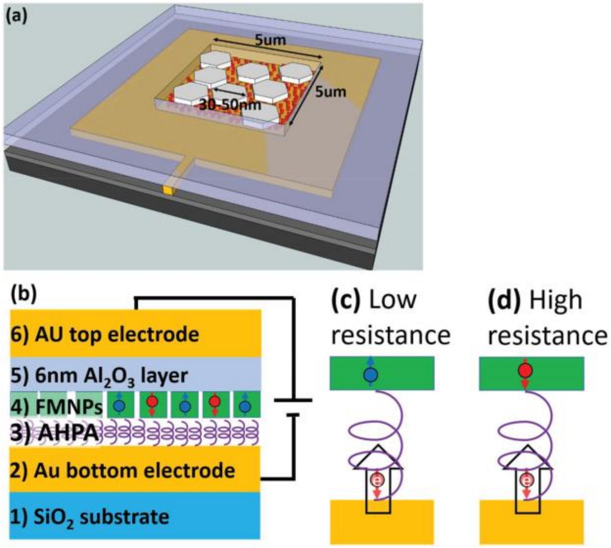

Figure 1.14 The above diagram shows a schematic of a CISS based spintronics memory device. a) Shows top view of the device. b) Shows side view of the device. The FMNPs have a random magnetization without the magnetic field. A right handed helix will transport spin down electrons preferentially to the FMNP (c). Now if the FMNP is magnetized upward, the resistance will be low. For the same configuration the resistance will be higher when the FMNP is magnetized downward (d). [16] This figure is taken from reference 16.

1.4 IMPORTANCE OF SPIN IN CHEMICAL REACTION

Controlling chemical reactivity by spin manipulation has been one of the most significant researches of the last decade that has shown a great promise to control the rate and selectivity for the product formation.[46-48] Spin effect on chemical reaction is amusing since the spin interaction energy in general is orders of magnitude smaller than the thermal energy k_BT. The importance of spin chemistry has been shown to have applications in different areas of science, which includes solar energy conversion in photosynthetic systems,[49] magnetic direction sensing by migratory birds,[50] NMR sensitivity enhancement,[51, 52] quantum computing, and magneto-electroluminescence in organic semiconductors.[53] Although a number of studies have shown spin control on chemical processes, most of the early experiments are limited to organic radical pairs. Recent experiments on spin control, based on the CISS effect, have shown a great promise for controlling spin in other chemical reactions. Some fundamentals about the spin-controlled reactions along with more recent experiments, are discussed in the next section.

1.4.1 Basic Principles and Some Examples

The spin control in the chemical reaction comes from the fundamental principle of "angular momentum conservation rule" which states that the rate of the chemical reaction will be zero where the spin of the reactant wavefunctions are different from the product. Although, this spin selection rule can be violated for real systems, as Hamiltonians have spin orbit coupling terms, nevertheless the chemical reaction rate will be slowed because the timescales for spin flips can be slow. Organic radical pairs are the most common species to show the spin effect in chemical reactions.[54] Radical pairs, formed by some chemical reactions, can be either in singlet or triplet states; and it was found that the radical pairs can interconvert between singlet and triplet state as a result of Zeeman, exchange, and dipolar interaction of the electrons spin and the nuclear spin.[55, 56] An applied magnetic field was found to affect the singlet-triplet conversion and hence the product formation which depends on the spin state of the radical pairs. Details about spin chemistry related to the radical pairs can be found in the literature.[47, 48]

Spin control on chemical reactions can also be found in other chemical processes. For example Scheffler has shown that the stacking of triplet O_2 has a low stacking parameter on a singlet state Al(111) surface.[57] Conservation of spin rule can also be seen in dipolar energy transfer processes, as shown by Guo et. al.[58] It was shown that excited state energy transfer from a rhenium(I) excited state to a chromium(III) acceptor is more efficient than that to a cobalt(III) acceptor, even though the latter has a higher dipolar cross section. The efficient energy transfer in the former case was attributed to the same spin state of the donor and acceptor which results in a spin allowed process.

1.4.2 Spin Control Using the CISS Effect

Although spin is an important parameter for a molecule's electronics structure and essential for bonding formation, spin control in chemical reaction has not been explored vastly. Part of the reason might be due to the weak coupling between electron spin and a molecule's nuclear geometry. Because of the weak coupling, it is hard to control the relative orientation of the intermediate radical species with respect to the reaction coordinate(s). Recent discovery of CISS effect has shown chiral molecules are different,[10] and electron transfer and electron rearrangement in a chiral molecule is affected by the spin. Generally, for a closed shell molecule charge reorganization or polarization creates a dipole moment across the molecule, and in chiral molecule this electron displacement creates a spin polarization. That is, for a chiral molecule opposite spin accumulation occurs at the opposite electric poles and this can cause the molecule to act as a "singlet biradical". This property of chiral molecules may contribute to the enantioselectivity in the interaction of the chiral molecules, and it opens up new ways to control the spin in chemical reactions.[10, 13] Recently, several important applications based on this effect has been shown; such as separation of enantiomers with a ferromagnetic surface,[12] enantiospecific electrochemistry,[59] and water splitting with chiral materials.[17, 19, 60, 61] Details about these specific projects can be found in the literature.

1.4.3 OER and Mechanism

Electrolysis of water to produce hydrogen is considered one of the promising avenues which can fulfill the clean energy demand. Several studies have been done to make stable, efficient, cost effective catalysts that are required to make water splitting a viable energy technology. But higher overpotential, often found in the water splitting experiment, limits the use of catalyst to make it an economically viable process. Previous experiments have shown that the spin of the intermediate species during water splitting experiments play a crucial role in determining the efficiency of the catalyst.

1.4.3.1 Basic of Oxygen Evolution Reaction

The water splitting reaction can be divided into two half reactions: The hydrogen evolution reaction, or HER, and the oxygen evolution reaction, or OER.

$$4H_2O + 4e^- \rightarrow 2\,H_2 + 4\,OH^- \qquad \text{HER}$$

$$4OH^- \rightarrow 2\,H_2O + O_2 + 4\,e^- \qquad \text{OER}$$

Among the two reactions, the oxygen evolution reaction is considered to be the more challenging since it occurs through a complicated four electron process, which leads to formation of an O-O bond. The OER reaction is kinetically sluggish and generally a higher overpotential is required for this reaction to occur at a useful rate. For electrochemical reactions, the overpotential of a reaction is the extra potential that one needs to apply in order for product formation as compared to the thermodynamically required value. The thermodynamic potential for the OER can be calculated as follows; for the reaction below,

$$2H_2O \rightarrow O_2 + 4H^+ + 4e^- \qquad E_0 = +1.23$$

This potential will shift depending on the pH value and the modified potential can be calculated using Nernst equation as shown below:

$$E_{new} \rightarrow E_0 + 4\frac{RT}{nF}ln[H^+]$$ **Equation 1.6**

Because n = 4 in this case,

$$E_{new} \rightarrow E_0 + 0.059\ ln[H^+]$$ **Equation 1.7**

For pH 13, $E_{new} = 1.23 - 0.059*13 = 0.46$ V. Thus, the overpotential will be $\eta = V_{app} - 0.46$ V, where η is the overpotential, V_{app} is the applied potential, and 0.46 V is the theoretical onset potential of OER (vs SHE)

In the past few decades, extensive studies were performed to design stable and efficient catalysts that have lower overpotential. To date RuO_2 and IrO_2 have been considered to be the benchmark for the OER with an overpotential of 300 mV in the alkaline medium.[62] Even though significant studies on these oxides are reported in literature, large scale production is hindered as both of them are made of precious metals. Transition metal oxides, on the other hand, have shown comparable electrocatalytic activity, whereas they are both cheap and can be synthesized easily.[63, 64]

1.4.3.2 Oxygen Evolution Reactions Mechanisms

Understanding the reaction mechanism of OER is key to improving water splitting catalysis.[65] Some electrocatalytic parameters such as the Tafel slopes, which relate the rates of an electrochemical reaction to the overpotential, provide valuable information about the mechanism of the OER. Details about the analysis of the Tafel slope for a multistep process and the mechanism are available in the literature.[66] Over the years, many scientists have proposed possible mechanisms for OER with a metal (M) based catalyst in either basic or acidic conditions. Most of the proposed mechanisms include similar intermediates such as MO, MOH, MOOH, whereas the major difference is found in the last step; i.e. the formation of O_2 step. An example of a step-by-step mechanism for the OER is shown for a basic medium (red curve) and an acidic medium (blue curve) in Figure 1.15. The active site of the OER is shown by M. At the first step a hydroxyl radical is adsorbed on the active site to form M-OH; which then undergoes a coupled proton and electron transfer to form M-O. From the M-O intermediate there are two different pathways which can form the molecular oxygen. One is a more direct route through the combination of two M-O moieties to produce O_2; whereas the other one involves the formation of another intermediate M-OOH before it decomposes to O_2. The diagram shown is a typical blueprint for the general OER mechanism. In addition to these steps, some papers also show a parallel step where 2M-OH goes by a slow dissociation to form hydrogen peroxide. Formation of H_2O_2 is found to be more stable at acidic pH, however, it eventually decomposes to molecular oxygen.

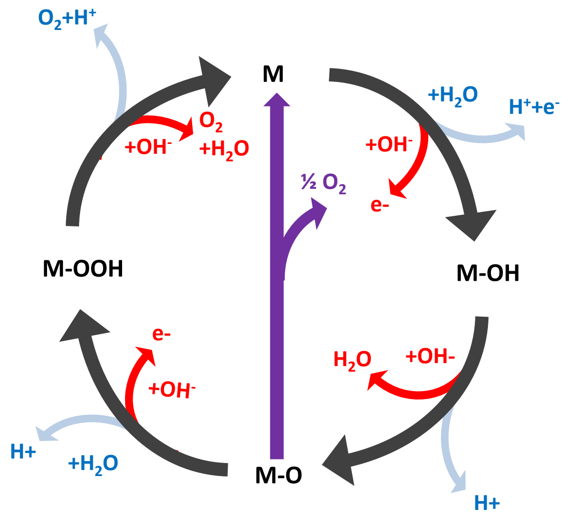

Figure 1.15 The OER mechanisms for basic (red) and acid (blue) medium.

1.4.4 Spin Control in Water Splitting

The ground state of O_2, referred to as triplet oxygen, has two unpaired electrons and is paramagnetic ($3\sum_g^-$); whereas the first excited state of the oxygen molecule is a singlet state, about 1 eV higher than the ground state. Because of the spin conservation rule, formation of an O-O bond on breaking the water molecules will require that one access the triplet energy pathway to form the triplet ground state oxygen. Often this spin consideration is not taken into account for the design of OER catalysts, as a result O_2 triplet formation and singlet mediated process; namely the formation of hydrogen peroxide and other superoxide species, compete with one another. If spin restrictions can be imposed on the catalysts then one can impose spin polarization on the surface to create spin polarized intermediates and to favor the triplet process. There are mainly two ways to create the spin polarization; either by using a magnetic field or by using a chiral molecule.

1.4.4.1 Control Spin with Magnetic Field

Because OER produces triplet oxygen which is paramagnetic, incorporation of magnetism in the surface should be beneficial in OER. In other words, magnetism should create the spin polarization on the surface and hence the radical intermediates will have parallel spin; which will allow formation of triplet oxygen. Previous workers have studied the effect of magnetism on OER was studied both theoretically and experimentally. For example, Groot et. al has studied electronic and magnetic properties of $RuO_2(110)$ surface to explain the higher efficiency of the catalyst in water splitting.[67] Electronic structure calculations show that even though bulk RuO_2 is not magnetic, the surface of the catalyst is magnetic which allows the triplet oxygen production conserving the angular momentum. Gracia has also done a lot of theoretical work on the electronic and magnetic properties of the orbitals of perovskite structures to determine how those properties influence the efficiency of the catalyst.[68-70] They have shown different criteria for the d electron's electronic configuration that facilitates the spin dependent electron transfers in a catalyst. Their calculations indicate that itinerant magnetism, characterized by hopping electrons with their spin aligned to the lattice core spin, can collectively transport electron spin in a material and make it a good catalyst. Only a few people have shown experimentally the increased efficiency in the water splitting with a ferromagnetic catalyst; for example, Garces-Pineda et al. who have shown for the first time a direct magnetic field enhancement of water splitting.[71] They showed that the efficiency of the OER can increase by more than 100%, at high current density, when a magnetic field is applied to ferromagnetic coated nickel foam substrates.

1.4.4.2 Control Spin with Chirality

The fact that a chiral molecule can act as a spin filter makes chiral molecular-based catalysts potential candidates for efficient OER. Important contribution on water splitting with different catalysts coated with chiral molecules have come from Naaman's group. Their first contribution in 2015 dealt with TiO2 coated with chiral polyalanine molecules for the spin controlled water splitting.[19] A significant reduction in the overpotential when chiral oligopeptide or DNA was used, has been observed. This result was attributed to the spin filtering when electrons are transmitted through the chiral molecule. The experiment suggests that in a chiral system the overpotential of OER can be decreased by avoiding the singlet energy pathway which forms different peroxides. Indeed, they have shown that the hydrogen peroxide, a side product of water splitting experiment, can be dramatically suppressed by using a chiral catalyst. The mechanism for the hydrogen peroxide formation and mechanism is shown in Figure 1.16. When the spin of the

OH radicals are antiparallel to each other, they combine to form hydrogen peroxide or singlet oxygen; however, if the spin of the radicals are parallel to each other they form ground state triplet oxygen. Due to the CISS effect, in the chiral case the spin polarization in the surface enhances triplet product as compared to singlet product such as hydrogen peroxide and singlet oxygen. While some other chiral catalysts have demonstrated this effect and have shown spin polarized enhancements in OER efficiency, the chirality was imprinted using long organic molecules or chiral materials which are not good water splitting catalysts. Thus, for practical applications, further studies are required on efficient electrocatalysts at different pH regimes to fully explore CISS mediated OER.

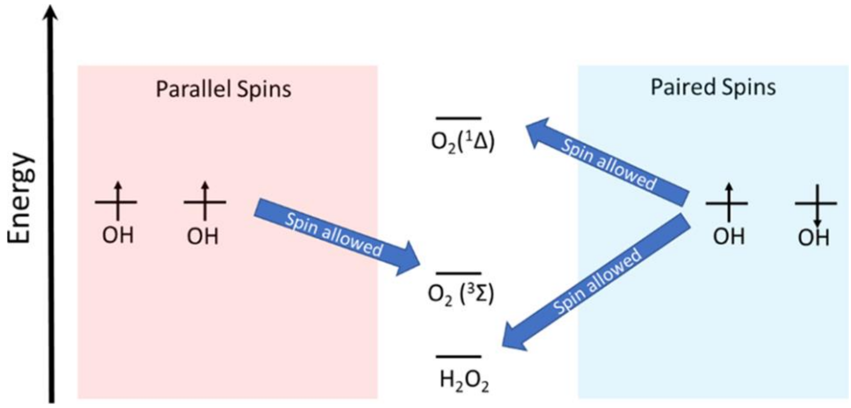

Figure 1.16 Energy diagram showing different products from the combination of OH intermediates during OER.[17] This figure is taken from reference 17.

1.5 DISSERTATION OUTLINE

The CISS effect has already shown great potential in different branches of science. Current studies on CISS effect are mainly focused in three different avenues. Firstly, fundamental understanding of the CISS effect, i.e, why this effect is so robust. Secondly, finding new chiral systems with better spin filtering properties that can be synthesized and fabricated easily for different applications. Thirdly, explore different areas of sciences, where CISS is utilized or can be utilized. The work presented in this dissertation has addresses these by studying spin dependent properties of chiral molecules at the ferromagnetic interface and by exploring spin filtering efficiencies through chiral metal oxide thin films that can be used in electrocatalytic experiments.

Chapter 2 reports our work on chirality induced magnetization of superparamagnetic particles. Asymmetric attachment of chiral molecules on a superparamagnetic iron oxide particle changes the magnetic properties of the particles from superparamagnetic to ferromagnetic. It was also found that magnetization direction of the particles depends on the handedness of the chiral molecules. Importance of symmetry breaking for magnetization was also explored by studying different systems using magnetic force microscopy. This study shows a potential to build memory devices of less than 10 nm size.

Chapter 3 reports the study of spin exchange interaction at chiral molecule ferromagnetic interface. Here Kelvin-probe measurements were used to measure the surface charge of magnetized ferromagnetic thin films coated with self-assembled monolayers (SAM) of chiral molecules. The findings reveal that the electron penetration from the metal electrode into the chiral molecules depends on the magnetization of the ferromagnet and the chirality of the molecule. This study is very important for molecular based spintronics devices.

Chapter 4 demonstrates spin filtering ability of chiral cobalt oxide thin film. Spin polarization study was performed by using magnetic conducting AFM and results show that conduction of electrons depends on the chirality and the magnetization of the tip. A spin-valve based magnetoresistance device was also made using chiral cobalt oxide thin film. The effect of dopant on the spin polarization, where chiral cobalt oxide is doped with Mn ions, also studied. Interestingly, Mn dopant improves the spin polarization. This study shows that chiral metal oxide thin film act as an efficient spin filter and can replace the permanent magnetic layer in the spintronics devices.

Chapter 5 reports our work on electrocatalytic activity with chiral cobalt oxide thin film for water splitting reaction. Chiral catalyst shows much higher efficiency for water splitting than achiral catalyst where a reduction of 65mV at 10 mA/cm^2 in the reaction overpotential was observed with the chiral catalyst. Experiments are also done at different pH and the product formation was evaluated. Effect of magnetic field on the catalytic activity were also studied with a modified paramagnetic catalyst. The importance of spin polarization through the materials that favors the formation of spin-favorable intermediates which facilitates the water splitting efficiency, has been shown.

1.6 REFERENCES

1.Ray, K.; Ananthavel, S. P.; Waldeck, D. H.; Naaman, R., Asymmetric Scattering of Polarized Electrons by Organized Organic Films of Chiral Molecules. *Science* **1999,** *283* (5403), 814.

2.Naaman, R.; Waldeck, D. H., Chiral-Induced Spin Selectivity Effect. *The Journal of Physical Chemistry Letters* **2012,** *3* (16), 2178-2187.

3.Naaman, R.; Waldeck, D. H., Spintronics and Chirality: Spin Selectivity in Electron Transport Through Chiral Molecules. *Annual Review of Physical Chemistry* **2015,** *66* (1), 263-281.

4.Dalum, S.; Hedegård, P., Theory of Chiral Induced Spin Selectivity. *Nano Letters* **2019,** *19* (8), 5253-5259.

5.Guo, A.-M.; Sun, Q.-f., Spin-Selective Transport of Electrons in DNA Double Helix. *Physical Review Letters* **2012,** *108* (21), 218102.

6.Gutierrez, R.; Díaz, E.; Gaul, C.; Brumme, T.; Domínguez-Adame, F.; Cuniberti, G., Modeling Spin Transport in Helical Fields: Derivation of an Effective Low-Dimensional Hamiltonian. *The Journal of Physical Chemistry C* **2013,** *117* (43), 22276-22284.

7.Gutierrez, R.; Díaz, E.; Naaman, R.; Cuniberti, G., Spin-selective transport through helical molecular systems. *Physical Review B* **2012,** *85* (8), 081404.

8.Michaeli, K.; Naaman, R., Origin of Spin-Dependent Tunneling Through Chiral Molecules. *The Journal of Physical Chemistry C* **2019,** *123* (27), 17043-17048.

9.Yeganeh, S.; Ratner, M. A.; Medina, E.; Mujica, V., Chiral electron transport: Scattering through helical potentials. *The Journal of Chemical Physics* **2009,** *131* (1), 014707.

10.Naaman, R.; Paltiel, Y.; Waldeck, D. H., Chiral Induced Spin Selectivity Gives a New Twist on Spin-Control in Chemistry. *Accounts of Chemical Research* **2020,** *53* (11), 2659-2667.

11.Naaman, R.; Paltiel, Y.; Waldeck, D. H., Chiral Molecules and the Spin Selectivity Effect. *The Journal of Physical Chemistry Letters* **2020,** *11* (9), 3660-3666.

12.Banerjee-Ghosh, K.; Ben Dor, O.; Tassinari, F.; Capua, E.; Yochelis, S.; Capua, A.; Yang, S.-H.; Parkin, S. S. P.; Sarkar, S.; Kronik, L.; Baczewski, L. T.; Naaman, R.; Paltiel, Y., Separation of enantiomers by their enantiospecific interaction with achiral magnetic substrates. *Science* **2018,** *360* (6395), 1331.

13.Kumar, A.; Capua, E.; Kesharwani, M. K.; Martin, J. M. L.; Sitbon, E.; Waldeck, D. H.; Naaman, R., Chirality-induced spin polarization places symmetry constraints on biomolecular interactions. *Proceedings of the National Academy of Sciences* **2017,** *114* (10), 2474.

14.Ben Dor, O.; Morali, N.; Yochelis, S.; Baczewski, L. T.; Paltiel, Y., Local Light-Induced Magnetization Using Nanodots and Chiral Molecules. *Nano Letters* **2014,** *14* (11), 6042-6049.

15.Dor, O. B.; Yochelis, S.; Mathew, S. P.; Naaman, R.; Paltiel, Y., A chiral-based magnetic memory device without a permanent magnet. *Nature Communications* **2013,** *4* (1), 2256.

16.Koplovitz, G.; Primc, D.; Ben Dor, O.; Yochelis, S.; Rotem, D.; Porath, D.; Paltiel, Y., Magnetic Nanoplatelet-Based Spin Memory Device Operating at Ambient Temperatures. *Advanced Materials* **2017,** *29* (17), 1606748.

17.Ghosh, K. B.; Zhang, W.; Tassinari, F.; Mastai, Y.; Lidor-Shalev, O.; Naaman, R.; Möllers, P.; Nürenberg, D.; Zacharias, H.; Wei, J.; Wierzbinski, E.; Waldeck, D. H., Controlling Chemical Selectivity in Electrocatalysis with Chiral CuO-Coated Electrodes. *The Journal of Physical Chemistry C* **2019,** *123* (5), 3024-3031.

18.Naaman, R.; Paltiel, Y.; Waldeck, D. H., Chiral Induced Spin Selectivity Gives a New Twist on Spin-Control in Chemistry. *Accounts of Chemical Research* **2020**.

19.Mtangi, W.; Kiran, V.; Fontanesi, C.; Naaman, R., Role of the Electron Spin Polarization in Water Splitting. *The Journal of Physical Chemistry Letters* **2015,** *6* (24), 4916-4922.

20.Ghazaryan, A.; Paltiel, Y.; Lemeshko, M., Analytic Model of Chiral-Induced Spin Selectivity. *The Journal of Physical Chemistry C* **2020,** *124* (21), 11716-11721.

21.Göhler, B.; Hamelbeck, V.; Markus, T. Z.; Kettner, M.; Hanne, G. F.; Vager, Z.; Naaman, R.; Zacharias, H., Spin Selectivity in Electron Transmission Through Self-Assembled Monolayers of Double-Stranded DNA. *Science* **2011,** *331* (6019), 894.

22.Varade, V.; Markus, T.; Vankayala, K.; Friedman, N.; Sheves, M.; Waldeck, D. H.; Naaman, R., Bacteriorhodopsin based non-magnetic spin filters for biomolecular spintronics. *Physical Chemistry Chemical Physics* **2018,** *20* (2), 1091-1097.

23.Mondal, P. C.; Kantor-Uriel, N.; Mathew, S. P.; Tassinari, F.; Fontanesi, C.; Naaman, R., Chiral Conductive Polymers as Spin Filters. *Advanced Materials* **2015,** *27* (11), 1924-1927.

24.Bullard, G.; Tassinari, F.; Ko, C.-H.; Mondal, A. K.; Wang, R.; Mishra, S.; Naaman, R.; Therien, M. J., Low-Resistance Molecular Wires Propagate Spin-Polarized Currents. *Journal of the American Chemical Society* **2019,** *141* (37), 14707-14711.

25.Xie, Z.; Markus, T. Z.; Cohen, S. R.; Vager, Z.; Gutierrez, R.; Naaman, R., Spin Specific Electron Conduction through DNA Oligomers. *Nano Letters* **2011,** *11* (11), 4652-4655.

26.Michaeli, K.; Kantor-Uriel, N.; Naaman, R.; Waldeck, D. H., The electron's spin and molecular chirality – how are they related and how do they affect life processes? *Chemical Society Reviews* **2016,** *45* (23), 6478-6487.

27.Wei, J. J.; Schafmeister, C.; Bird, G.; Paul, A.; Naaman, R.; Waldeck, D. H., Molecular Chirality and Charge Transfer through Self-Assembled Scaffold Monolayers. *The Journal of Physical Chemistry B* **2006,** *110* (3), 1301-1308.

28.Ravi, S.; Sowmiya, P.; Karthikeyan, A., MAGNETORESISTANCE AND SPIN-FILTERING EFFICIENCY OF DNA-SANDWICHED FERROMAGNETIC NANOSTRUCTURES. *SPIN* **2013,** *03* (01), 1350003.

29.Mishra, D.; Markus, T. Z.; Naaman, R.; Kettner, M.; Göhler, B.; Zacharias, H.; Friedman, N.; Sheves, M.; Fontanesi, C., Spin-dependent electron transmission through bacteriorhodopsin embedded in purple membrane. *Proceedings of the National Academy of Sciences* **2013,** *110* (37), 14872.

30.Senthil Kumar, K.; Kantor-Uriel, N.; Mathew, S. P.; Guliamov, R.; Naaman, R., A device for measuring spin selectivity in electron transfer. *Physical Chemistry Chemical Physics* **2013,** *15* (42), 18357-18362.

31.Kiran, V.; Mathew, S. P.; Cohen, S. R.; Hernández Delgado, I.; Lacour, J.; Naaman, R., Helicenes—A New Class of Organic Spin Filter. *Advanced Materials* **2016,** *28* (10), 1957-1962.

32.Mishra, S.; Pirbadian, S.; Mondal, A. K.; El-Naggar, M. Y.; Naaman, R., Spin-Dependent Electron Transport through Bacterial Cell Surface Multiheme Electron Conduits. *Journal of the American Chemical Society* **2019,** *141* (49), 19198-19202.

33.Jia, L.; Wang, C.; Zhang, Y.; Yang, L.; Yan, Y., Efficient Spin Selectivity in Self-Assembled Superhelical Conducting Polymer Microfibers. *ACS Nano* **2020,** *14* (6), 6607-6615.

34.Kulkarni, C.; Mondal, A. K.; Das, T. K.; Grinbom, G.; Tassinari, F.; Mabesoone, M. F. J.; Meijer, E. W.; Naaman, R., Highly Efficient and Tunable Filtering of Electrons' Spin by Supramolecular Chirality of Nanofiber-Based Materials. *Advanced Materials* **2020,** *32* (7), 1904965.

35.Bloom, B. P.; Kiran, V.; Varade, V.; Naaman, R.; Waldeck, D. H., Spin Selective Charge Transport through Cysteine Capped CdSe Quantum Dots. *Nano Letters* **2016,** *16* (7), 4583-4589.

36.Lu, H.; Wang, J.; Xiao, C.; Pan, X.; Chen, X.; Brunecky, R.; Berry, J. J.; Zhu, K.; Beard, M. C.; Vardeny, Z. V., Spin-dependent charge transport through 2D chiral hybrid lead-iodide perovskites. *Science Advances* **2019,** *5* (12), eaay0571.

37.Inui, A.; Aoki, R.; Nishiue, Y.; Shiota, K.; Kousaka, Y.; Shishido, H.; Hirobe, D.; Suda, M.; Ohe, J.-i.; Kishine, J.-i.; Yamamoto, H. M.; Togawa, Y., Chirality-Induced Spin-Polarized State of a Chiral Crystal ${\mathrm{CrNb}}_{3}{\mathrm{S}}_{6}$. *Physical Review Letters* **2020,** *124* (16), 166602.

38.Chatterjee, J.; Haik, Y.; Chen, C.-J., Size dependent magnetic properties of iron oxide nanoparticles. *Journal of Magnetism and Magnetic Materials* **2003,** *257* (1), 113-118.

39.Leslie-Pelecky, D. L.; Rieke, R. D., Magnetic Properties of Nanostructured Materials. *Chemistry of Materials* **1996,** *8* (8), 1770-1783.

40.Bean, C. P.; Livingston, J. D., Superparamagnetism. *Journal of Applied Physics* **1959,** *30* (4), S120-S129.

41.Carmeli, I.; Leitus, G.; Naaman, R.; Reich, S.; Vager, Z., Magnetism induced by the organization of self-assembled monolayers. *The Journal of Chemical Physics* **2003,** *118* (23), 10372-10375.

42.Crespo, P.; Litrán, R.; Rojas, T. C.; Multigner, M.; de la Fuente, J. M.; Sánchez-López, J. C.; García, M. A.; Hernando, A.; Penadés, S.; Fernández, A., Permanent Magnetism, Magnetic Anisotropy, and Hysteresis of Thiol-Capped Gold Nanoparticles. *Physical Review Letters* **2004,** *93* (8), 087204.

43.Yamamoto, Y.; Miura, T.; Suzuki, M.; Kawamura, N.; Miyagawa, H.; Nakamura, T.; Kobayashi, K.; Teranishi, T.; Hori, H., Direct Observation of Ferromagnetic Spin Polarization in Gold Nanoparticles. *Physical Review Letters* **2004,** *93* (11), 116801.

44.Ben Dor, O.; Yochelis, S.; Radko, A.; Vankayala, K.; Capua, E.; Capua, A.; Yang, S.-H.; Baczewski, L. T.; Parkin, S. S. P.; Naaman, R.; Paltiel, Y., Magnetization switching in ferromagnets by adsorbed chiral molecules without current or external magnetic field. *Nature Communications* **2017,** *8* (1), 14567.

45.Bhatti, S.; Sbiaa, R.; Hirohata, A.; Ohno, H.; Fukami, S.; Piramanayagam, S. N., Spintronics based random access memory: a review. *Materials Today* **2017,** *20* (9), 530-548.

46.Buchachenko, A., Recent advances in spin chemistry. *Pure and Applied Chemistry* **2000,** *72*, 2243 - 2258.

47.Buchachenko, A. L.; Berdinsky, V. L., Spin Catalysis of Chemical Reactions. *The Journal of Physical Chemistry* **1996,** *100* (47), 18292-18299.

48.Hore, P. J.; Ivanov, K. L.; Wasielewski, M. R., Spin chemistry. *The Journal of Chemical Physics* **2020,** *152* (12), 120401.

49.Colvin, M. T.; Ricks, A. B.; Scott, A. M.; Smeigh, A. L.; Carmieli, R.; Miura, T.; Wasielewski, M. R., Magnetic Field-Induced Switching of the Radical-Pair Intersystem Crossing Mechanism in a Donor−Bridge−Acceptor Molecule for Artificial Photosynthesis. *Journal of the American Chemical Society* **2011,** *133* (5), 1240-1243.

50.Hore, P. J.; Mouritsen, H., The Radical-Pair Mechanism of Magnetoreception. *Annual Review of Biophysics* **2016,** *45* (1), 299-344.

51.Lee, J. H.; Okuno, Y.; Cavagnero, S., Sensitivity enhancement in solution NMR: Emerging ideas and new frontiers. *Journal of Magnetic Resonance* **2014,** *241*, 18-31.

52.Levitt, M. H., Singlet Nuclear Magnetic Resonance. *Annual Review of Physical Chemistry* **2012,** *63* (1), 89-105.

53.Wohlgenannt, M., Organic magnetoresistance and spin diffusion in organic semiconductor thin film devices. *physica status solidi (RRL) – Rapid Research Letters* **2012,** *6* (6), 229-242.

54.Steiner, U. E.; Ulrich, T., Magnetic field effects in chemical kinetics and related phenomena. *Chemical Reviews* **1989,** *89* (1), 51-147.

55.Evans, E. W.; Dodson, C. A.; Maeda, K.; Biskup, T.; Wedge, C. J.; Timmel, C. R., Magnetic field effects in flavoproteins and related systems. *Interface Focus* **2013,** *3* (5), 20130037.

56.Jones, A. R., Magnetic field effects in proteins. *Molecular Physics* **2016,** *114* (11), 1691-1702.

57.Chrétien, S.; Metiu, H., O2 evolution on a clean partially reduced rutile TiO2(110) surface and on the same surface precovered with Au1 and Au2: The importance of spin conservation. *The Journal of Chemical Physics* **2008,** *129* (7), 074705.

58.Guo, D.; Knight, T. E.; McCusker, J. K., Angular Momentum Conservation in Dipolar Energy Transfer. *Science* **2011,** *334* (6063), 1684.

59.Metzger, T. S.; Mishra, S.; Bloom, B. P.; Goren, N.; Neubauer, A.; Shmul, G.; Wei, J.; Yochelis, S.; Tassinari, F.; Fontanesi, C.; Waldeck, D. H.; Paltiel, Y.; Naaman, R., The Electron Spin as a Chiral Reagent. *Angewandte Chemie International Edition* **2020,** *59* (4), 1653-1658.

60.Mtangi, W.; Tassinari, F.; Vankayala, K.; Vargas Jentzsch, A.; Adelizzi, B.; Palmans, A. R. A.; Fontanesi, C.; Meijer, E. W.; Naaman, R., Control of Electrons' Spin Eliminates Hydrogen Peroxide Formation During Water Splitting. *Journal of the American Chemical Society* **2017,** *139* (7), 2794-2798.

61.Zhang, W.; Banerjee-Ghosh, K.; Tassinari, F.; Naaman, R., Enhanced Electrochemical Water Splitting with Chiral Molecule-Coated Fe3O4 Nanoparticles. *ACS Energy Letters* **2018,** *3* (10), 2308-2313.

62.Lee, Y.; Suntivich, J.; May, K. J.; Perry, E. E.; Shao-Horn, Y., Synthesis and Activities of Rutile IrO2 and RuO2 Nanoparticles for Oxygen Evolution in Acid and Alkaline Solutions. *The Journal of Physical Chemistry Letters* **2012,** *3* (3), 399-404.

63.Song, F.; Bai, L.; Moysiadou, A.; Lee, S.; Hu, C.; Liardet, L.; Hu, X., Transition Metal Oxides as Electrocatalysts for the Oxygen Evolution Reaction in Alkaline Solutions: An Application-Inspired Renaissance. *Journal of the American Chemical Society* **2018,** *140* (25), 7748-7759.

64.Deng, X.; Tüysüz, H., Cobalt-Oxide-Based Materials as Water Oxidation Catalyst: Recent Progress and Challenges. *ACS Catalysis* **2014,** *4* (10), 3701-3714.

65.Dau, H.; Limberg, C.; Reier, T.; Risch, M.; Roggan, S.; Strasser, P., The Mechanism of Water Oxidation: From Electrolysis via Homogeneous to Biological Catalysis. *ChemCatChem* **2010,** *2* (7), 724-761.

66.Suen, N.-T.; Hung, S.-F.; Quan, Q.; Zhang, N.; Xu, Y.-J.; Chen, H. M., Electrocatalysis for the oxygen evolution reaction: recent development and future perspectives. *Chemical Society Reviews* **2017,** *46* (2), 337-365.

67.Torun, E.; Fang, C. M.; de Wijs, G. A.; de Groot, R. A., Role of Magnetism in Catalysis: RuO2 (110) Surface. *The Journal of Physical Chemistry C* **2013,** *117* (12), 6353-6357.

68.Gracia, J., Spin dependent interactions catalyse the oxygen electrochemistry. *Physical Chemistry Chemical Physics* **2017,** *19* (31), 20451-20456.

69.Sharpe, R.; Lim, T.; Jiao, Y.; Niemantsverdriet, J. W.; Gracia, J., Oxygen Evolution Reaction on Perovskite Electrocatalysts with Localized Spins and Orbital Rotation Symmetry. *ChemCatChem* **2016,** *8* (24), 3762-3768.

70.Sharpe, R.; Munarriz, J.; Lim, T.; Jiao, Y.; Niemantsverdriet, J. W.; Polo, V.; Gracia, J., Orbital Physics of Perovskites for the Oxygen Evolution Reaction. *Topics in Catalysis* **2018,** *61* (3), 267-275.

71.Garcés-Pineda, F. A.; Blasco-Ahicart, M.; Nieto-Castro, D.; López, N.; Galán-Mascarós, J. R., Direct magnetic enhancement of electrocatalytic water oxidation in alkaline media. *Nature Energy* **2019,** *4* (6), 519-525.

2.0 SINGLE DOMAIN 10 nm FERROMAGNETISM IMPRINTED ON SUPERPARAMAGNETIC NANOPARTICLES USING CHIRAL MOLECULES

This work was published as Koplovitz, E.; Leitus, G.; Ghosh, S.; Bloom, B. P.; Yochelis, S.; Rotem, D.; Vischio, F.; Striccoli, M.; Elisabetta, F.; Naaman, R.; Waldeck, D. H.; Porath, D.; Paltiel, Y. *Small* **2019**, 15, 1804557. The author of the dissertation performed the nanoparticle synthesis, the design of the experiments, the magnetic force microscopy measurement, and participated in writing the manuscript. The supporting information for this chapter can be found in Appendix A.

The rapid growth in demand for data and the emerging applications of Big Data requires the increase of memory capacity. Magnetic memory devices are among the leading technologies for meeting this demand; however, they rely on the use of ferromagnets that creates size reduction limitations and poses complex materials requirements. Usually, magnetic memory sizes are limited to 30-50 nm. Reducing the size even further, to the ~10-20 nm scale, destabilizes the magnetization and its magnetic orientation becomes susceptible to thermal fluctuations and stray magnetic fields. In the present work it is shown that 10 nm single domain ferromagnetism can be achieved. Using asymmetric adsorption of chiral molecules superparamagnetic iron oxide nanoparticles become ferromagnetic with an average coercive field of ~ 80 Oe. The asymmetric absorption of molecules stabilizes the magnetization direction at room temperature and the orientation is found to depend on the handedness of the chiral molecules. These studies point to a novel method for the miniaturization of ferromagnets (down to ~10 nm) using established synthetic protocols.

2.1 INTRODUCTION

The rapid growth in demand for data (such as videos, pictures and audio) and the emerging applications of Big Data require the increase of memory capacity, as well as faster and more energy efficient non-volatile memory devices. Spintronic based magnetic memory devices are among the leading technologies for meeting this demand.[1-3] Spintronics technology is already industrialized and widely used in devices such as hard disk drives and magnetic random access memory.[4] All spintronic devices require the use of magnetic materials as the memory storage medium and for generating spin polarized currents. The use of ferromagnets for producing the spin current creates size reduction limitations and poses complex materials requirements.[3, 4]

The size reduction limitation arises from the physicochemical nature of the materials, specifically ferromagnets (FM), whose magnetic properties are comprised from their magnetic domains at smaller sizes. Typically, magnetic domains in a ferromagnet are a micron in size, so that reducing the size to ~50 nm scale creates a single magnetic domain with high coercivity. The exact location of the transition from multiple domain to single domain of Fe_3O_4 depends on both size and shape. For example, in cuboidal particles the critical diameter for forming a multi-domain structure has been theoretically and experimentally determined to be 76 nm[5] and for spherical Fe_3O_4 nanoparticles the theoretical critical diameter was found to be 128 nm.[6] Reducing the size of the material even further destabilizes the magnetization and its magnetic orientation becomes susceptible to thermal fluctuations and weak stray magnetic fields. At small enough sizes, the material enters the superparamagnetic regime, ~10-20 nm scale, with zero coercivity and no magnetic remanence (Figure 2.1a ,b).[7] Thus, the reduction in size of magnetic memory devices and magnetic reading heads is usually limited to a 30-50 nm size regime.[8]

In recent works it was shown that simple spintronic devices without magnetic layers could be realized using the Chiral Induced Spin Selectivity (CISS) effect.[9, 10] The CISS effect provides an easy and efficient way to generate a spin polarized current that is either parallel or anti-parallel to the electrons' velocity; in addition, it correlates with the handedness of the chiral molecules. Using the CISS effect, new types of simple spintronic memory devices and a nanoscale memristor have been demonstrated.[11-14]

The adsorption of chiral molecules on a metal surface has been shown to change the metal's magnetic properties[15-18] and also switch the magnetization direction of a soft FM in a way that depends on the handedness of the chiral molecules.[19] This effect was named the magnetism induced by proximity of adsorbed chiral molecules (MIPAC). The MIPAC effect arises from the CISS effect, i.e., the spin-dependent electron fluctuations in chiral molecules. For right-handed (left-handed) chiral molecules electrons with a preferred spin up (down) move upward through the molecule and electrons with a preferred spin down (up) move downward through the molecule (Figure 2.1 c). In a semiclassical picture, placing chiral molecules with these charge oscillations in contact with a metal induces a magnetic moment in the metal by spin torque transfer.[20-22] In a more quantum picture, the proximity induced wavefunction delocalization of surface states occurs upon surface modification,[23, 24] and the wavefunction penetration into the chiral molecules is spin dependent because of the CISS effect. This phenomenon induces a non-symmetric density of states in the material, which is equivalent to magnetization of a ferromagnetic. Note that these works show that chiral molecules can reorder magnetization or induce paramagnetism. However no reports claimed that superparamagnetism can be changed to ferromagnetism.

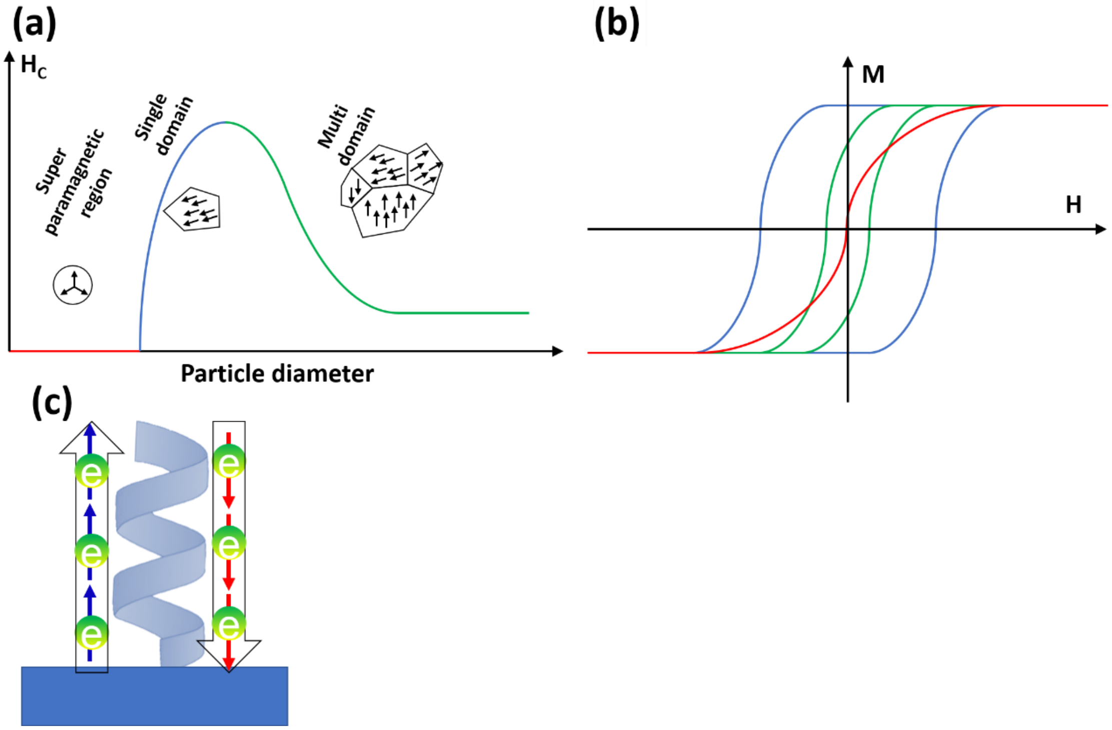

Figure 2.1 Panel (a) shows the generic dependence of a magnetic material (FM in the bulk) on the reduction physical size: multidomain (green), single domain (blue) and super paramagnetism (red). Panel (b) shows magnetization hysteresis loops for the different domain size behaviors. Panel (c) illustrates the CISS effect in which a right-handed chiral molecule has preference for spin up to move upward and for spin down to move downward.

In the present work we show that chiral molecules can change the magnetic properties of 10 nm iron oxide nanoparticles from superparamagnetic to ferromagnetic, thus realizing 10 nm chiral induced ferromagnetic iron oxide nanoparticles (CIFIONs). These CIFIONs present ferromagnetic properties even at 10nm size. The anisotropic placement of the chiral molecules stabilize the nanoparticles magnetization direction at room temperature and the orientation depends on the handedness of the chiral molecules. These studies point to a novel method for the miniaturization of well-defined ferromagnets (~10 nm) using established synthetic protocols for superparamagnetic iron oxide nanoparticles (SPIONs).

2.2 RESULTS AND DISCUSSION

2.2.1 Sample Preparation

In this work we used ~10 nm spherical SPIONs capped by oleic acid, oleylamine, and 1,2 dodecanediol in a chloroform solution, which were synthesized following a previously reported procedure.[27,28] Figure 2.2a shows a representative TEM image of the as synthesized SPIONs. As a reference we also used SPIONs caped by L-tartaric acid molecules in water solution (Figure A.1, Appendix A).

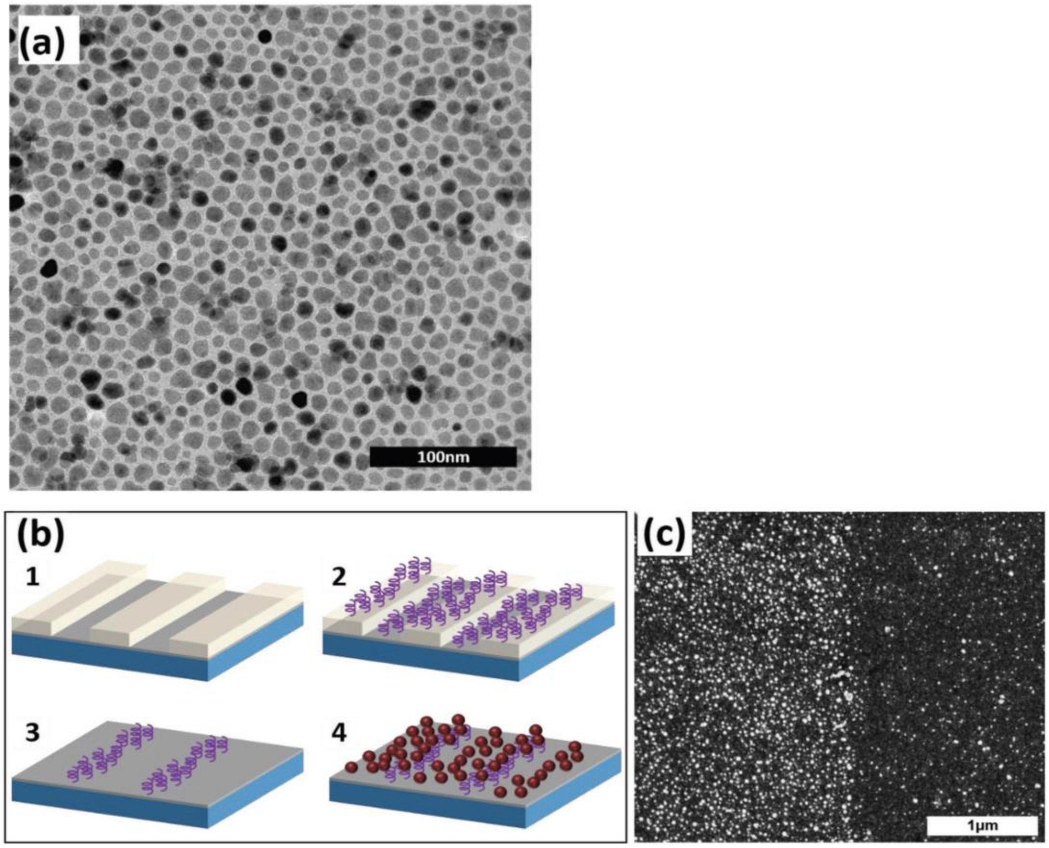

Figure 2.2 a) Transmission electron microscope image of the ≈10 nm SPIONs. b) Illustration of the M-AFM samples patterning of the AHPA-SAM on a 100 nm Ag (gray layer) evaporated on 4 × 4 mm2 Si chip (blue layer). 1-the resist pattern. 2-AHPA-SAM (purple helical molecules) formation. 3-Resist lift-off, AHPA-SAM was left only where there was no resist. 4-iron oxide nanoparticle (red spheres) adsorption. c) Scanning electron microscope image on the border between an area with AHPA-SAM (left side) and an area without (right side). The iron oxide density is much higher on the AHPA-SAM because of the carboxylic terminal group of the AHPA molecule which binds to iron oxide.

Right-handed (L) and left-handed (D) α-helix polyalanine (AHPA) were used as the chiral molecules to imprint a magnetization on the iron oxide nanoparticles. The chiral molecules were purchased from Sigma Aldrich Co. LLC, with a sequence of 36 amino acids of [H]-CAAAAKAAAAKAAAAKAAAAKAAAAKAAAAKAAAAK-[OH] where C, A, and K are cysteine, alanine, and lysine amino acids respectively. The AHPA molecules are terminated with a thiol group from the cysteine amino acid and a carboxylic terminal group through the last lysine residue. The thiol is used to covalently bind the AHPA molecules to metal surfaces such as gold and silver and the carboxylic group was used to bind and immobilize the SPIONs.

Measurement of the magnetization imprinting effect on the SPIONs by the AHPA molecules were performed with a superconducting quantum interference device (SQUID) and by using magnetic atomic force microscopy (M-AFM). For both types of measurements, the sample consisted of a monolayer film of SPIONs supported by a self-assembled monolayer (SAM) of L- or D- AHPA, on a 100 nm Ag film. For the M-AFM measurement, additional lithography was performed to pattern AHPA-SAM areas with lift-off assisted selective adsorption (Figure 2.2b outlines this procedure) in order to compare SPIONs with and without chiral molecules in the same M-AFM image. M-AFM measurements were obtained by taking interleaved topography and magnetic interaction images using a cobalt alloy coated tip (coercive field of ~300 Oe, K~2.8 N/m, F~75 KHz) which was magnetized either normal (up) or anti-normal (down) to the substrate with a 5000 Oe magnetic field. Scanning electron microscopy images taken at the border between an AHPA-SAM (left side) and bare silver (right side) show that a higher particle density is present on the AHPA-SAM areas (Figure 2.2c). The higher SPION density is attributed to the carboxylic terminal group of the AHPA molecule.

For the M-AFM measurements, two additional reference samples were prepared. The first reference sample had only SPIONs on Ag (without AHPA). The second reference sample used SPIONs that were coated from all directions with L-tartrate (or D-tartrate) ligands and placed on a mica substrate, to check the importance of symmetry breaking.

Preparation and measurements details of all samples are available in the Appendix. A section.

2.2.2 SQUID Measurement

Magnetic moment measurements of SPIONs adsorbed on L- AHPA molecules (Figure 2.3a) were performed using a SQUID, and the magnetization hysteresis loop was obtained (Figure 2.3b) by subtracting the response of a clean Ag substrate (Figure A.3 in the Appendix A).

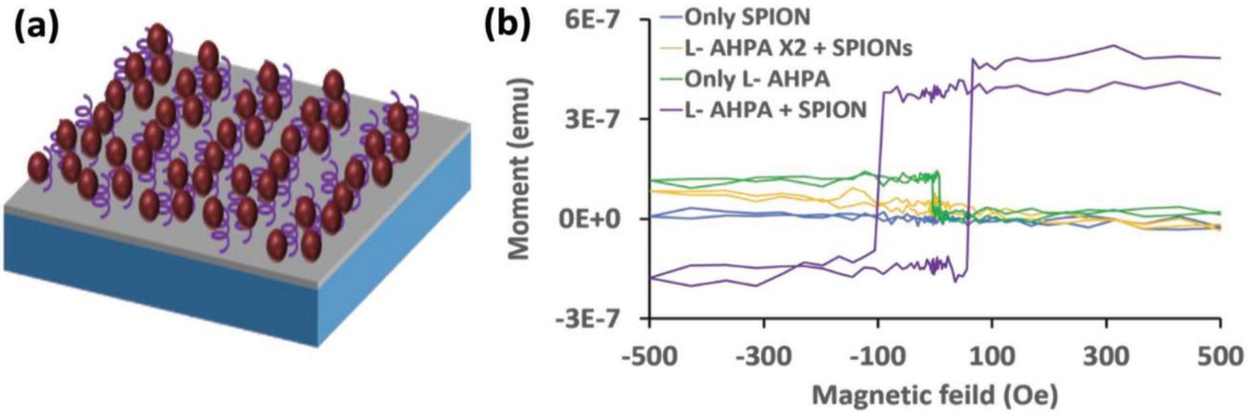

Figure 2.3 Illustration of the sample for the SQUID measurements: 100 nm Ag (gray layer) evaporated on 4 × 4 mm2 Si chip (blue layer). SAM of AHPA chiral molecules (purple helical molecules) was adsorbed on the Ag layer and iron oxide nanoparticles (red spheres) were adsorbed on top of the AHPA-SAM. b) SQUID measurements of the magnetization hysteresis loop. The sample of L-AHPA with iron oxide nanoparticles (purple line) showsCIFIONs with a hysteresis loop exhibiting ferromagnetic behavior with an average coercive field of ≈80 Oe. The hysteresis loop is not symmetric around zero and shows a preference to magnetize the CIFIONs in the upward direction. Three reference samples were measured. The first of L-AHPA X2 with chiral molecules adsorbed on both sides of the iron oxide nanoparticles (orange line) display no measurable response. The second of only L-AHPA (without nanoparticles, green line) shows weak magnetic order and no hysteresis is measured. In this case, the adsorption of chiral molecules from one side also seem to generate some small substrate magnetic ordering. The third reference sample of only iron oxide nanoparticles (without AHPA, blue line) presents no measurable response.

The SPIONs by themselves do not show significant magnetization when deposited on an Ag substrate (blue). The adsorption of chiral molecules on the Ag substrate generates a weak additional magnetism (green), which may arise from chiral imprinting.[21]

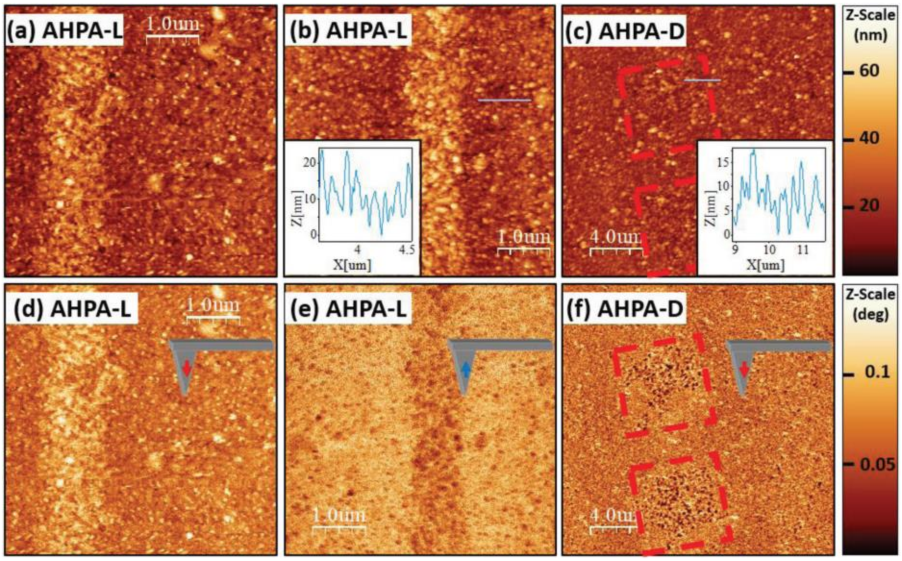

Figure 2.4 Panels (a-c) show topography images that were taken and interleaved with the magnetic interaction images (tip distance of 130 nm) in panels (d–f). Topography and phase color scales are on the respective right sides of the images. The M-AFM tip was magnetized down (red arrow), or up (blue arrows). In panels (d) and (e) an L-AHPA-SAM (right-handed), the substrate, is patterned with lines and shows that the iron oxide nanoparticles are magnetized upward. The tip experiences repulsive interactions for downward tip magnetization and attractive interactions for upward tip magnetization, as indicated by the bright and dark colors. In panel (f), D-AHPA-SAM (left handed) has a square patterned surface (red squares) and the darker color shows that the iron oxide nanoparticles are magnetized downward due to attractive magnetic interactions with a downward magnetized M-AFM tip. The insets in panels (b) and (c) show topographic cross sections**.**

Interestingly, when the SPIONs are deposited on the L-AHPA-SAM the hysteresis loop inverts and a stronger magnetization is recorded (purple). Despite the intrinsic property of SPIONs to be superparamagnetic, i.e., zero coercivity and no remanence field, upon their adsorption on chiral molecules, they transform into CIFIONs with a ferromagnetic hysteresis loop and average coercive field of ~80 Oe. The hysteresis loop is not symmetric around zero and shows a preference to magnetize the CIFIONs in the upward direction. All measurements were repeated on three samples.

To relate this effect to the adsorption of chiral molecules from one side only, a reference sample with an additional L- AHPA-SAM adsorbed on top of the SPIONs, named L- AHPA X2 (the SPIONs are now embedded between two layers of L- AHPA molecules), was prepared. Figure A.2 in the Appendix A illustrates the preparation. In this case, no significant magnetization was measured (orange); it was similar to the measurement with only SPIONs deposited on silver. The hysteresis loop is not symmetric around zero and shows a preference to magnetize the CIFIONs in the upward direction. The flip from upward to downward magnetization occurs at ~ -95 Oe whereas the flip from downward to upward magnetization occurs at ~ 60 Oe. In all of the reference samples (without the SPIONs) the hysteresis was below the noise level. It is interesting to note that the magnetic moment seems to be symmetric around the L- AHPA curve. It is clear that the chiral molecules impart some magnetization onto the substrate, which may give rise to the asymmetry around zero magnetic field.

2.2.3 Magnetic Force Microscopy (M-AFM) Measurement

Figure 2.4 shows the results of the M-AFM measurements. For the L- AHPA (right-handed helix) the SAM was patterned into stripes (topography images are shown in Figure 2.4a,b and magnetic interaction images are shown in Figure 2.4d, e for downward and upward magnetization of the M-AFM tip, respectively). When magnetizing the M-AFM tip downward (red arrow), a repulsive magnetic interaction is measured (bright features), and for an upward magnetized tip (blue arrow), an attractive magnetic interaction is observed (dark features). This behavior demonstrates that the CIFIONs are magnetized with an upward orientation. For D-AHPA (left-handed helices) the SAM was patterned into squares; the topography image is shown in Figure 2.4c and the magnetic interaction image for downward magnetization of the M-AFM tip is shown in Figure 2.4f. In this case, an attractive interaction dominates which indicates that the CIFIONs are magnetized with a downward orientation. This observation stands in contrast to Figure 2.4d in which L-AHPA CIFION samples, probed with the same tip magnetization, show the opposite behavior. Thus, the chirality of the AHPA SAM controls the orientation of the magnetization of the iron oxide nanoparticles. Similar measurements are presented for a single nanoparticle in the Figure A.4 in Appendix A.

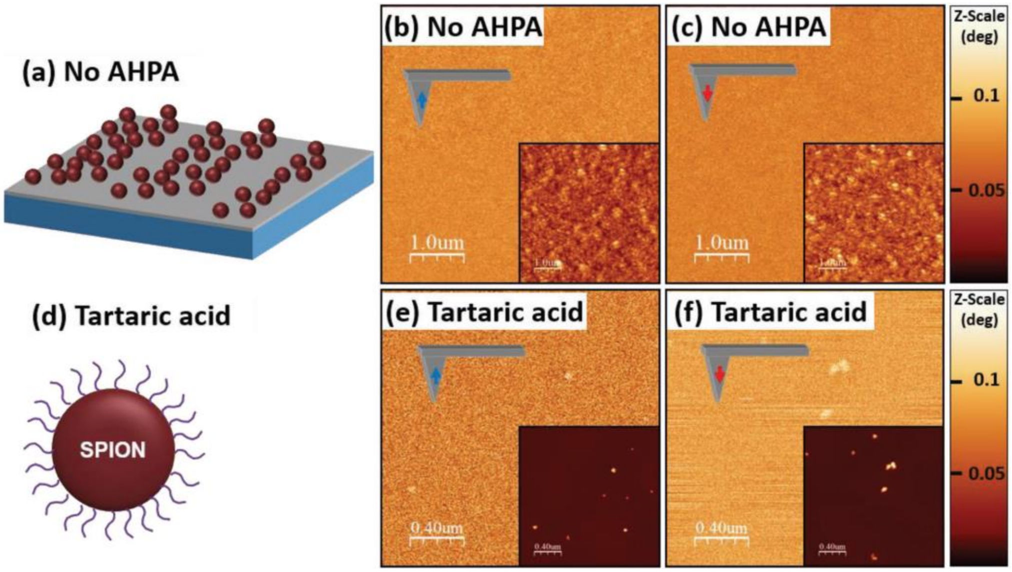

Figure 2.5 a) Illustration of the SPIONs with no chiral molecule reference sample. b,c) Magnetic interaction measurements of SPIONs on Ag without chiral molecules. There is no measurable signal for both M-AFM tip magnetizations (upward and downward) although there are SPIONs as can be seen in the topography images (insets). d) Illustration of SPION covered, from all directions, with left-handed chirality tartaric acid. e,f) Magnetic interaction measurements of tartaric acid covered SPIONs on a mica substrate. For both tip magnetization (upward and downward), there is a repulsive magnetic interaction, which correlates to the SPIONs seen in the topography images (insets).

Two additional reference systems were investigated using M-AFM. The first reference measured the magnetic interaction of SPIONs physically adsorbed on an Ag layer without any chiral molecules (Figure 2.5a, b, c and see Figure A.5 in Appendix A for topography cross section images). These data fail to generate a discernable magnetic response above the background. In the second system SPIONs were covered on all sides with L-tartaric acid and were measured by the MFM method on a mica surface (Figure 2.5d, e, f). These nanoparticles displayed a random magnetization direction. Additional images for L- and D-tartaric acid SPIONs on SiO_2 and statistical analysis thereof are shown in Figure A.6 in Appendix A.

The experimental results indicate that the chiral molecules change the magnetic properties of SPIONs from superparamagnetic, which has zero coercive field and no remanence, to ferromagnetic CIFIONs, which have a nonzero coercive field and display remanence. The SQUID measurements exhibit a significant ferromagnetic hysteresis loop for CIFIONs on an AHPA-SAM with an average coercive field of ~80 Oe, while the reference measurements of only SPIONs or only AHPA-SAMs show no hysteresis loops and much weaker magnetic signals (Figure 2.3b). The hysteresis loop is also not symmetric around zero magnetic field, which indicates that magnetization of the CIFIONs in the upward direction requires a lower absolute magnetic field than in the downward direction for the right-handed helical molecules (L- AHPA).

The M-AFM measurements show that the CIFIONs on an L-AHPA SAM have attractive or repulsive magnetic interactions with the M-AFM tip when the tip is magnetized in the down and up orientations, respectively. This dependence is reversed for CIFIONs on a D-AHPA SAM (Figure 2.4f). These results corroborate the SQUID measurements by showing that the functionalized iron oxide nanoparticles exhibit a stable magnetization, which is robust to thermal fluctuations and displays a significant coercive field and remanence (in contrast to a nanoparticle with superparamagnetic behavior). The measurements also show that the orientation of the CIFION magnetization is controlled by the chirality of the SAM molecules.

2.2.4 Mechanism of Magnetization Imprinting

We ascribe the chiral based magnetization imprinting on the SPIONs to chiral induced spin selectivity at the chiral molecule-iron oxide interface. An electron exchange current flows between the iron oxide nanoparticles and the Ag substrate by way of the chiral molecules, and the forward and reverse current are spin filtered by the chiral molecules. The spin preference is determined by the helicity of the chiral molecule; for right-handed (left-handed) chiral molecules spin up (down) electrons will be preferentially transmitted to the molecule while spin down (up) electrons will be preferentially transferred down the molecule. This process results in a majority spin up population in the nanoparticle and stabilizes the magnetization in the upward direction (Figure 2.6a). The opposite magnetization of the iron oxide nanoparticle is observed when the chirality of helical molecules is reversed (Figure 2.6b). In the case of a SPION covered by chiral molecules from all directions or embedded between two SAMs of the same handedness, the symmetry plane is not broken and no net stable magnetization is observed; an electron with one type of spin will transfer into the SPION from the bottom interface with chiral molecules, while the interface at the top of the SPION will transfer electrons of the opposite spin type (Figure 2.6c).

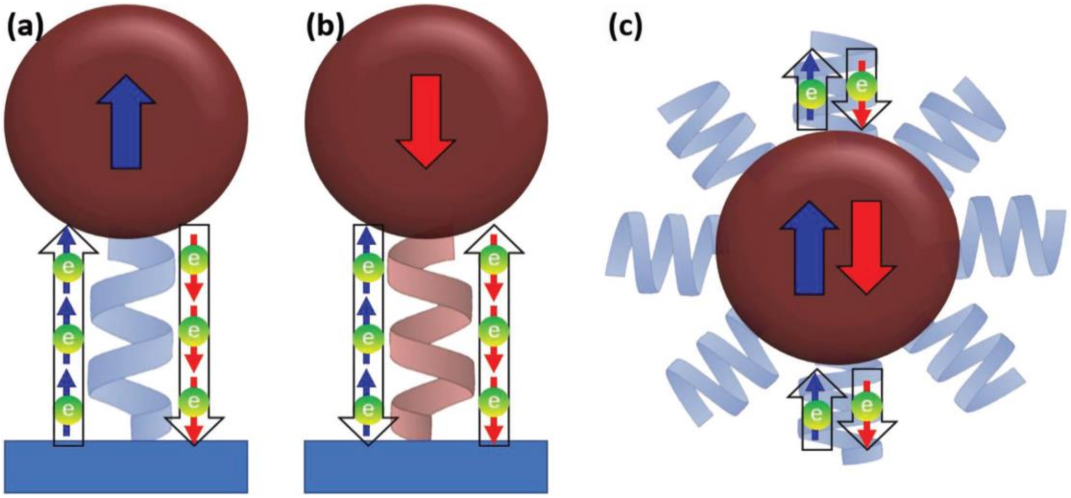

Figure 2.6 Panels (a) and (b) show right-handed and left-handed chiral molecules, respectively, linked only to the bottom side of the iron oxide nanoparticle. Because of the CISS effect, spin up (down) electrons are preferentially going into the nanoparticle, while spin down (up) electrons are preferentially going out of the nanoparticle creating majority spin up (down) electrons in the nanoparticle. This process creates a net magnetization of the nanoparticle with a defined upward (downward) orientation. Panel (c) shows a right-handed chiral molecule linked to the iron oxide nanoparticle from all directions. In this case, spin up (down) electrons are going into the nanoparticle from the bottom (top) chiral molecule and going out of the nanoparticle from the top (bottom) molecule, resulting in unstable magnetization.

Measurements (both SQUID and M-AFM) of the reference samples of SPIONs without chiral molecules do not show magnetization and substantiate the role of chiral induced spin selective transport for the magnetization imprinting. The magnetic interaction measurements on chiral tartaric acid coated SPIONs indicate that achieving strong magnetization imprinting requires anisotropic coverage e.g. a defined orientation for spin flow.

2.3 SUMMARY

Using SQUID and M-AFM measurements, we have shown how ferromagnetic properties can be imprinted on 10 nm SPIONs. This size reduction should enable the scale down of magnetic memory area by an order of magnitude and may prove to be important to magnetic force microscopy as well. These magnetic chiral iron oxide nanoparticles manifest remanence and an average coercive field of ~80 Oe at room temperature. In addition, the preferred magnetization direction is determined by the chirality of the molecules and their nonsymmetrical placement around the nanoparticle. We propose a mechanism for the chiral imprinting that is based on the well-established CISS effect; namely, magnetism induced by proximity of adsorbed chiral molecules. This explanation suggests that the ferromagnetic properties are imprinted when the chiral molecules are bound on one side of the SPIONs and should disappear when the SPIONs are covered with chiral molecules from two opposite faces, or from all directions. Measurements of SPIONs covered with chiral molecules from two or all directions indeed showed no remanence and zero coercive field. The results indicate that magnetic based devices (especially spintronic devices) can be further miniaturized using chiral-based magnetization imprinting and that magnetic nanomaterials could be magnetized using chemical adsorption, without an external magnetic field and without applying spin-polarized current.

2.4 REFERENCES

1.Guth, M.; Schmerber, G.; Dinia, A., Magnetic tunnel junctions for magnetic random access memory applications. *Materials Science and Engineering: C* **2002,** *19* (1), 129-133.

2.Bhatti, S.; Sbiaa, R.; Hirohata, A.; Ohno, H.; Fukami, S.; Piramanayagam, S. N., Spintronics based random access memory: a review. *Materials Today* **2017,** *20* (9), 530-548.

3.Hwang, C. S., Prospective of Semiconductor Memory Devices: from Memory System to Materials. *Advanced Electronic Materials* **2015,** *1* (6), 1400056.

4.Kawahara, T.; Ito, K.; Takemura, R.; Ohno, H., Spin-transfer torque RAM technology: Review and prospect. *Microelectronics Reliability* **2012,** *52* (4), 613-627.

5.Li, Q.; Kartikowati, C. W.; Horie, S.; Ogi, T.; Iwaki, T.; Okuyama, K., Correlation between particle size/domain structure and magnetic properties of highly crystalline Fe3O4 nanoparticles. *Scientific Reports* **2017,** *7* (1), 9894.

6.Leslie-Pelecky, D. L.; Rieke, R. D., Magnetic Properties of Nanostructured Materials. *Chemistry of Materials* **1996,** *8* (8), 1770-1783.

7.Teja, A. S.; Koh, P.-Y., Synthesis, properties, and applications of magnetic iron oxide nanoparticles. *Progress in Crystal Growth and Characterization of Materials* **2009,** *55* (1), 22-45.

8.Hirohata, A.; Takanashi, K., Future perspectives for spintronic devices. *Journal of Physics D: Applied Physics* **2014,** *47* (19), 193001.

9.Naaman, R.; Waldeck, D. H., Chiral-Induced Spin Selectivity Effect. *The Journal of Physical Chemistry Letters* **2012,** *3* (16), 2178-2187.

10.Naaman, R.; Waldeck, D. H., Spintronics and Chirality: Spin Selectivity in Electron Transport Through Chiral Molecules. *Annual Review of Physical Chemistry* **2015,** *66* (1), 263-281.

11.Ben Dor, O.; Yochelis, S.; Radko, A.; Vankayala, K.; Capua, E.; Capua, A.; Yang, S.-H.; Baczewski, L. T.; Parkin, S. S. P.; Naaman, R.; Paltiel, Y., Magnetization switching in ferromagnets by adsorbed chiral molecules without current or external magnetic field. *Nature Communications* **2017,** *8* (1), 14567.

12.Dor, O. B.; Yochelis, S.; Mathew, S. P.; Naaman, R.; Paltiel, Y., A chiral-based magnetic memory device without a permanent magnet. *Nature Communications* **2013,** *4* (1), 2256.

13.Koplovitz, G.; Primc, D.; Ben Dor, O.; Yochelis, S.; Rotem, D.; Porath, D.; Paltiel, Y., Magnetic Nanoplatelet-Based Spin Memory Device Operating at Ambient Temperatures. *Advanced Materials* **2017,** *29* (17), 1606748.

14.Al-Bustami, H.; Koplovitz, G.; Primc, D.; Yochelis, S.; Capua, E.; Porath, D.; Naaman, R.; Paltiel, Y., Single Nanoparticle Magnetic Spin Memristor. *Small* **2018,** *14* (30), 1801249.

15.Carmeli, I.; Leitus, G.; Naaman, R.; Reich, S.; Vager, Z., Magnetism induced by the organization of self-assembled monolayers. *The Journal of Chemical Physics* **2003,** *118* (23), 10372-10375.

16.Crespo, P.; Litrán, R.; Rojas, T. C.; Multigner, M.; de la Fuente, J. M.; Sánchez-López, J. C.; García, M. A.; Hernando, A.; Penadés, S.; Fernández, A., Permanent Magnetism, Magnetic Anisotropy, and Hysteresis of Thiol-Capped Gold Nanoparticles. *Physical Review Letters* **2004,** *93* (8), 087204.

17.Hernando, A.; Crespo, P.; García, M. A., Origin of Orbital Ferromagnetism and Giant Magnetic Anisotropy at the Nanoscale. *Physical Review Letters* **2006,** *96* (5), 057206.

18.Yamamoto, Y.; Miura, T.; Suzuki, M.; Kawamura, N.; Miyagawa, H.; Nakamura, T.; Kobayashi, K.; Teranishi, T.; Hori, H., Direct Observation of Ferromagnetic Spin Polarization in Gold Nanoparticles. *Physical Review Letters* **2004,** *93* (11), 116801.

19.Ben Dor, O.; Morali, N.; Yochelis, S.; Baczewski, L. T.; Paltiel, Y., Local Light-Induced Magnetization Using Nanodots and Chiral Molecules. *Nano Letters* **2014,** *14* (11), 6042-6049.

20.Berger, L., Emission of spin waves by a magnetic multilayer traversed by a current. *Physical Review B* **1996,** *54* (13), 9353-9358.

21.Ralph, D. C.; Stiles, M. D., Spin transfer torques. *Journal of Magnetism and Magnetic Materials* **2008,** *320* (7), 1190-1216.

22.Slonczewski, J. C., Current-driven excitation of magnetic multilayers. *Journal of Magnetism and Magnetic Materials* **1996,** *159* (1), L1-L7.

23.Kisielewski, M.; Maziewski, A.; Kurant, Z.; Tekielak, M.; Wawro, A.; Baczewski, L. T., Magnetic ordering in ultrathin cobalt film covered by an overlayer of noble metals. *Journal of Applied Physics* **2003,** *93* (10), 7628-7630.

24.Kisielewski, M.; Maziewski, A.; Tekielak, M.; Wawro, A.; Baczewski, L. T., New Possibilities for Tuning Ultrathin Cobalt Film Magnetic Properties by a Noble Metal Overlayer. *Physical Review Letters* **2002,** *89* (8), 087203.

3.0 EFFECT OF CHIRAL MOLECULES ON THE ELECTRON'S SPIN WAVEFUNCTION AT INTERFACES

This work was published as Ghosh, S.; Mishra, S.; Avigad, E.; Bloom, B. P.; Baczewski, L. T.; Yochelis, S.; Paltiel, Y.; Naaman, R.; Waldeck, D. H. *J. Phys. Chem. Lett*, **2020**, 11(4), 1550-1557. The author of the dissertation performed the Kelvin probe measurements, the design of the experiments, and participated in writing the manuscript. The supporting information for this chapter can be found in Appendix B.

Kelvin probe measurements on ferromagnetic thin film electrodes coated with self-assembled monolayers of chiral molecules reveal that the electron penetration from the metal electrode into the chiral molecules depends on the ferromagnet's magnetization direction and the molecules' chirality. Electrostatic potential differences as large as 100 mV are observed. These changes arise from the applied oscillating electric field which drives spin dependent charge penetration from the ferromagnetic substrate to the chiral molecules. The enantiospecificity of the response is studied as a function of the magnetization strength, the magnetization direction, and the handedness and length of the chiral molecules. These new phenomena are rationalized in terms of the chiral-induced spin selectivity (CISS) effect in which one spin orientation of electrons from the ferromagnet penetrates more easily into a chiral molecule than does the other orientation. The large potential changes (> kT at room temperature) manifested here imply that this phenomenon is important for spin transport in chiral spintronic devices and for magneto-electrochemistry of chiral molecules.

3.1 INTRODUCTION

The control and detection of electron spin dynamics is essential for the realization of spintronic[1] and quantum information technologies. Recent developments in molecular spintronics have pointed to the "spinterface" (ferromagnet surface/ molecular semiconductor interface) as playing an important role in determining device behavior.[2] This work demonstrates the use of chiral molecules to control the electron spin density at an interface and its effect on the electrostatic potential. Thus, it suggests that chiral molecules and the constraints they impose on the interface through the chiral induced spin selectivity (CISS) effect provide a new approach to controlling the "spinterface". This work also provides new insight into the mechanism of the chiral induced spin selectivity (CISS) effect discovered more than a decade ago[3] and for which a full quantitative theory has not yet been provided.

A number of different experiments have shown that chiral organic molecules exhibit strongly spin-dependent electron transport at room temperature. For example, one experimental method has examined the spin distribution of photoelectrons that transit from a metal substrate through a layer of chiral molecules and are detected with a Mott polarimeter.[4-6] In another method the effect was established by measuring the spin polarization of electron tunneling currents through individual chiral molecules adsorbed on a magnetized substrate.[7-9] The effect was also observed via the magnetization generated by chiral films[10, 11] and by the dissymmetry in electron transfer rates of chiral molecules[12, 13] and chiral quantum dots,[14-17] among others.[18-26] In addition, CISS has been shown by the enantiospecific adsorption rate of chiral molecules on magnetized ferromagnetic films.[27, 28] Abendroth et al[29] used photoemission spectroscopy to reveal workfunction shifts of ferromagnet/chiral molecule interfaces that depend on the magnetization direction. The current work explores the interfacial effects of chiral molecules assembled on a ferromagnetic substrate.

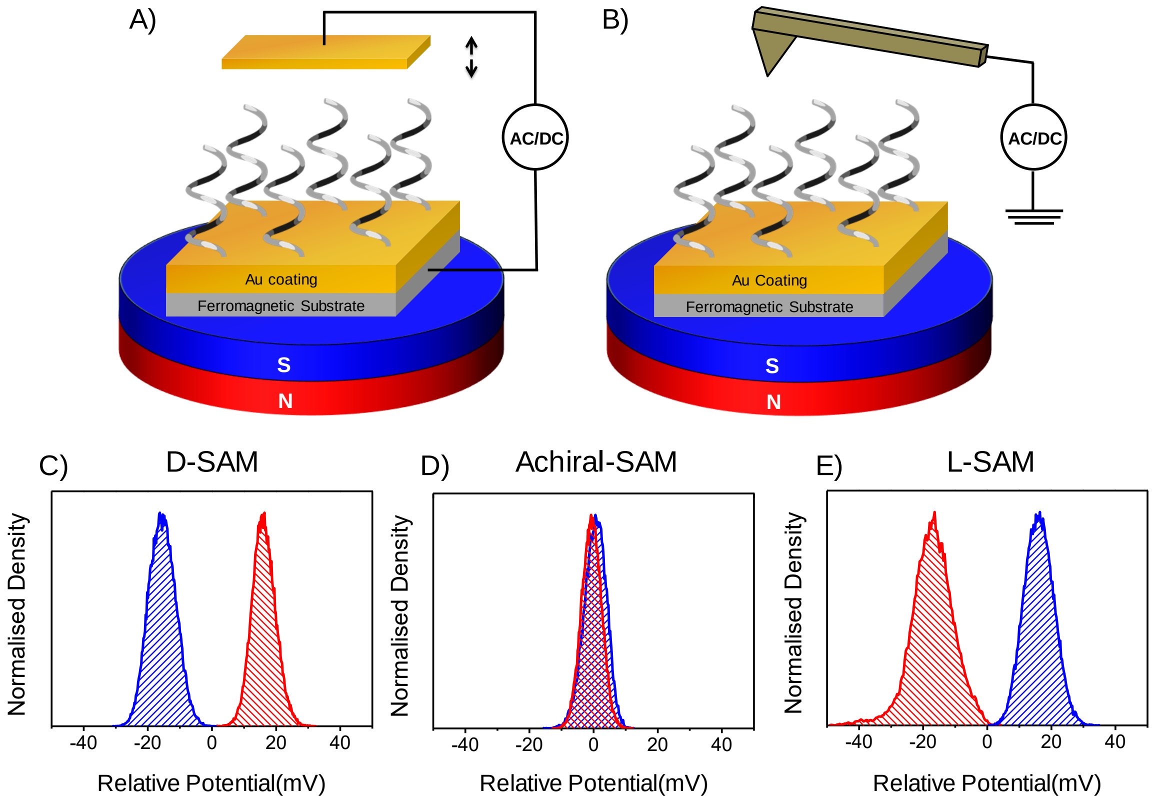

Figure 3.1 Schematic diagrams illustrating the principle of the Kelvin probe measurement. In the macroscopic measurement (panel A), the distance of an Au electrode from the chiral-SAM / ferromagnetic sample is varied sinusoidally. In the microscopy version of the Kelvin probe measurement (panel B), an AFM conducting tip is used as the counter-electrode and its lateral position is scanned to image the substrate's potential distribution. The diagrams illustrate how a static magnet is placed under the sample in order to saturate the magnetization of the ferromagnetic layer. Measured CPD distributions are shown for the D-AL5 peptide (panel C), L-AL5 peptide (panel E), and an achiral SAM (Panel D) coated ferromagnetic substrate under two different magnetizations. The blue color represents the potential distribution for a magnetization pointing to the South, and red corresponds to a North direction. These two directions are defined to be along the axis perpendicular to the surface. The zero voltage is set by the averaged contact potential difference found in the two measurements.

This study uses Kelvin probe force microscopy (KPFM)[30] and macroscopic Kelvin probe[31] measurements to investigate the spin-dependent resistance at metal-chiral molecule interfaces. Self-assembled monolayers (SAMs) of chiral organic molecules were adsorbed on ferromagnetic substrates, which were magnetized either parallel or antiparallel to the surface normal. Using the Kelvin probe, we investigated the effect of an oscillating electric field on charge injection from the magnetic substrate into the molecule as a function of the magnetization direction and the handedness of the molecule. An important advantage of this method over the existing ones, such as magneto-optic Kerr effect (MOKE) and tunneling microscopy methods, lies in its simplicity. The basic Kelvin-probe setup consists of a metallic probe electrode that is placed near the sample surface to form a capacitor (see Figure 3.1A). Then, the distance between the probe electrode and the sample surface is changed periodically to generate a frequency-dependent capacitance. Thus, an AC voltage is created across the gap and it is proportional to the voltage difference between the probe electrode and the sample. Rather than record the AC voltage directly, it is common to apply a DC voltage, referred to as the contact potential difference (CPD), to null the response. The concept of Kelvin probe force microscopy is similar except the probe in this case is a conductive cantilever which is scanned over the surface to record an electrostatic potential map (see Figure 3.1B). This work focuses on changes in the CPD, or electrostatic surface potential, that arise as one changes the adsorbate's enantiomeric form and the surface magnetization. These enantiospecific changes in the measured CPD arise from the spin dependence of charge penetration from the ferromagnet into the adsorbed chiral molecules, at the chiral molecule/ferromagnet interface.

Several ferromagnetic substrates (with Ni or Co layer) and different types of chiral SAMs were measured. For chiral SAMs, the CPD depends on the molecules' handedness and the ferromagnetic substrate's magnetization direction. This dependence arises from the difference between the probabilities of electrons with spin up and spin down tunneling into the chiral molecule layer, i.e., of the CISS effect. More specifically, the use of the ferromagnetic substrate affects the spin-dependent part of the contact resistance. For opposite magnetization directions of the ferromagnetic substrate, the change in the CPD corresponds to a difference in the induced dipole moments in the chiral SAM; it implies a strong penetration of the spin wavefunction through the molecular layer for one chirality, and a weaker penetration for the opposite chirality.

3.2 RESULTS

Panels C, D, and E of Figure 3.1 show histograms of the CPD, which were measured using the KPFM method (see Appendix B for more details), as a function of the magnetization direction for three self-assembled monolayer (SAM) systems: a D-AL5 peptide ($-S-CH_2-CH_2-(Ala-Aib)_5-COOH$) denoted as D-SAM, an L-AL5 peptide ($-S-CH_2-CH_2-(Ala-Aib)_5-COOH$) denoted as L-SAM, and an achiral-SAM composed of mercaptoalkylcarboxylates ($-S-(CH_2)_{15}-COOH$). The ferromagnetic substrates consist of a 10 nm thick layer of Ni with a 10 nm capping layer of Au. For the D-SAM, the CPD was found to be 30-40 mV higher under North (red) magnetization than under South (blue) magnetization (the two directions are along the axis perpendicular to the surface), whereas the opposite was found for the L-SAM. In a control experiment with achiral SAMs, the CPD does not show any dependence on the applied magnetization direction. These data show that for a magnetization direction which ‘matches’ the SAM chirality, the charge density extends farther into the chiral SAM.

To confirm that the observations originate from the preferential tunneling of one electron spin over the other (i.e. the CISS effect), the dependence of the CPD on the Au layer thickness (wedge shape layer) which covers the ferromagnetic cobalt thin film exhibiting a perpendicular anisotropy (see Figure 3.2) was measured. As the thickness of the Au layer increases, the spin-polarized electron density emanating from the ferromagnetic layer will depolarize more prior to entering the chiral molecules.[13] Thus, as the Au capping layer becomes thinner, the measured dependence of the potential difference on the magnetization direction should become stronger. Figure 3.2 shows KPFM results from measurements with L-AL5 SAMs adsorbed on a magnetic substrate comprising a 1.8 nm thick Co film that is covered with an Au wedge layer whose thickness is varied uniformly from 2 nm to 10 nm over a lateral distance of 10 mm (represented by the wedge shape at the top of Figure 3.2). The CPD was measured along the thickness gradient of the Au layer for two different film magnetization vertical orientations, North and South.

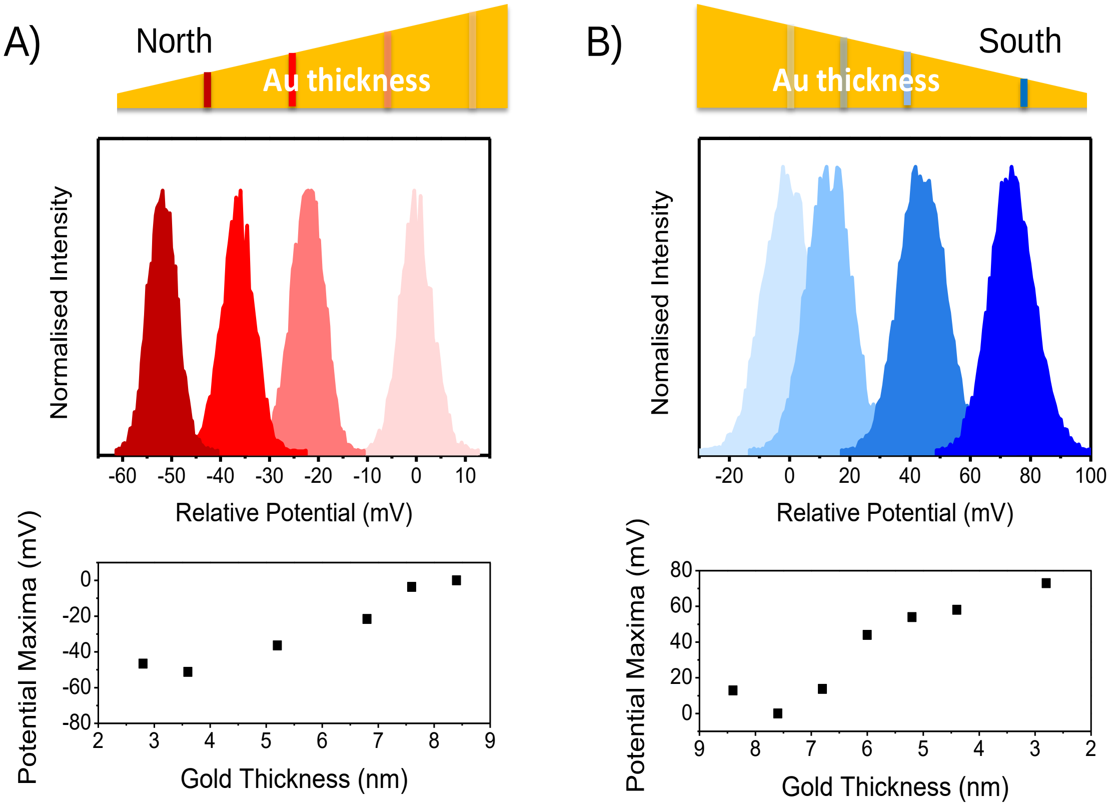

Figure 3.2 Change in the CPD as a function of the Au layer thickness for the opposite Co magnetization directions with adsorbed L-AL5 SAMs. The top diagram shows the distribution of a potential in different regions of the magnetic sample along the Au wedge. The color of each plot corresponds to the region indicated on the gradient bar by the same shade. The zero voltage is set by the measurement at the region of the highest Au thickness of 10 nm. The maxima of the potential distribution curves versus the thickness of the gold layer are plotted at the bottom of the Figure. As shown in panel (A) the CPD becomes more negative as the gold thickness decreases for a magnetization pointing up. In contrast, in panel (B) where the magnetization vector points down, the CPD becomes positive and its value increases with decreasing gold layer thickness. To estimate the error in the measurements see the FWHM of the histograms.

Under application of a North magnetic field (Figure 3.2A), the CPD becomes more negative as the gold thicknesses decreases from 10 nm to 2 nm (light to dark red). The lower panel shows a plot of the most probable CPD value (peak of the distribution) measured at different gold thicknesses. Conversely, for South magnetization direction (Figure 3.2B) the CPD becomes more positive as the gold thickness decreases (light to dark blue color). In both cases changing the Au capping thickness from 10 nm to 2 nm results in a 60-80 mV shift in the CPD. These data indicate that the spin polarization persists through more than 10 nm of Au, but that it is strongly attenuated.

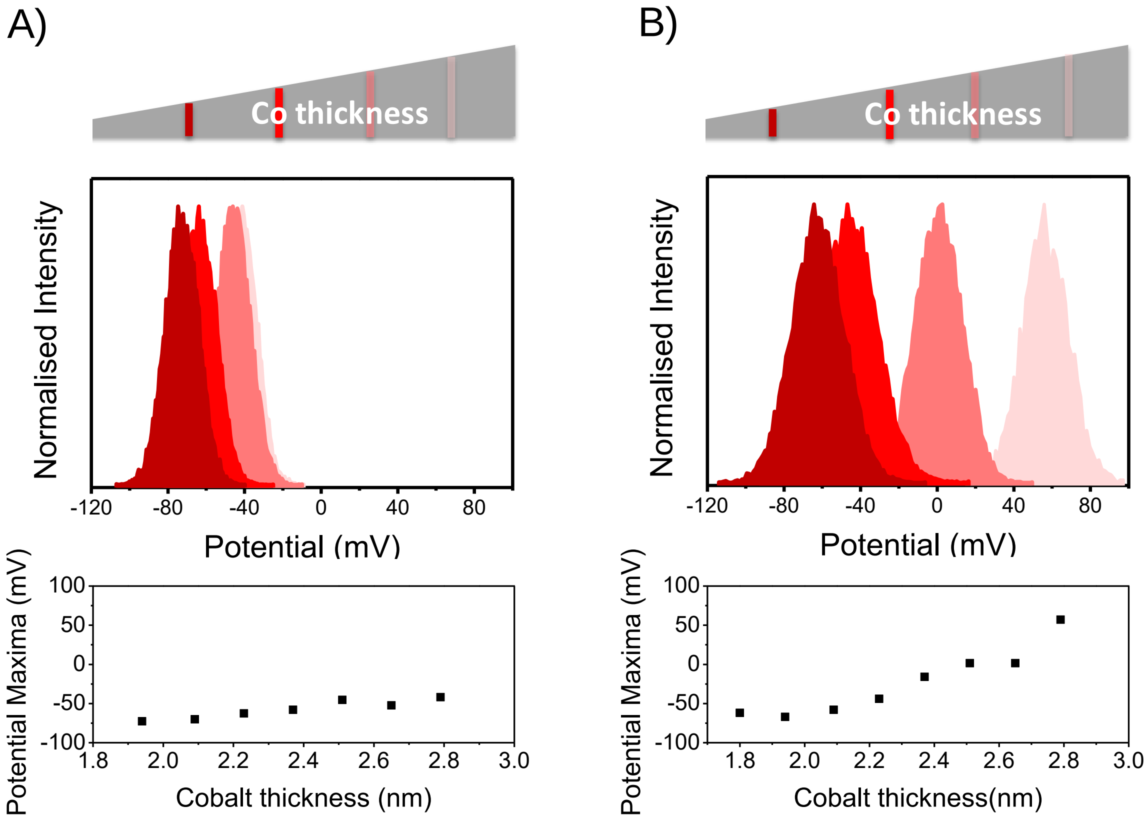

Figure 3.3 Coercivity dependent changes in the CPD. The Co thickness is changed from 1.5 to 3 nm and the coercive field decreases as the Co layer thickness increases. The color of each plot corresponds to the region indicated on the gradient bar by the same shade. The bottom diagram plots the maxima of the potential distribution curve for the substrate with adsorbed L-AL5 SAMs vs the thickness of the Co layer. The CPD measured in the presence of a constant magnetic field well above the coercive field (panel A) shows a weak dependence on the Co thickness. In contrast, a strong Co layer thickness dependence is measured in the absence of constant magnetic field (panel B). Here, the external magnetic field has been applied to orient a magnetization in a given direction and then removed prior to the measurement.

More importantly, these findings support the claim that spin delocalization from the chiral molecule into the magnetized substrate is responsible for the observed changes in CPD. Note that the MBE grown ferromagnetic Co layer in this sample, has a higher saturation magnetization than the polycrystalline Ni layer used for the measurements in Figure 3.1 and that in Au/Co/Au configuration such nanostructures feature a perpendicular anisotropy;[32] i.e. the easy axis points directly out-of-plane. This feature results in a larger difference in the CPD for the Co ferromagnetic substrates than for the Ni ferromagnetic substrates.

Previous work on the interaction of chiral molecules with ferromagnetic thin film surfaces showed that the enantiospecificity arose from the projection of the magnetic moment on the direction perpendicular to the film surface.[33] To examine this feature, measurements on the L-AL5 SAMs were conducted using Au/Co/Au ferromagnetic substrates, in which the cobalt-layer thickness was varied from 1.6 to 3 nm and the Au capping layer thickness was fixed at 2 nm. The coercivity and easy-axis direction of the magnetic layer (Co) changes with thickness; below 2 nm the easy axis of the Co is mainly out of plane while for Co layer thicknesses above 2 nm a spin reorientation transition takes place and the magnetization easy axis rotates to an in-plane direction (See Appendix B for more details on the ferromagnetic sample coercivity)[32, 34]

Figure 3.3A shows the CPD measured along the Co thickness gradient under North magnetization for substrates with the L-AL5 SAM. Note, the magnet was placed underneath the substrate during the measurements, i.e. the Co layer magnetization was oriented perpendicular to the sample normal, even for Co thicknesses above the spin reorientation transition, along the applied magnetic field direction. In this configuration, a large negative shift of CPD was observed, however the CPD distributions vary only weakly with the Co thickness. Figure 3.3B shows experimental results for the same sample as in Figure 3.3A, but upon removal of the permanent magnet. When the magnetic field is removed, the magnetization of the Co layer (for thicknesses of Co layer above 2 nm) is no longer oriented normal to the surface and instead rotates toward the ‘easy’ axis as a function of thickness. When the easy axis is not aligned with the electron injection direction into the SAM the electron density injected into the SAM is lower and the CPD becomes more positive. These results imply that the tilt angle of chiral molecules adsorbed on the substrate surface, in an ordered chiral monolayer, could be probed by changing the magnetization direction.

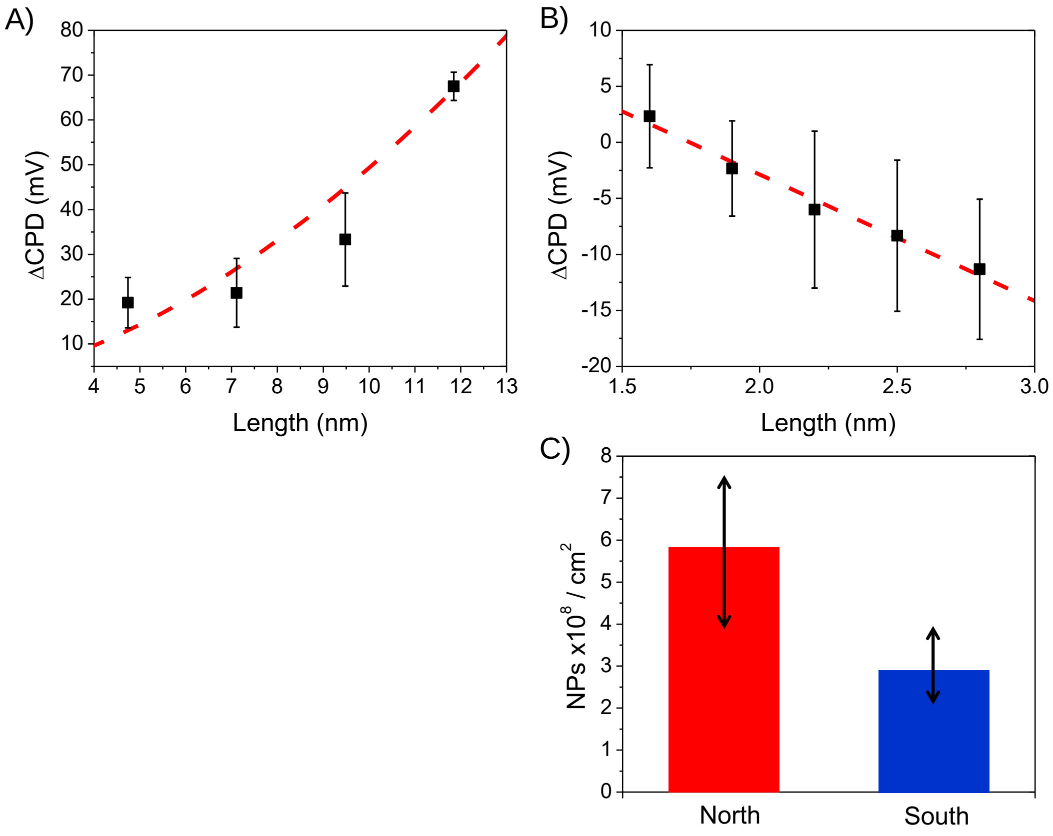

Figure 3.4 Panels A and B show a change in CPD for molecules of different length; (A) double stranded DNA and (B) AL_n oligopeptides on a magnetized Ni/Au electrode. The red lines are fits of the data by a quadratic dependence in panel (A) and by a linear fit in panel (B). See SI for details on the SAM compositions. Panel C shows the number of Au NPs that electrostatically bind to an L-polyalanine monolayer in 2 seconds, for North (red) and South (blue) magnetization directions. The experiments were repeated 5 times and measured at several different areas to reduce fluctuations.

Lastly, the dependence of the CPD's asymmetry on the substrate magnetization, was studied as a function of the chiral molecule length (L); see Figure 3.4. The CPD of the SAM coated substrate electrode arises from the potential drop across the SAM and thus should be proportional to the dipole moment of the molecules, $D \propto LQ$, in the SAM; where Q is the amount of charge transferred between the metal surface and the monolayer and L is the effective distance between this charge and the surface. As the molecules become longer, the injected charge can delocalize farther from the metal substrate and a larger potential drop is expected. If the delocalization length changes with the chiral molecule length, then the asymmetry in the contact potential difference, $\Delta\mathrm{CPD} = CPD(\mathrm{North}) - CPD(\mathrm{South})$, should change with length. Figure 3.4A shows the ΔCPD for North and South magnetized films with chiral DNA, and Figure 3.4B shows the case for oligopeptides (ALn with n=3-7) SAMs. See the Appendix B for molecular sequences of the DNA and oligopeptides. Interestingly, a different length dependence was observed for the two types of molecules: $\Delta\mathrm{CPD} \propto L^2$ for the DNA and $\Delta\mathrm{CPD} \propto L$ for the oligopeptides.

Given that the ΔCPD of the SAM-coated electrodes is proportional to the dipole moment of the molecules $D \propto LQ$, a linear dependence on L implies that the amount of charge displacement in the SAM layer is independent of molecular length; whereas, a supralinear dependence on L implies that the amount of charge displacement in the SAM increases with the molecular length. In DNA, the molecule's polarizability has been shown to scale linearly with the molecule's length,[35] and this could account for the quadratic growth in the dipole moment with the length, $D \propto L^2$. The data suggest that the polarizability in the oligopeptides does not change significantly over the short lengths studied (1.5 to 3 nm) and therefore the dipole moment appears to change linearly with the molecular length. While the ΔCPD signal has a different sign for DNA and oligopeptides, these data are consistent with previous reports; conductive AFM measurements showed a higher tunneling barrier for DNA under North magnetization[7] than South magnetization and the opposite for oligopeptides.[8]

Large changes in the surface potential can affect surface chemical processes. Figure 3.4C illustrates this fact by demonstrating how the change in surface charge of an L-polyalanine SAM on a magnetized Ni/Au substrate can be used to control the electrostatic adsorption of achiral gold NPs. The substrate was immersed for 2 seconds and the number of particles was normalized to a 1 cm2 substrate area. The gold NPs were counted using SEM images. The experiment was repeated five times. By simply changing the magnetization direction applied to the substrate, a two-fold change in the absorption rate was found.

3.3 A MODEL

Here we sketch a model that rationalizes the observations and is consistent with the many other CISS effect observations for electron transmission through chiral molecules. First we describe the time-dependence of the response, which results from the oscillating electric polarization in the molecule, and second we discuss the large magnitude of the effect. In the Kelvin probe experiment, a time-dependent response of the chiral SAM/ferromagnet sample is measured. Namely, charge flows between the ferromagnetic substrate and the SAM in response to the oscillating electric field that is applied by the Kelvin probe. As is known, the Kelvin probe measurement can be modeled by an AC electrical circuit comprising a capacitance for the probe and the interface. The situation studied here (metal with an insulating monolayer film) requires an effective capacitance comprising the capacitance of the SAM/Kelvin probe junction, $\mathrm{C_{mol-p}}$, in series with a resistance and capacitance for the ferromagnet/chiral-SAM interface, R and $\mathrm{C_{fm-mol}}$.

The resistance R determines the rate at which charge is transferred between the chiral molecules and the substrate.

While the effect of molecular films on a metal substrate's work function has been studied widely, much less is known about the difference in the behavior that arises for chiral molecules on ferromagnetic surfaces. An electric field that is acting on a molecule or molecular monolayer at an electrode, modifies the molecular electronic states. The electric fields at an electrode surface can be as high as 10^8 -10^9 V/m,[36] and this field induces a dipole moment in the molecule, i.e., an electron charge displacement. For chiral molecules, this charge displacement in the molecule is accompanied by a spin polarization.[37] Based on spin-orbit coupling strengths of about 5 meV in chiral organic molecules, one expects a spin polarization, ΔP, of a few percent, or less.[38, 39]

Upon application of an oscillating electric field onto the magnetic substrate coated with the chiral monolayer, charge reorganization in the molecule takes place, but also charge flow between the substrate and the molecules occurs. This charge flow implies charge exchange (electron cloud overlap) between the molecule and the metal. Electron density permeating from the metal into the positive electric pole of the molecule, polarized by the oscillating field, can have either the same spin as that of the electrons which remain at the positive pole or it can have the opposite spin. To estimate the difference in energy ΔE between the two possibilities, we take the product of the spin polarization ΔP, which is a metric for the difference in the two spin densities, and the typical value of the singlet-triplet energy splitting, which is a metric for the electronic orbital energy difference between the two spin types. In a Heitler-London valence bond picture,[40] this approximation results in

$$\Delta E = \frac{2(Q\,S^2 - J_{exc})}{1 - S^4} \cdot \Delta P \qquad \textbf{Equation 3.1}$$

where Q is the Coulomb integral, S is the electron overlap integral, and J_{exc} is the exchange integral. The values found for these different parameters are sensitive to the level of theory used for calculation. Thus, we approximate this term in the equation by the triplet-singlet energy difference of an excited electronic configuration. Given that the typical energy splitting between singlet and triplet states in hydrocarbons is of the order of 1 eV,[41] a spin polarization of 3% yields an energy splitting $\Delta E = 30$ meV. This energy splitting at 300K amounts to a spin selectivity in the spin injection of about 1:4, namely a spin polarization of approximately 60%. Clearly if the singlet-triplet energy difference is larger, or the initial spin polarization on the formation of the dipole is higher, then a higher spin polarization can be observed in the CISS effect. Consequently, a significant energy bias exists for injecting one spin orientation over the other and the magnitudes are sufficient to account for the observed contact potential differences. This mechanism is reminiscent of a “spin blockade”[42] that restricts the spin injection from the substrate to the molecule despite an apparent small spin-orbit coupling in the chiral molecule. Thus, this mechanism could give rise to the large spin selectivity reported in CISS processes and account for the large CPD values reported here.

The mechanism presented here indicates that the transport is nonlinear,[43] and it is consistent with the current versus voltage (I-V) curves that are observed in magnetic conducting probe measurements of oligopeptides. For convenience I-V curves for the AL7 molecule, which are taken from ref 8, are reproduced in Figure 3.5A under different magnetization directions. The data show that non-linear conduction occurs after an electric field is applied to the molecules. The current under South (blue) magnetization direction begins to occur when the applied voltage is approximately 93 mV, and the current for North (red) direction appears at a higher voltage, ~200 mV. The inset in Figure 3.5A shows a plot of log(I) versus voltage for the same data, which illustrates more clearly the difference in the voltage (difference in on-state and off-state voltage slopes) for the two curves. According to the suggested model vide supra, the difference of 100 mV between the voltage of the two spin currents is associated with a “spin blockade”[42]. Note, in this experiment the tip is ferromagnetic, as opposed to the experiments in Figures 3.1 –3.4 where the tip was conductive, hence the geometry of the experiment is inverted and the effect on the magnetization is reversed; panel B illustrates this difference. The sub-band splittings of the AFM tip, blue and red semicircles, are controlled by the applied magnetization, whereas the spin injection from the substrate into the chiral molecule, blue and red semicircles, is determined by the helicity of the molecule.

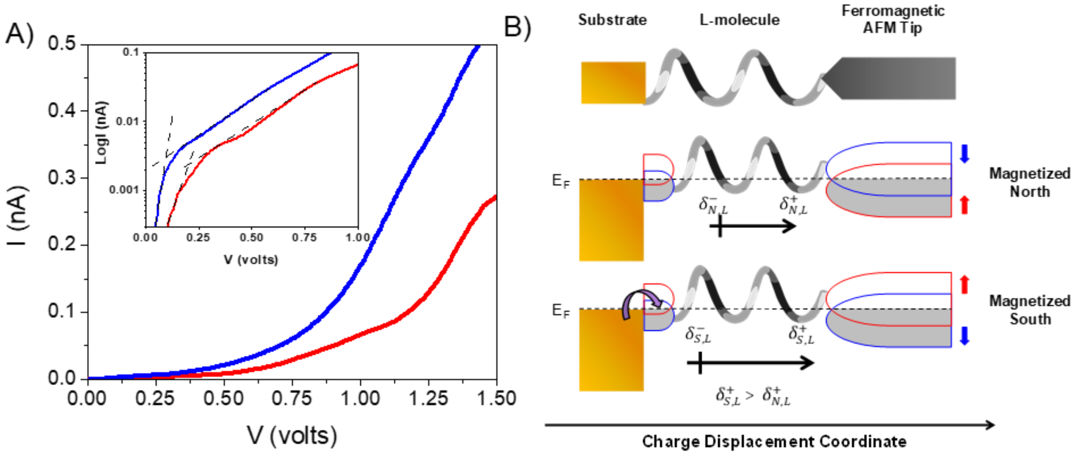

Figure 3.5 Paneles A shows I-V curves from magnetic conductive probe atomic force microscopy measurements in the presence of a magnetic field pointing South (blue) and magnet pointing North (red) for an AL7 oligopeptide. The inset is a log plot in which the dashed lines illustrate the changeover from off-state to on-state voltages. Panel B shows a corresponding cartoon depicting the interaction of the ferromagnetic substrate with the chiral SAM to create a “spin blockade”. The red and blue semicircles indicate a splitting of the spin sub bands.

Based on the presented model, the difference in the resistance of the chiral molecules can be rationalized by the spin dependence of the electron penetration into the molecular layer. Figure 3.3B provides further evidence corroborating the suggested model. Here, the contact potential difference of the same sample is measured, but in regions with two different thickness ranges. When Co is 1.8 nm thick the easy axis is pointing out-of-plane and the potential shift is much larger than that found for a 2.5 nm thick cobalt region in which the easy axis is in-plane. For the 1.8 nm thick Co both spin-orbit coupling and spin exchange interactions should be considered; whereas for the 2.5 nm thick Co, the spin-orbit coupling term may dominate.

3.4 SUMMARY

It was shown that coating a ferromagnetic film electrode with a self-assembled monolayer of chiral molecules leads to contact potential differences (measured via the Kelvin probe method) that depend on the magnetization direction of the ferromagnetic film with respect to the SAM’s chirality. The data show that the asymmetry in the potential difference can be as large as 100 mV and is controlled by the magnetization direction of the ferromagnetic film electrode. The use of Kelvin probe measurements for extracting spin dynamics inside chiral organic monolayer films demonstrates a new way to probe spin penetration in ultrathin films without the need for external contacts. The phenomena were interpreted using the CISS effect and AC transient charge redistribution, and the magnitude of the effect is explained by the non-linearity of the spin exchange interactions. These observations rationalize how large spin polarizations can be generated in the experiments despite the apparent small spin-orbit coupling in the chiral hydrocarbons and should thus motivate more detailed calculations on the interaction of chiral molecules with ferromagnetic substrates in the future.

3.5 REFERENCES

.

1.Varignon, J.; Vila, L.; Barthélémy, A.; Bibes, M., A new spin for oxide interfaces. *Nat. Phys.* **2018,** *14*, 322.

2.Cinchetti, M.; Dediu, V. A.; Hueso, L. E., Activating the molecular spinterface. *Nat. Mater.* **2017,** *16*, 507.

3.Naaman, R.; Paltiel, Y.; Waldeck, D. H., Chiral molecules and the electron's spin. *Nat. Rev. Chem.* **2019,** *3*, 250.

4.Göhler, B.; Hamelbeck, V.; Markus, T. Z.; Kettner, M.; Hanne, G. F.; Vager, Z.; Naaman, R.; Zacharias, H., Spin Selectivity in Electron Transmission Through Self-Assembled Monolayers of dsDNA. *Science* **2011,** *331*, 894.

5.Kettner, M.; Göhler, B.; Zacharias, H.; Mishra, D.; Kiran, V.; Naaman, R.; Fontanesi, C.; Waldeck, D. H.; Sęk, S.; Pawłowski, J., Spin Filtering in Electron Transport Through Chiral Oligopeptides. *J. Phys. Chem. C* **2015,** *119*, 14542.

6.Kettner, M.; Maslyuk, V. V.; Nürenberg, D.; Seibel, J.; Gutierrez, R.; Cuniberti, G.; Ernst, K. H.; Zacharias, H., Chirality-Dependent Electron Spin Filtering by Molecular Monolayers of Helicenes. *J. Phys. Chem. Lett.* **2018,** *9*, 2025.

7.Xie, Z.; Markus, T. Z.; Cohen, S. R.; Vager, Z.; Gutierrez, R.; Naaman, R., Spin specific electron conduction through DNA oligomers. *Nano Lett.* **2011,** *11*, 4652.

8.Kiran, V.; Cohen, S. R.; Naaman, R., Structure Dependent Spin Selectivity in Electron Transport through Oligopeptides. *J. Chem. Phys.* **2017,** *146*, 092302.

9.Aragonès, A. C.; Medina, E.; Ferrer-Huerta, M.; Gimeno, N.; Teixidó, M.; Palma, J. L.; Tao, N.; Ugalde, J. M.; Giralt, E.; Díez-Pérez, I., Measuring the Spin-Polarization Power of a Single Chiral Molecule. *Small* **2017,** *13*, 1602519.

10.Ben Dor, O.; Yochelis, S.; Radko, A.; Vankayala, K.; Capua, E.; Capua, A.; Yang, S. H.; Baczewski, L. T.; Parkin, S. S. P.; Naaman, R., Magnetization switching in ferromagnets by adsorbed chiral molecules without current or external magnetic field. *Nat. Commun.* **2017,** *8*, 14567.

11.Smolinsky, E. Z. B.; Neubauer, A.; Kumar, A.; Yochelis, S.; Capua, E.; Carmieli, R.; Paltiel, Y.; Naaman, R.; Michaeli, K., Electric field controlled magnetization in GaAs/AlGaAs heterostructures-chiral organic molecules hybrids. *J. Phys. Chem. Lett.* **2019,** *10*, 1139.

12.Mondal, P. C.; Fontanesi, C.; Waldeck, D. H.; Naaman, R., Spin-dependent Transport through Chiral Molecules Studied by Spin-dependent Electrochemistry. *Acc. Chem. Res.* **2016,** *49*, 2560.

13.Mondal, P. C.; Fontanesi, C.; Waldeck, D. H.; Naaman, R., Magnetic Field and Chirality Effects on Electrochemical Charge Transfer Rates: Spin Dependent Electrochemistry. *ACS Nano* **2015,** *9*, 3377.

14.Ben Dor, O.; Morali, N.; Yochelis, S.; Baczewski, L. T.; Paltiel, Y., Local Light-Induced Magnetization Using Nanodots and Chiral Molecules. *Nano Lett.* **2014,** *14*, 6042.

15.Bloom, B. P.; Kiran, V.; Varade, V.; Naaman, R.; Waldeck, D. H., Spin Selective Charge Transport through Cysteine Capped CdSe Quantum Dots. *Nano Lett.* **2016,** *16*, 4583.

16.Bloom, B. P.; Graff, B. M.; Ghosh, S.; Beratan, D. N.; Waldeck, D. H., Chirality Control of Electron Transfer in Quantum Dot Assemblies. *J. Am. Chem. Soc.* **2017,** *139*, 9038.

17.Bloom, B. P.; Liu, R.; Zhang, P.; Ghosh, S.; Naaman, R.; Beratan, D.; Waldeck, D. H., Directing Charge Transfer in Quantum Dot Assemblies. *Acc. Chem. Res.* **2018,** *51*, 2565.

18.Carmeli, I.; Skakalova, V.; Naaman, R.; Vager, Z., Magnetization of Chiral Monolayers of Polypeptide-A Possible Source of Magnetism in Some Biological Membranes. *Angew. Chem., Int. Ed.* **2002,** *41*, 761.

19.Zwang, T. J.; Hürlimann, S.; Hill, M. G.; Barton, J. K., Helix-Dependent Spin Filtering through the DNA Duplex. *J. Am. Chem. Soc.* **2016,** *138*, 15551.

20.Eckshtain-Levi, M.; Capua, E.; Refaely-Abramson, S.; Sarkar, S.; Gavrilov, Y.; Mathew, S. P.; Paltiel, Y.; Levy, Y.; Kronik, L.; Naaman, R., Cold denaturation induces inversion of dipole and spin transfer in chiral peptide monolayers. *Nat. Commun.* **2016,** *7*, 10744.

21.Suda, M.; Thathong, Y.; Promarak, V.; Kojima, H.; Nakamura, M.; Shiraogawa, T.; Ehara, M.; Yamamoto, H. M., Light-driven molecular switch for reconfigurable spin filters. *Nat. Commun.* **2019,** *10*, 2455.

22.Dor, O. B.; Yochelis, S.; Ohldag, H.; Paltiel, Y., Optical Chiral Induced Spin Selectivity XMCD Study. *Chimia* **2018,** *72*, 379.

23.Santos, J. I.; Rivilla, I.; Cossío, F. P.; Matxain, J. M.; Grzelczak, M.; Mazinani, S. K. S.; Ugalde, J. M.; Mujica, V., Chirality-Induced Electron Spin Polarization and Enantiospecific Response in Solid-State Cross-Polarization Nuclear Magnetic Resonance. *ACS Nano* **2018,** *12*, 11426.

24.He, X.; Zhou, Y.; Wen, X.; Shpilman, A. A.; Ren, Q., Effect of Spin Polarization on the Exclusion Zone of Water. *J. Phys. Chem. B* **2018,** *122*, 8493.

25.Abendroth, J. M.; Nakatsuka, N.; Ye, M.; Kim, D.; Fullerton, E. E.; Andrews, A. M.; Weiss, P. S., Analyzing Spin Selectivity in DNA-Mediated Charge Transfer via Fluorescence Microscopy. *ACS Nano* **2017,** *11*, 7516.

26.Ravi, S.; Sowmiya, P.; Karthikeyan, A., Magnetoresistance and Spin-filtering Efficiency of DNA-Sandwiched Ferromagnetic Nanostructures. *SPIN* **2013,** *03*, 1350003.

27.Banerjee-Ghosh, K.; Ben Dor, O.; Tassinari, F.; Capua, E.; Yochelis, S.; Capua, A.; Yang, S. H.; Parkin, S. S. P.; Sarkar, S.; Kronik, L., Separation of enantiomers by their enantiospecific interaction with achiral magnetic substrates. *Science* **2018,** *360*, 1331.

28.Tassinari, F.; Steidel, J.; Paltiel, S.; Fontanesi, C.; Lahav, M.; Paltiel, Y.; Naaman, R., Enantioseparation by crystallization using magnetic substrates. *Chem. Sci.* **2019,** *10*, 5246.

29.Abendroth, J. M.; Cheung, K. M.; Stemer, D. M.; El Hadri, M. S.; Zhao, C.; Fullerton, E. E.; Weiss, P. S., Spin-Dependent Ionization of Chiral Molecular Films. *J. Am. Chem. Soc.* **2019,** *141*, 3863.

30.Nonnenmacher, M.; O'Boyle, M. P.; Wickramasinghe, H. K., Kelvin probe force microscopy. *Appl. Phys. Lett.* **1991,** *58*, 2921.

31.Melitz, W.; Shen, J.; Kummel, A. C.; Lee, S., Kelvin probe force microscopy and its application. *Surf. Sci. Rep.* **2011,** *66*, 1.

32.Kisielewski, M.; Maziewski, A.; Tekielak, M.; Wawro, A.; Baczewski, L. T., New possibilities for tuning ultrathin cobalt film magnetic properties by a noble metal overlayer. *Phys. Rev. Lett.* **2002,** *89*, 087203.

33.Koplovitz, G.; Leitus, G.; Ghosh, S.; Bloom, B. P.; Yochelis, S.; Rotem, D.; Vischio, F.; Striccoli, M.; Fanizza, E.; Naaman, R., Single Domain 10 nm Ferromagnetism Imprinted on Superparamagnetic Nanoparticles Using Chiral Molecules. *Small* **2019,** *15*, 1804557.

34.Kisielewski, M.; Maziewski, A.; Kurant, Z.; Tekielak, M.; Wawro, A.; Baczewski, L. T., Magnetic ordering in ultrathin cobalt film covered by an overlayer of noble metals. *J. Appl. Phys.* **2003,** *93*, 7628.

35.Ying, L.; White, S. S.; Bruckbauer, A.; Meadows, L.; Korchev, Y. E.; Klenerman, D., Frequency and Voltage Dependence of the Dielectrophoretic Trapping of Short Lengths of DNA and dCTP in a Nanopipette. *Biophys. J.* **2004,** *86*, 1018.

36.Zangwill, A., *Physics at Surfaces*. 1988.

37.Kumar, A.; Capua, E.; Kesharwani, M. K.; Martin, J. M. L.; Sitbon, E.; Waldeck, D. H.; Naaman, R., Spin Polarization Accompanies Charge Polarization in Chiral Molecules- Implication for Enantio-selectivity and Bio-recognition. *Proc. Natl. Acad. Sci. U. S. A.* **2017,** *114*, 2474.

38.Yeganeh, S.; Ratner, M. A.; Medina, E.; Mujica, V., Chiral electron transport: Scattering through helical potentials. *J. Chem. Phys.* **2009,** *131*, 014707.

39.Michaeli, K.; Naaman, R., Origin of Spin Dependent Tunneling Through Chiral Molecules. *J. Phys. Chem. C* **2019,** *123*, 17043.

40.Shaik, S. S.; Phillipe, C. H., *A Chemist's Guide to Valence Bond Theory*. 2007.

41.Köhler, A.; Beljonne, D., The singlet-triplet exchange energy in conjugated polymers. *Adv. Funct. Mater.* **2004,** *14*, 11.

42.de Bruijckere, J.; Gehring, P.; Palacios-Corella, M.; Clemente-Leon, M.; Coronado, E.; Paaske, J.; Hedegard, P.; van der Zant, H. S. J., Ground-State Spin Blockade in a Single-Molecule Junction. *Phys. Rev. Lett.* **2019,** *122*, 197701.

43.Matityahu, S.; Utsumi, Y.; Aharony, A.; Entin-Wohlman, O.; Balseiro, C. A., Spin-dependent transport through a chiral molecule in the presence of spin-orbit interaction and nonunitary effects. *Phys. Rev. B: Condens. Matter Mater. Phys.* **2016,** *93*, 075407.

4.0 SPIN POLARIZATION STUDY OF PURE AND DOPED CHIRAL OXIDE THIN FILM FOR SPINTRONICS BASED DEVICES WITHOUT A PERMANENT FERROMAGNET

This work shows that the transmission of electrons through chiral cobalt oxide (CoOx) thin films is spin selective. The spin filtering is revealed through two complementary studies: magnetic conducting probe-atomic force microscopy (mcp-AFM) measurement of current-voltage curves and magnetoresistance measurements in a thin film device. The data show that the conduction of electrons depends on the chirality of the CoOx films. The mcp-AFM data and the magnetoresistance data display an antisymmetric response with the direction of the applied magnetic field, a signature that is indicative of the chiral induced spin selectivity (CISS) effect. In addition to the data on pure CoOx films, mcp-AFM studies of Mn doped oxide films are also reported and show that the Mn doping improves the spin polarization.

4.1 INTRODUCTION

Conventional electronics use electronic charge, whereas spintronics devices use the electron spin for data storage, data transfer, and other operations.[1] Spintronics devices are attractive as they require less energy to manipulate the spin than charging a capacitor. All the spintronics devices are based on the concept of transferring a spin-polarized electron to another ferromagnetic layer through a nonmagnetic layer. For example a spin valve based on the giant magnetoresistance (GMR) or tunneling magnetoresistance (TMR) effects consist of two ferromagnetic layers separated by a thin nonmagnetic layer; the first ferromagnetic layer is a fixed layer and the second layer acts as an analyzer which changes the magnetization direction with an external magnetic field.[2, 3] Although spin valve based devices are very attractive and are already being used in read heads and hard disks that are based on GMR or TMR effect, they suffer from drawbacks which limit their use for future application.[4, 5] The first one being the problem with miniaturization. The use of a permanent magnet limits the minimum sizes of material that can be used in the device since below that size the material becomes superparamagnetic. The second challenge is the need for the permanent ferromagnetic layer close to the free ferromagnetic layer. To solve the later problem other layers are being incorporated, which not only complicates the structure but also makes the devices more expensive. Additionally, it was found that the injection of spin current into the nonmagnetic layer often suffers from impedance mismatch between the metals and high-resistivity materials.[5-7]

The chiral induced spin selectivity effect (CISS effect), which describes chiral molecules as a spin filter, has been exploited to create devices in which spin current is injected without any need of permanent ferromagnetic layer. The CISS effect happens of the coupling between an electron's spin and its angular momentum in a chiral electrostatic potential. Because of this coupling, the transmission of one spin direction is preferred over the other in chiral molecules. A number of chiral biomolecules such as oligopeptides,[8] DNA,[9-12] bacteriorhodopsin(bR),[13] helicenes,[14] chiral conductive polymers[15] and other organic molecules[16] have been shown to display efficient spin filtering properties. Other inorganic-organic materials such as quantum dots,[17] perovskites,[18] metal organic frameworks or MOFs,[19] chiral metal organic crystals[20] have also shown great promise as a candidate for CISS based spintronics application. Although molecular based spintronics have shown some great promise, their implementation poses significant engineering challenges. For example, using chiral molecule assemblies in devices has not proved to be robust to high temperatures and other operating conditions. Moreover, the fabrication of reliable molecule metal junctions is not only a cumbersome process but also suffers from device shorting. A promising alternative would be to use pure chiral inorganic material as a source for spin polarized electrons.

Previously some pure inorganic material has shown to have efficient spin polarization. For example Inui et al. have studied spin transport through monoaxial chiral dichalcogenide $CrNb_3S_6$.[21] Their results show that a spin signal persists even over micrometer distances, which was attributed to spin-momentum locking due to the antisymmetric spin orbit interaction (SOI) under monoaxial chiral symmetry. Although the chiral crystal shows efficient spin transfer, the material consists of mixed chiral domains; as a result, different domains in the material will polarize different spin, which inhibits the materials use for making a spintronics device. Recently our group has shown another chiral metal oxide film, i.e chiral copper oxide which shows spin polarization at room temperature.[22] But the material shows only a very weak (5%) spin polarization which makes it difficult to make a device with a reasonable efficiency. So, to make spintronics devices with a nonmagnetic material as a spin source, it is necessary to use a material which can be prepared easily and also exhibit efficient spin polarization.

In this work spin dependent electron transport was studied through chiral cobalt oxide thin films that were prepared by the electrodeposition method. Two different experimental setups were used to study the spin polarization. In the first method, a magnetic conductive probe AFM technique was used, and electron conduction was measured with opposite magnetization. Results show higher conduction of one electron spin over the other with a chiral film. In the second method a spin-valve based magnetoresistance device was prepared and resistance of the device was measured for opposite spins. An antisymmetric magnetoresistance behavior was observed with the applied magnetic field. In both the cases the preferred spin was found to be opposite for L and D chiral film. Finally, the effect of doping on the spin polarization of the chiral cobalt oxide film was also studied and results show an improvement in the spin polarization upon doping the material with Mn ions.

4.2 RESULTS

4.2.1 Cobalt Oxide Thin Film and Chirality

Chiral cobalt oxide thin films were prepared by using a previously reported procedure.[23] Briefly electrodeposition is performed at a constant potential of 0.7 V vs Ag/AgCl in an aqueous solution of cobalt-tartrate complex at pH 9.6 (see experimental section for details). The thickness of the films are controlled by depositing for different amounts of time. Previous results showed that during the electrodepostion Co(II) in the solution oxidizes to generate Co(III)/Co(IV) species in the film. Figure 4.1a shows the surface topography of an L- cobalt oxide film.[24] As can be seen the surface has a roughness of ± 2 nm. To study the chirality, L and D cobalt oxide thin films were electrodeposited on an ultrathin metal electrode, comprising a quartz substrate that was coated with a 5nm Ti/10 nm Au gold overlayer, and the chirality was measured using circular dichroism spectroscopy. Figure 4.1b and 4.1c show the absorbance and circular dichroism spectra of the L/D chiral cobalt oxide films. In the absorbance spectra the feature at 325 -450 nm and at higher energy is associated with a Co-O ligand to metal charge transfer transition.[25] The opposite CD signal for the L and D cobalt oxides (figure 4.1c) indicates control over the chirality of the films by manipulation of the tartrate chirality. XRD (Figure C.1 in Appendix C) and XPS (Figure C.2 in Appendix C) characterization of the films were also performed, and they reveal no significant differences between the physical and morphological features of the films. Note that the cobalt oxide film which is prepared under these conditions is not magnetic.[23]

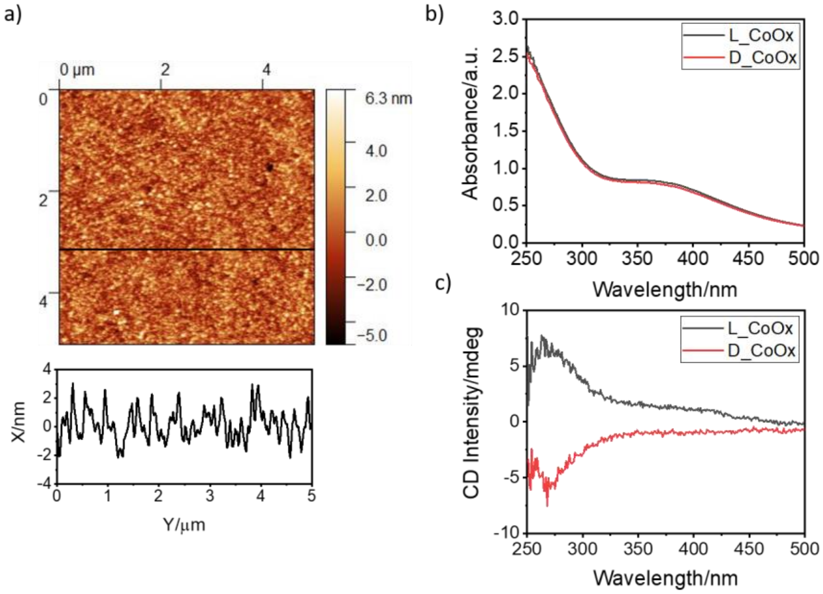

Figure 4.1 Panel a) shows a topography image of the L-CoOx surface. Panel b) shows the absorbance of L/D cobalt oxides that were prepared on a quartz/5 nm Ti/ 10 nm Au substrate. Panel c) shows circular dichroism of the corresponding films. The absorbance spectra are subtracted with the blank substrate of quartz 5nm Ti/ 10 nm Au. The cobalt oxides are 130-150 nm thick

4.2.2 Magnetic Conductive Atomic Force Microscopy

Spin dependent charge transport through the chiral cobalt oxide thin film was studied using magnetic conductive probe AFM (mcp-AFM) with a Co/Cr coated ferromagnetic tip. The sample for the mcp-AFM was prepared by electrodepositing a 25 nm thin film of CoOx on a 10 Ti/ 80 nm Au electrode. The ferromagnetic Co/Cr tip was magnetized by placing it on a permanent magnet, and the tip (magnetized either up or down) was then used to perform the conductance measurement; see Figure 4.2a. A potential bias is applied between the tip (held at ground) and the gold substrate, and the current flows between the gold substrate and the tip through the chiral metal oxide thin film. More than 40 current vs potential (*i*-V) curves were collected for each magnetization and an average of these curves are reported in Figure 4.2. The details about the experiments are given in section 4.4. Because conductive-AFM is very sensitive to different parameters such as the tip, contact resistance variation over the sample surface, the applied force, sample preparation etc., it is very important to do the measurements consistently between two opposite magnetizations. To avoid systematic biasing of the measurements, current-voltage curves were sampled on different regions of the surface with the same tip and the same force being used; the data in the figure are a statistical average of these different curves. During a typical experiment, an area of 20μm by 20 μm was first scanned to select flat and defect free regions for collecting the I-V measurements.

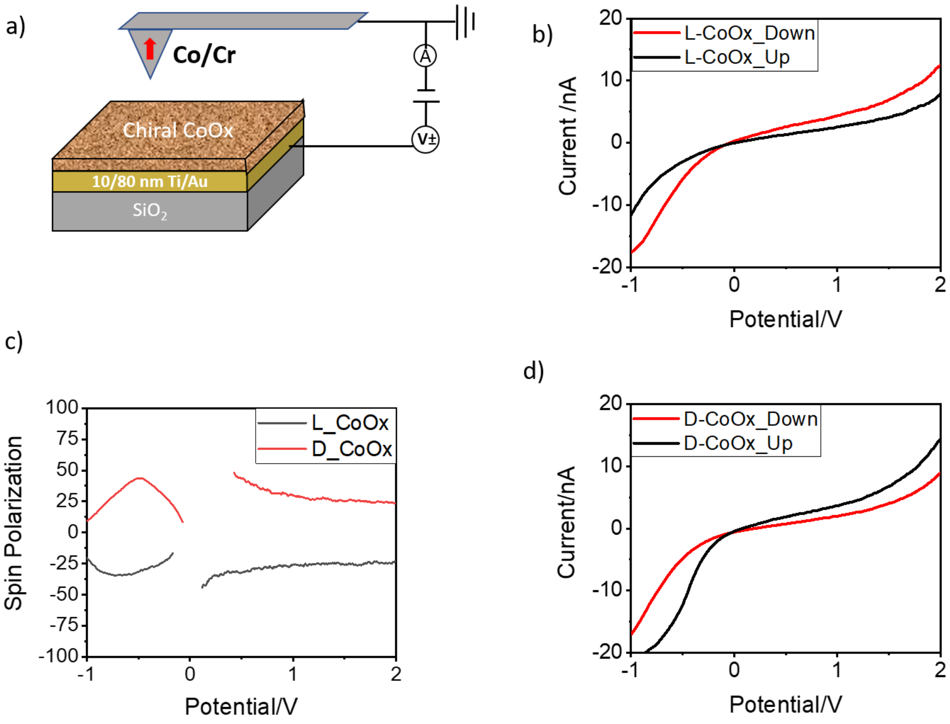

Figure 4.2 Panel a) shows a schematic diagram for the setup for the magnetic conductive AFM measurement. Panels b) and d) show the average *i*-V cruves for the L and D cobalt oxide respectively, with a north (red) or south (black)

magnetized tip. Panel c) plots the spin polarization of the current, as a percentage, versus the applied voltage for L-(black) or D-(red) cobalt oxide thin films.

Figure 4.2 summarizes the mcp-AFM data collected for the L and D chiral cobalt oxide films. Panel 4.2b) shows the current versus voltage (i-V) curves for L-CoOx and panel 4.2d) shows the *i*-V curves for the D-CoOx. Note that a nonlinear and asymmetric *i*-V behavior is obtained for the applied bias. The asymmetry of the individual i-V curves with voltage is attributed to the Schottky barriers in the AFM tip/CoOx/Au circuit element and is qualitatively consistent with that shown by others for metal-semiconductor-metal (M-S-M) structures.[26, 27] For L-CoOx, the current is consistently higher for the down magnetization than it is for the up magnetization. These data imply that under positive bias the spins polarized anti-parallel to the electron velocity (along the surface normal in the lab frame) transmit through the L-cobalt oxide more readily than the spins polarized parallel to the electron velocity (down in the lab frame). Under negative bias, the preferred spin orientation is also anti-parallel with the electron velocity, however the current direction has changed, and the preferred spins are oriented anti-parallel to the surface normal in the lab frame. This behavior manifests for spin filtering which occurs from the CISS effect.

From what is known about the CISS effect, the opposite chiral film should favor the opposite spin. Indeed, an opposite effect is observed with the D-cobalt oxide film where the up spin (spin parallel to electron velocity) shows a higher current than the spin down electrons (antiparallel to the electron velocity) under positive bias. The degree of spin polarization, P, can be calculated from the i-V data by using the equation.

$$P = \frac{i_{up} - i_{down}}{i_{up} + i_{down}} \times 100\% \qquad \textbf{Equation 4.1}$$

where i_{up} and i_{down} are the current measured with up or down magnetized tip respectively. From the figure 4.2c it can be seen that the spin polarization is close to 25-35 % between L and D cobalt oxide.

4.2.3 Spin Valve Based Magnetoresistance Device

Given the significant spin filtering (circa 25%) by the chiral CoOx film, a spin valve device that operates based on magnetoresistance was fabricated. A shematic diagram of the spin valve device is shown in Figure 4.3a. See section 4.4 for device specifications. In this device a crossbar geometry was employed. In the measurement, 1 mA of current flows from the bottom gold electrode through the CoOx film to the top electrode. During the experiment an external magnetic field is varied from 0 to 0.6 Tesla, then from 0.6 Tesla to -0.6 Tesla, and finally back to 0 Tesla. The data (pink dots in Figure 4.3b and Figure 4.3c) are collected at 0.05 Tesla intervals. The voltage difference was measured through the other two electrode contacts, and the resistance was computed using Ohm’s law. The magnetoresistance is defined as

$$MR(\%) = \frac{R(H) - R(0)}{R(H) + R(0)} \times 100$$ **Equation 4.2**

where R(0) is the resistance at zero magnetic field and R(H) is the resistance measured under the field. As can be seen from figure 4.3b), the magnetoresistance curve is antisymmetric with the field direction. Under a positive applied magnetic field, the nickel layer is magnetized along the surface normal and a larger resistance (by ~ 1 %) is observed for current flow through the L-CoOx layer than for the case of zero field. Under a negative applied magnetic field, the opposite behavior is observed; that is, the resistance to current flow by the chiral film is lower than it is under zero field (by ~ 1 %). This antisymmetric response is a common feature of spin current flowing through a chiral medium in contact with a ferromagnetic electrode.[28] It occurs because the spin filtering by the chiral film does not change with magnetic field direction but that of the Ni layer does; the Ni film can be considered as an analyzer polarizer for the spin current. Figure 4.3c shows the MR response for a D-CoO_x film and it has an anitsymmetric MR response that is opposite to that of the L-CoOx , as expected for spin filtering by the CISS effect.

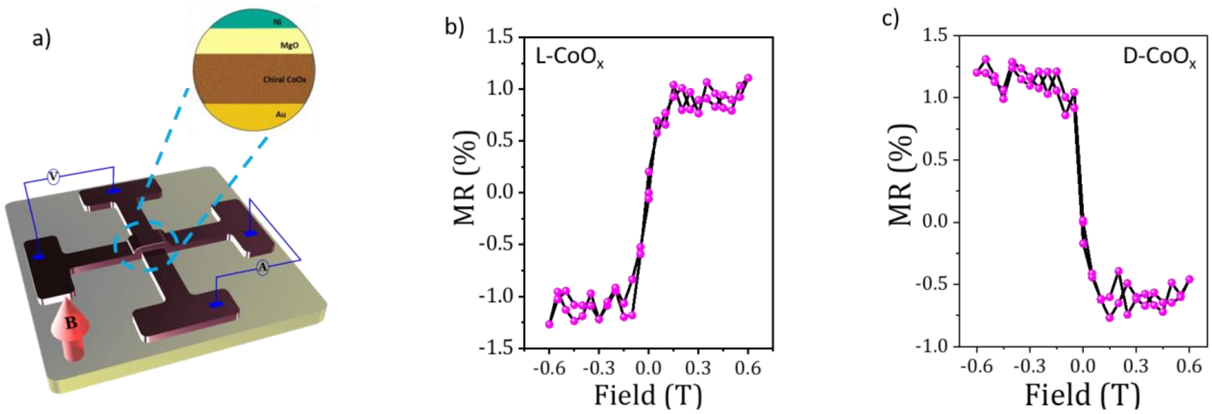

Figure 4.3 Panel a) shows a schematic illustration for the setup used in making the four probe magnetoregistance(MR) measurements; the bottom electrode is a gold film of 2μm thickness and the top electrode is ferromagnetic Ni. The inset shows different layers in the device. Panels b and c) show the magnetoregistance curves for L-CoOx and D-CoOx respectively.

The magnitude of the magnetoresistance difference is about 2%, between up an down. This experiment shows that non magnetic chiral thin films of CoOx can act as a spin filter in a device structure is about 2%, between up an down. Although the magnetoresistance difference in this system is low compare to other giant magnetoresistance device,[29] this experiment shows that non magnetic chiral thin films of CoOx can be used replacing the permanent ferromagnetic layer.

4.2.4 Spin Polarization with Mn Doped Cobalt Oxide Film

Thin film composition and order likely have a significant impact on spin filtering performance. For example, a recent study reported that chiral crystalline metal organic frameworks made of lanthanide show almost 100 % spin polarization, which is attributed to large spin-orbit coupling from paramagnetic Dy(III) species.[19] Figure 4.4 shows mcp-AFM data and spin polarizations for cobalt oxide doped with 5% Mn dopant. See the experimental section for details on the preparation of the doped L-CoOx films. To determine the stoichiometry between CoO_x and the Mn dopant, X-ray photoelectron spectroscopy was employed; Figure C.3 shows the measured Co2p and Mn2p spectra. To determine the atomic percent ratio the $2p_{3/2}$ peaks were integrated, and the resulting area was scaled to account for the differences in photoelectron cross section. Figure 4.4a compares the CD spectra of the doped and undoped L-CoOx films and it shows no significant differences between the two films.

The magnetic conducting probe AFM data for the Mn doped L-CoOx films were collected for both up and down magnetic fields, and the averaged current vs potential profiles are plotted in figure 4.4b. The current with down magnetization shows a higher current than do the data for the up magnetization. Note that the chirality of the pure and the doped L-CoOx films have the same sense (as defined by the circular dichroism spectra) and thus they are expected to select for the same spin polarizion of the electrons(figure 4.4a).[30] The spin polarization was computed for these doped films and it is plotted along with that computed for the undoped L-CoOx films in Figure 4.4c. Interestingly the polarization with the doped film shows a larger spin polarization (red curve) than the undoped chiral cobalt oxide(black). In fact, the spin polarization increases from 25 % to 55-60 % (at 1 V potential bias) upon doping.

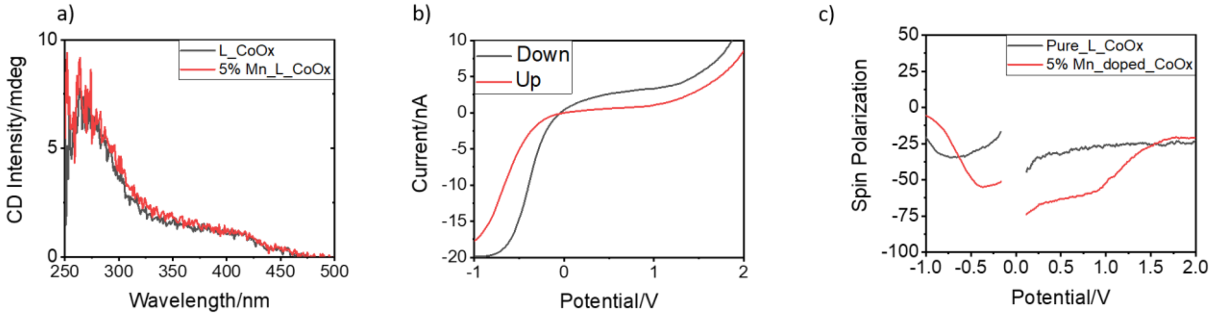

Figure 4.4 Panel a) shows circular dichroism spectra of pure and 5% Mn doped cobalt oxide films. Panel b) shows *i*-V curves for the 5% Mn doped CoOx for different magnetizations. Panel c) plots the spin polarization, as a percentage, versus applied voltage for pure (black) and 5% Mn doped cobalt oxide.

How can one explain the increase in the spin polarization? To answer this question we consider at the likely spin state of the Mn. Previous studies imply that Mn-doped cobalt oxide can occur by substitutional displacement of Co^{3+} ($t_{2g}^{6} – e_g^{0}$) by Mn^{3+} ($t_{2g}^{3} – e_g^{1}$) .[31] In this scenario, a low spin cobalt ion is replaced by a high spin Mn ion. Note that the high spin Co sites are reported to undergo Jahn-Teller distortion to a bipyramidal site geometry, however they remain high spin. We hypothesize that the paramagnetic Mn^{3+} ions in the chiral film are aligned with the chiral axis, because for the CISS effect, and enhance the spin polarization over the case of the CoOx. This hypothesis is consistent with an earlier MOF study[19] and a study on metallo-peptides[32].

4.3 CONCLUSION

The presents study demonstrates that transmission of electron through a chiral cobalt oxide thin film is spin dependent. A magnetic conductive AFM study shows a 25 % spin polarization through pure chiral cobalt oxide film. Spin polarization can be improved to 50-60 % by doping the material with 5% Mn. The paramagnetic nature of the Mn species with empty d orbitals ensures that spin transport is intact throughout the materials. Finally using the chiral cobalt oxide thin film we have prepared a spin valve based on magnetoresistance of the device. This study shows how a simple electrodeposition of chiral film can be used as a alternative to the magnetic layer for spin electron source in spintronics devices. This work demonstrates that chiral metal oxide films can displayspin filtering properties that may prove useful as a source of spin polarized electrons in spintronics device. This will not only simplify the spintronics device structure but also make this a economically viable process.

4.4 EXPERIMENTAL METHODS

4.4.1 Thin Chiral Cobalt Oxide Thin Film Deposition

Chiral cobalt oxide thin films wereprepared by using an electrodeposition method following a previous procedure.[23] Briefly L/D tartaric acid(0.8 mmol), $CoCl_2.6H_2O$ (0.08 mmol) were added to 10 ml of water to make a Co-tartrate complex. Next, sodium carbonate (2 mmol) was added to the solution and the total volume was increased to 20 ml. A three-electrode system was employed where the working electrode is made of glass and coated with 10 nm Ti and 80 nm Au which is deposited by e-beam evaporation. A Pt sheet and Ag/AgCl were used as counter and reference electrode, respectively. The electrodeposition was done 0.7 V constant potential for 300 sec to deposit a 25 nm thin film. For preparing the Mn doped cobalt oxide films, the deposition was performed under the same conditions except that $MnCl_2$ was also added in the electrolyte solution. The ratio of metal salts that is needed to prepare a 5% Mn-doped cobalt oxide was found to be 95:5 for $CoCl_2$: $MnCl_2$. Prior to the electrodeposition, the substrate was cleaned with boiling acetone and ethanol for 10 min each, and after the deposition the film was rinsed with water and dried before use.

4.4.2 Magnetic Conductive AFM

Magnetic conductive probe AFM (mcp-AFM) was performed using a chiral metal oxide coated/gold substrate. The substrate was prepared by depositing 10 nm Ti followed by a 80 nm Au layer on a glass substrate. Prior to the electrodeposition the substrate was cleaned with boiling acetone and ethanol for 10 min each. A 25-30 nm chiral L/D CoOx thin film was deposited on the one half of the substrate. After the deposition was complete the substrate was rinsed with water and left in the vacuum to dry before the conducting probe measurements. The mcp-AFM was performed using an Asylum instrument with a Cr/Co magnetic tip (ASYMFMHM-R2, Asylum Research) of coercivity 550 Oe. Before the conductance measurement the tip was magnetized with a permanent magnet for 10 min with either up or down magnetic field. For each magnetization, 40-50 *i*-V curves were measured at different positions. To avoid damage of the tip by lateral motion, the tip was retracted in between the measurements. Before the conductance measurement on the cobalt oxide film, experiments were performed on a bare gold surface to confirm the conductive signal from the gold surface**.** Note that the tip that was used for this experiment has higher coercivity and it retains its magnetization for many hours, > 5 hrs. The *i*-V curves were measured in a contact mode with a force of 25 nN that was applied between tip and the substrates during the experiment. Applying a lower force results in inconsistent signals. Measurements for opposite magnetization were done in the same location for a fair comparison.

4.4.3 Magnetoresistance Device

Magnetoresistance experiments were done in a crossbar geometry using a four probe method. The device was prepared on SiO_2 wafer, where the bottom electrode (2um) was made of 10 nm Ti layer followed by 40 nm gold (Au) layer, and was prepared by using optical lithography. On the top of that a thin film (20-25 nm) of chiral cobalt oxide was deposited using electrodeposition (described above). A buffer layer of thickness 1.5 nm of MgO was deposited on the top using e-beam evaporation. Finally, a 50 μm top electrode made of 40 nm Ni and 10 nm Au were deposited in a cross-bar geometry using a shadow mask. The gold layer on the top was used to protect the ferromagnetic (Ni) layer from oxidation. The conductance measurements were carried out within a SQUIDMPMS3 made by Quantum Design. A magnetic field between ± 0.6 Tesla is applied in out of the plane mode of the device and the resistance of the devices was measured using a standard 4 probe method by applying a constant 1 mA current to the opposite electrode. The magnetic field was varied cyclically from 0 to 0.6 T and then -0.6 T back to 0T. The 1 mA current was passed from the bottom gold electrode to the top ferromagnetic electrode and the potential was measured for each 0.05 T change in the magnetic field.

4.5 REFERENCES

1.Žutić, I.; Fabian, J.; Das Sarma, S., Spintronics: Fundamentals and applications. *Reviews of Modern Physics* **2004,** *76* (2), 323-410.

2.Tsymbal, E. Y.; Pettifor, D. G., Perspectives of giant magnetoresistance. In *Solid State Physics*, Ehrenreich, H.; Spaepen, F., Eds. Academic Press: 2001; Vol. 56, pp 113-237.

3.Lee, Y. M.; Hayakawa, J.; Ikeda, S.; Matsukura, F.; Ohno, H., Effect of electrode composition on the tunnel magnetoresistance of pseudo-spin-valve magnetic tunnel junction with a MgO tunnel barrier. *Applied Physics Letters* **2007,** *90* (21), 212507.

4.Dolui, K.; Narayan, A.; Rungger, I.; Sanvito, S., Efficient Spin Injection and Giant Magnetoresistance in Fe/MoS2/Fe Junctions. *Physical Review B* **2014,** *90* (4), 041401.

5.Schmidt, G.; Ferrand, D.; Molenkamp, L. W.; Filip, A. T.; van Wees, B. J., Fundamental obstacle for electrical spin injection from a ferromagnetic metal into a diffusive semiconductor. *Physical Review B* **2000,** *62* (8), R4790-R4793.

6.Rashba, E. I., Theory of electrical spin injection: Tunnel contacts as a solution of the conductivity mismatch problem. *Physical Review B* **2000,** *62* (24), R16267-R16270.

7.Mathew, S. P.; Mondal, P. C.; Moshe, H.; Mastai, Y.; Naaman, R., Non-magnetic organic/inorganic spin injector at room temperature. *Applied Physics Letters* **2014,** *105* (24), 242408.

8.Aragonès, A. C.; Medina, E.; Ferrer-Huerta, M.; Gimeno, N.; Teixidó, M.; Palma, J. L.; Tao, N.; Ugalde, J. M.; Giralt, E.; Díez-Pérez, I.; Mujica, V., Measuring the Spin-Polarization Power of a Single Chiral Molecule. *Small* **2017,** *13*, 1602519.

9.Abendroth, J. M.; Nakatsuka, N.; Ye, M.; Kim, D.; Fullerton, E. E.; Andrews, A. M.; Weiss, P. S., Analyzing Spin Selectivity in DNA-Mediated Charge Transfer via Fluorescence Microscopy. *ACS Nano* **2017,** *11*, 7516.

10.Göhler, B.; Hamelbeck, V.; Markus, T. Z.; Kettner, M.; Hanne, G. F.; Vager, Z.; Naaman, R.; Zacharias, H., Spin Selectivity in Electron Transmission Through Self-Assembled Monolayers of Double-Stranded DNA. *Science* **2011,** *331*, 894.

11.Xie, Z.; Markus, T. Z.; Cohen, S. R.; Vager, Z.; Gutierrez, R.; Naaman, R., Spin Specific Electron Conduction through DNA Oligomers. *Nano Lett.* **2011,** *11*, 4652.

12.Zwang, T. J.; Hürlimann, S.; Hill, M. G.; Barton, J. K., Helix-Dependent Spin Filtering through the DNA Duplex. *J. Am. Chem. Soc.* **2016,** *138*, 15551.

13.Varade, V.; Markus, T.; Vankayala, K.; Friedman, N.; Sheves, M.; Waldeck, D. H.; Naaman, R., Bacteriorhodopsin based non-magnetic spin filters for biomolecular spintronics. *Physical Chemistry Chemical Physics* **2018,** *20* (2), 1091-1097.

14.Kiran, V.; Mathew, S. P.; Cohen, S. R.; Hernández Delgado, I.; Lacour, J.; Naaman, R., Helicenes—A New Class of Organic Spin Filter. *Advanced Materials* **2016,** *28* (10), 1957-1962.

15.Mondal, P. C.; Kantor-Uriel, N.; Mathew, S. P.; Tassinari, F.; Fontanesi, C.; Naaman, R., Chiral Conductive Polymers as Spin Filters. *Advanced Materials* **2015,** *27* (11), 1924-1927.

16.Mishra, S.; Pirbadian, S.; Mondal, A. K.; El-Naggar, M. Y.; Naaman, R., Spin-Dependent Electron Transport through Bacterial Cell Surface Multiheme Electron Conduits. *Journal of the American Chemical Society* **2019,** *141* (49), 19198-19202.

17.Bloom, B. P.; Kiran, V.; Varade, V.; Naaman, R.; Waldeck, D. H., Spin Selective Charge Transport through Cysteine Capped CdSe Quantum Dots. *Nano Letters* **2016,** *16* (7), 4583-4589.

18.Lu, H.; Wang, J.; Xiao, C.; Pan, X.; Chen, X.; Brunecky, R.; Berry, J. J.; Zhu, K.; Beard, M. C.; Vardeny, Z. V., Spin-dependent charge transport through 2D chiral hybrid lead-iodide perovskites. *Science Advances* **2019,** *5* (12), eaay0571.

19.Huizi-Rayo, U.; Gutierrez, J.; Seco, J. M.; Mujica, V.; Diez-Perez, I.; Ugalde, J. M.; Tercjak, A.; Cepeda, J.; San Sebastian, E., An Ideal Spin Filter: Long-Range, High-Spin Selectivity in Chiral Helicoidal 3-Dimensional Metal Organic Frameworks. *Nano Letters* **2020,** *20* (12), 8476-8482.

20.Mondal, A. K.; Brown, N.; Mishra, S.; Makam, P.; Wing, D.; Gilead, S.; Wiesenfeld, Y.; Leitus, G.; Shimon, L. J. W.; Carmieli, R.; Ehre, D.; Kamieniarz, G.; Fransson, J.; Hod, O.; Kronik, L.; Gazit, E.; Naaman, R., Long-Range Spin-Selective Transport in Chiral Metal–Organic Crystals with Temperature-Activated Magnetization. *ACS Nano* **2020,** *14* (12), 16624-16633.

21.Inui, A.; Aoki, R.; Nishiue, Y.; Shiota, K.; Kousaka, Y.; Shishido, H.; Hirobe, D.; Suda, M.; Ohe, J.-i.; Kishine, J.-i.; Yamamoto, H. M.; Togawa, Y., Chirality-Induced Spin-Polarized State of a Chiral Crystal ${\mathrm{CrNb}}_{3}{\mathrm{S}}_{6}$. *Physical Review Letters* **2020,** *124* (16), 166602.

22.Ghosh, K. B.; Zhang, W.; Tassinari, F.; Mastai, Y.; Lidor-Shalev, O.; Naaman, R.; Möllers, P.; Nürenberg, D.; Zacharias, H.; Wei, J.; Wierzbinski, E.; Waldeck, D. H., Controlling Chemical Selectivity in Electrocatalysis with Chiral CuO-Coated Electrodes. *The Journal of Physical Chemistry C* **2019,** *123* (5), 3024-3031.

23.Ghosh, S.; Bloom, B. P.; Lu, Y.; Lamont, D.; Waldeck, D. H., Increasing the Efficiency of Water Splitting through Spin Polarization Using Cobalt Oxide Thin Film Catalysts. *The Journal of Physical Chemistry C* **2020,** *124* (41), 22610-22618.

24.Casella, I. G., Electrodeposition of cobalt oxide films from carbonate solutions containing Co(II)–tartrate complexes. *Journal of Electroanalytical Chemistry* **2002,** *520* (1), 119-125.

25.Barreca, D.; Massignan, C.; Daolio, S.; Fabrizio, M.; Piccirillo, C.; Armelao, L.; Tondello, E., Composition and Microstructure of Cobalt Oxide Thin Films Obtained from a Novel Cobalt(II) Precursor by Chemical Vapor Deposition. *Chemistry of Materials* **2001,** *13* (2), 588-593.

26.Wang, S.; Cheng, G.; Cheng, K.; Jiang, X.; Du, Z., The current image of single SnO2 nanobelt nanodevice studied by conductive atomic force microscopy. *Nanoscale Research Letters* **2011,** *6* (1), 541.

27.Giannazzo, F.; Schilirò, E.; Greco, G.; Roccaforte, F., Conductive Atomic Force Microscopy of Semiconducting Transition Metal Dichalcogenides and Heterostructures. *Nanomaterials* **2020,** *10* (4).

28.Michaeli, K.; Varade, V.; Naaman, R.; Waldeck, D. H., A new approach towards spintronics–spintronics with no magnets. *Journal of Physics: Condensed Matter* **2017,** *29* (10), 103002.

29.Bhatti, S.; Sbiaa, R.; Hirohata, A.; Ohno, H.; Fukami, S.; Piramanayagam, S. N., Spintronics based random access memory: a review. *Materials Today* **2017,** *20* (9), 530-548.

30.Bloom, B. P.; Graff, B. M.; Ghosh, S.; Beratan, D. N.; Waldeck, D. H., Chirality Control of Electron Transfer in Quantum Dot Assemblies. *Journal of the American Chemical Society* **2017,** *139* (26), 9038-9043.

31.Ke, Q.; Yi, D.; Jin, Y.; Lu, F.; Zhou, B.; Zhan, F.; Yang, Y.; Gao, D.; Yan, P.; Wan, C.; Cui, P.; Golberg, D.; Yao, J.; Wang, X., Manganese Doping in Cobalt Oxide Nanorods Promotes Catalytic Dehydrogenation. *ACS Sustainable Chemistry & Engineering* **2020,** *8* (14), 5734-5741.

32.Torres-Cavanillas, R.; Escorcia-Ariza, G.; Brotons-Alcázar, I.; Sanchis-Gual, R.; Mondal, P. C.; Rosaleny, L. E.; Giménez-Santamarina, S.; Sessolo, M.; Galbiati, M.; Tatay, S.; Gaita-Ariño, A.; Forment-Aliaga, A.; Cardona-Serra, S., Reinforced Room-Temperature Spin Filtering in Chiral Paramagnetic Metallopeptides. *Journal of the American Chemical Society* **2020,** *142* (41), 17572-17580.

5.0 INCREASING THE EFFICIENCY OF WATER SPLITTING THROUGH SPIN POLARIZATION USING COBALT OXIDE THIN FILM CATALYSTS

This chapter is taken from Ghosh, S.; Bloom, B. P.; Lu, Y.; Lamont, D.; Waldeck, D. H. *J. Phys. Chem. C* **2020**, 124(41), 22610-22618. The author of the dissertation performed the electrochemistry, the design of the experiments, the thin film deposition, and the water splitting measurements, as well as participated in writing the manuscript. The supporting information for this chapter can be found in Appendix D.

This work explores the use of chiral cobalt oxide thin film electrocatalysts for the oxygen evolution reaction and examines how their spin polarization properties might be used to control electrochemically generated intermediates at different pH values. These studies demonstrate that chiral cobalt oxide electrocatalysts reduce the reaction overpotential by 65 mV at 10 mA cm^{-2}, increase the oxygen yield by 1.4-fold at a fixed current density at pH 10, and decrease the production of hydrogen peroxide by 4.0-fold as compared to the corresponding meso-CoO_x analogs. Additional studies in which the electrocatalyst is modified to make it paramagnetic exhibit a similar enhancement with an applied external magnetic field. The findings from these studies are described using a proposed mechanistic model which unifies the favorable effects of chirality and magnetization. The results are attributed to the advantage of spin polarized intermediates in facilitating the oxygen evolution reaction.

5.1 INTRODUCTION

The emergence of a hydrogen economy is largely predicated upon the development of cost-effective and low carbon footprint methods for producing hydrogen. While gasification and steam reforming are established cost-effective routes to hydrogen generation, their carbon content is significant.[1] The electrolysis of water is one promising avenue for storing the electricity generated from renewable and carbon free technologies as hydrogen fuel.[2-4] Because of their excellent prolonged stability and potential for high turnover efficiency, metal oxide catalysts have been studied extensively for water splitting reactions.[5, 6] First row transition metal oxide and hydroxides are particularly interesting candidates for next-generation electrocatalysts because of their relatively cheap cost and ease in fabrication, however more improvement is required to compete with existing state-of-the-art electrolysis technologies.[7]

During the water splitting process, hydrogen is formed at the cathode, and oxygen is formed at the anode through a process involving the net transfer of four electrons. The anodic process, or oxygen evolution reaction (OER), has previously been identified as greatly affecting the overpotential for the water splitting reaction and can be the bottleneck for the entire process.[8] Because ground state oxygen exists in a triplet state, O_2 ($^3\sum_g^-$), we and others have hypothesized that its 'sluggishness' arises from spin constraints that exist in the elementary reaction steps for its formation.[9, 10] Often, spin constraints are not explicitly included in the design of water splitting architectures, so that O_2 ($^3\sum_g^-$) formation competes with singlet mediated processes such as, the formation of hydrogen peroxide and other superoxide species. At high pH, these undesired pathways are less favorable because of the stability of the products, however the spin restrictions in the formation of O_2 ($^3\sum_g^-$) can still limit the Faradaic efficiency of the reaction. At neutral pH, however, peroxide and superoxide species are more stable[11, 12] so that preventing their formation becomes increasingly important. The formation of hydrogen peroxide and superoxides can also decrease the stability of the anode[13] which degrades the catalyst's performance. Thus, a catalyst's ability to minimize side reactions while improving the efficiency of O_2 ($^3\Sigma_g^-$) formation is paramount for increasing the stability of the catalyst and the overall efficiency of the reaction.

Several groups have investigated the importance of spin considerations during O_2 ($^3\Sigma_g^-$) generation.[9, 14-19] For instance, de Groot *et al.* has shown theoretically that the good catalytic performance in OER for $RuO_2(110)$ may arise from the material's magnetic moment on the surface which helps to align adjacent spins.[14] Other groups have illustrated the importance of the number of unpaired electron's in the catalyst's active center[15, 16] which have since been shown theoretically to allow for ferromagnetic-like exchange interactions between the oxygen radical intermediates and the catalyst.[20, 21] These theoretical studies are corroborated by experiments on ferromagnetic catalysts for which the magnetization state was shown to affect the OER efficiency.[22, 23] The utility of spin-alignment for enhancing OER efficiency was demonstrated convincingly by Garces-Pineda and coworkers who showed that an external magnetic field caused a two-fold increase in current densities (above 100 mA cm^{-2}) at high applied bias voltage.[24]

Recent research suggests that electrocatalysts coated with chiral molecules[25-27] and intrinsically chiral CuO,[10] can be used to align the electron's spin orientation and enhance the OER. By a comparison of chiral catalysts with their achiral analogues, these studies showed a reduction in the overpotential for the OER. The enhanced efficiency for O_2 ($^3\Sigma_g^-$) production was attributed to the formation of spin-polarized radical intermediates on the electrocatalyst's surface because of the chiral induced spin selectivity (CISS) effect.[28-31] The CISS effect says that electrons (or holes) moving through a chiral electrocatalyst become spin-polarized; that is, there is a preference to have the spin aligned either parallel or antiparallel to the electron's velocity. Thus, as reactants (such as water or hydroxide) become oxidized on a chiral anode they inject, preferentially, electrons of one spin type. For singlet state reactants (such as hydroxide), the radical intermediates that are generated on the chiral anode surface have their electron spins polarized preferentially whereas those formed on an achiral anode surface are not necessarily polarized. Prior to this study with CoO_x, chiral electrocatalysts comprised long organic molecules as the spin-filtering agent or used chiral CuO which is not a very efficient water splitting catalyst (relatively high overpotentials). Moreover, earlier work with chiral catalysts have not discussed how pH dependent changes in mechanism may affect the role of spin-polarized reaction intermediates. This study explores the OER reaction with an efficient CoO_x chiral electrocatalyst over a range of alkaline pHs.

Previous studies on mixed cobalt oxide and cobalt oxide hydroxide catalysts have shown that they are some of the best electrocatalysts for the OER, with overpotentials ranging from 0.238 V to 0.290 V.[32] In this work, we show how to fabricate chiral cobalt oxide/oxyhydroxide (CoO_x) anodes, through the electrodeposition from solutions of $CoCl_2$ and tartaric acid. Because the reaction overpotential for water splitting is sensitive to choices about the pH, electrolyte, mass loading, and the active catalytic area[11, 33] this work focuses on how chirality affects the catalyst performance, rather than more general comparisons to the state-of-the-art in the literature. The findings of this study demonstrate that chiral CoO_x thin films enhance the catalytic efficiency for water splitting, compared to its achiral analogue, over a pH range from pH 13 to pH 6.5. In addition, we show that the electrochemical conversion of these CoO_x films to a paramagnetic phase causes them to display a dependence of their OER efficiency on an external magnetic field. Lastly, we propose a mechanistic picture that describes the role of spin polarization in electrochemically generated radical intermediates over the pH range.

5.2 RESULTS AND DISCUSSION

5.2.1 Film Preparation and Characterization

Chiral cobalt oxide thin films were prepared by modifying previously developed protocols.[34] Briefly, the electrodeposition was performed at a constant potential of 0.9 V vs. NHE in an aqueous solution containing 4 mM of $CoCl_2 \cdot 4H_2O$, 0.1 M Na_2CO_3, and 40 mM of L-, D-, or meso-tartaric acid. Previous studies indicate that the electrodeposition process involves a redox transition from Co(II) in solution to Co(III)/Co(IV) species, such as Co_3O_4, CoOOH, or Co_2O_3, in the electrodeposited films.[30] The thickness of the film was controlled by the deposition time and it was quantified using profilometry. For practical purposes, instead of measuring the thickness for each film a calibration curve of thickness vs absorbance was used (See Figure D.1 and Appendix D for more details).

To ensure a valid comparison of catalytic efficiency between L- and meso-CoO_x thin films, the physical and morphological features of the films were characterized. Figure 5.1a shows X-ray photoelectron spectroscopy (XPS) data (normalized to the Co $2p_{3/2}$ maxima) for L- (black, bottom) and meso-CoO_x (blue, top) in which the satellite structure between 784 and794 eV (see zoomed in view in Figure 5.1b), indicates that the oxide / hydroxide content is remarkably similar. A more detailed analysis and discussion of the XPS spectra on the composition and properties of the CoO_x catalysts are provided in the Appendix D. Figure 5.1c shows X-ray diffraction (XRD) patterns for

L- (black, bottom) and meso-CoO_x (blue, top) thin films on FTO which corroborate the XPS data. The peaks arising from CoO_x and FTO are labeled in accordance with previous literature assignments[35] and both spectra show similar peak 2θ positions and peak intensity ratios. Although it is difficult to determine the exact composition of the materials, because of the large number of possible oxide / oxyhydroxide states overlapping in the spectral region, the similarity between the L-CoO_x and meso-CoO_x in the XPS and XRD imply that the catalysts are the same with the exception of film's overall chirality. Figure 5.1d shows top-down SEM images of L- (black border, left) and meso-CoO_x (blue border, right) thin films. Both images show similar morphological structure. Although the geometrical area of the substrates that are used for these studies is 1 cm^2, the electrochemical surface area can change between films because of changes in the surface roughness. To ensure this was not the case, the electrochemical surface area was measured using the double layer capacitance method,[36] and it was found to be very similar for L- and meso-CoO_x; see Appendix D and Figure D.6 for details. The surface structure was further probed by AFM topography measurements which indicate that the L-CoO_x and meso-CoO_x exhibit comparable surface roughness; See Figure D.7

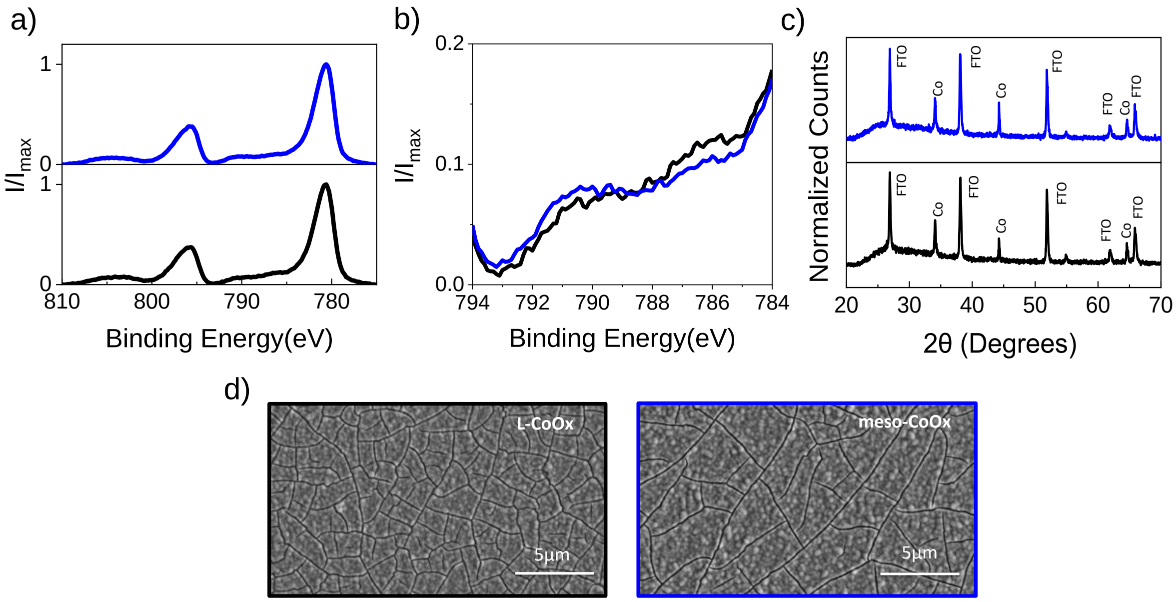

Figure 5.1 (a) XPS spectra of L- (black) and meso-CoO$_x$ (blue) thin films deposited on FTO. (b) Zoomed in view in the satellite spectral region from (a). (c) XRD spectra for L- (black, bottom) and meso-CoO$_x$ (top, blue) thin films. The peaks arising from the substrate and CoO$_x$ are labeled. (d) Corresponding top-down SEM images of L- (black border, left) and meso-CoO$_x$ (blue border, right) thin films.

To study the optical properties of the CoO$_x$ films, the substrate was changed to gold coated quartz which allows for better transmittance in the UV spectral region. Figure 5.2 shows absorbance (a) and circular dichroism (b) measurements on CoO$_x$ thin-films that were deposited from solutions containing complexes of Co^{2+} with L-tartaric acid (black), D-tartaric acid (red), and meso-tartaric acid (blue). The feature at 325-450 nm is associated with a Co–O ligand-to-metal charge transfer transition.[37] A higher energy transition, occurring to the blue, is also observed and is consistent with reports on other cobalt oxides.[38] Similarity in the UV-Vis spectra along with the aforementioned characterization methods between L-, D-, and meso-CoO$_x$ samples confirms that the composition, morphology, and thickness of the films are comparable. The mirror image Cotton effects in the circular dichroism spectra in L- and D-CoO$_x$ indicate the chirality of the thin films.

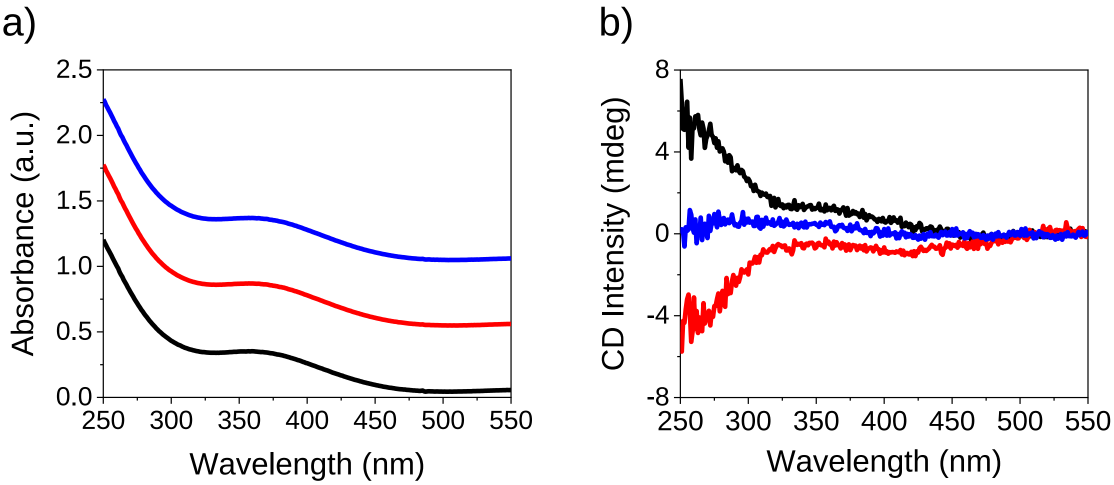

Figure 5.2 (a,b) Absorbance and circular dichroism spectra, respectively, of L- (black), D- (red), and meso-CoOx (blue) thin films electrodeposited on 10 nm thick gold coated quartz. The absorbance data are offset by 0.5 absorbance units for clarity.

More importantly, the opposite signal arising at the Co - O charge transfer transition indicates that the chirality is imprinted onto the electronic structure of the catalyst. The chirality is thought to arise in an analogous manner to that reported for CuO, in which tartaric acid can direct the deposition of the material so that high index (chiral) planes of the crystallites in these polycrystalline films are preferentially presented on the surface.[10, 39] During the electrodeposition the L- and D-tartrate ligands act to select these index planes enantiospecifically which gives rise to the approximate mirror symmetry. In contrast, the meso-tartrate with its two opposite chirality centers has no such bias and a null CD response is obtained.

5.2.2 Water Splitting Study

Figure 5.3A shows linear sweep voltammograms for the chiral L-CoO_x (black) and meso-CoO_x (blue) thin film electrodes in 0.1 M KOH. A large increase in current is evident for both CoO_x films as compared to a bare FTO substrate (green), indicating their electrocatalytic activity.

The reaction overpotential, defined as the voltage needed to maintain a current density of 10 mA/cm^2, is found to be 64 mV lower (13%) for the L-CoO$_x$ than for the meso-CoO$_x$. The difference in applied potential needed to generate a given current density increases between the chiral and meso electrocatalysts at larger current densities; 105 mV at 20 mA/cm^2 (20%) and 159 mV (28%) at 40 mA/cm^2. Figure 5.3b shows voltammograms of chiral L-CoO$_x$ (black) and meso-CoO$_x$ (blue) thin films at pH 10 in sodium carbonate / bicarbonate buffer solution. A similar difference in overpotential is observed at 3 mA/cm^2 between the measurements at pH 10 and pH 13; ~25mV. The surface area of the two catalysts was found to be the same by using a double layer capacitive current method; note that the surface area of the meso-CoO$_x$ would need to be ~3 time higher to match the overpotential of L-CoO$_x$ at 30 mA/cm^2 current density. Tafel analysis of L- and meso-CoO$_x$ films is presented in the Appendix D, see Figure D.8. The Tafel slope, which indicates the amount of overpotential required to increase the reaction rate by a factor of 10, is approximately ~1.3-fold lower for L-CoO$_x$ (101 mV/dec) than for meso-CoO$_x$ (133 mV/dec) at pH 13. The improvement in the current-voltage behavior for the L-CoO$_x$ is similar in magnitude to other chiral electrocatalysts,[26] however the CoO$_x$ catalysts in this study are operating at much higher current densities and lower overpotentials. While the emphasis of these studies is on the comparison between L- and meso-CoO$_x$ it is important to note that previous studies on OER of chiral materials show that D and L enantiomers exhibit similar behavior.[10, 26] To verify this, linear sweep voltammograms comparing D-CoOx and meso-CoO$_x$ were collected and are shown in Figure D.9 and table D.2. A notable improvement is again observed using the chiral catalyst, D-CoO$_x$, compared to the meso-CoO$_x$

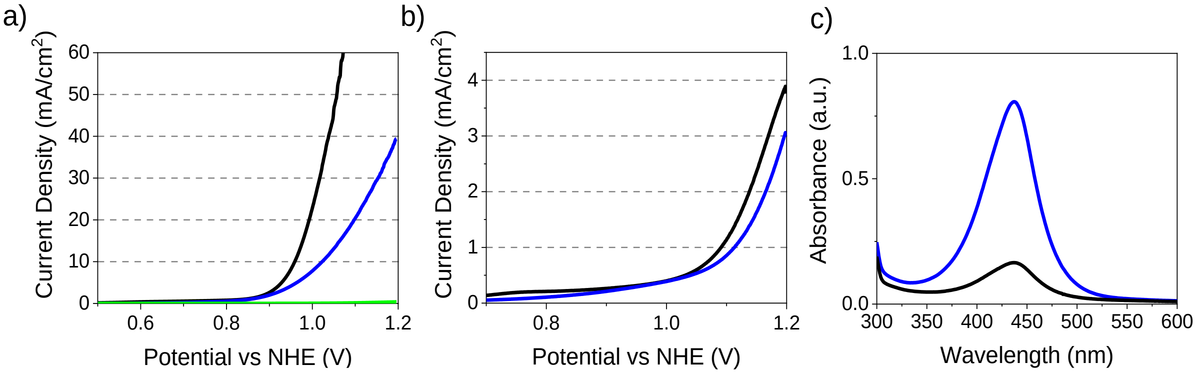

Figure 5.3 (a) Linear sweep voltammograms for the OER using L-CoO$_x$ (black), meso-CoO$_x$ (blue), and a bare FTO substrates (green) in 0.1M KOH. (b) Linear sweep voltammograms of the OER using L-CoO$_x$ (black) and meso-CoO$_x$ (blue) in Na_2CO_3/$NaHCO_3$ (pH 10). (c) UV-Vis absorption spectra of hydrogen peroxide using L-CoO$_x$ (black) and meso-CoO$_x$ (blue) catalysts. Following electrolysis the solutions are titrated with o-tolidine indicator. The integrated peak area reflects the amount of hydrogen peroxide present, see text for additional details.

A competing pathway for the oxygen evolution reaction at neutral pH is the formation of hydrogen peroxide. To study the role of chirality, more specifically the chirality-induced spin alignment of radical intermediates, for inhibiting hydrogen peroxide formation, electrochemical experiments were performed in which 1.5 V vs. NHE was applied to a CoO$_x$ thin film for 45 min in a 0.1 M Na_2SO_4 solution at pH=6.5. Following the reaction, a spectrophotometric redox indicator, o-tolidine, was added to the solution and the absorbance was measured. Figure 5.3c shows the change in absorption of o-tolidine, and hence the amount of hydrogen peroxide production, when the water splitting reaction is performed using L-CoO$_x$ (black) and meso-CoO$_x$ (blue) as the electrocatalyst. Integrating the absorbance peaks of these data indicate that the meso-CoO$_x$ produces 4-times more hydrogen peroxide than is produced for the L-CoO$_x$, despite the lower current density of meso-CoO$_x$ at the applied potential. Thus, the chiral electrocatalyst is more selective against peroxide generation, than is the meso-catalyst

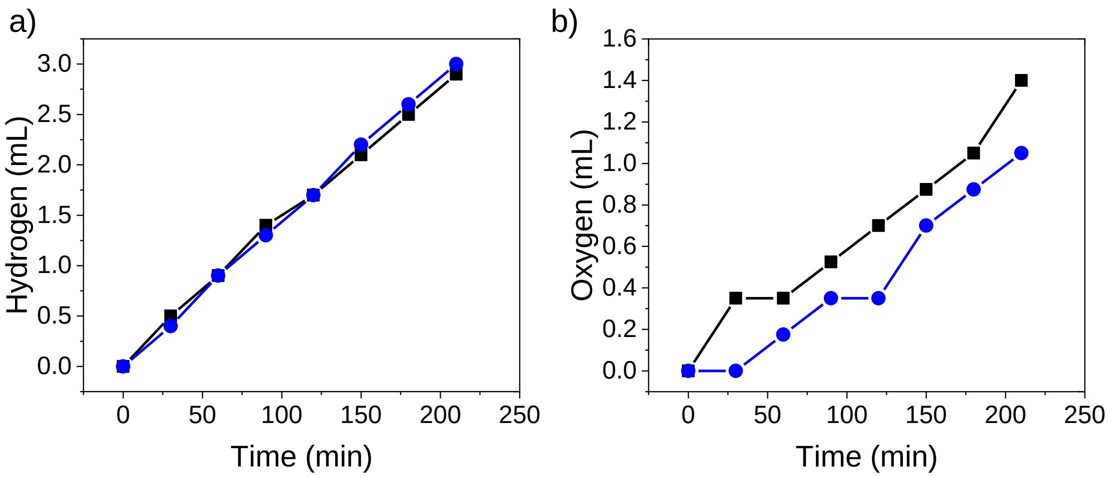

Figure 5.4 Representative Hoffman apparatus measurements for hydrogen production (left) and oxygen production (right) with L- (black) and meso-CoO_x (blue) catalysts. The water splitting was performed at a 5.0 mA / cm^2 current density in a sodium carbonate / bicarbonate pH 10 buffer solution.

This phenomenon was investigated further by quantitatively measuring the hydrogen and oxygen yield using a Hoffman apparatus, Figure 5.4. Experiments with Pt as both the anode and cathode were used to standardize the apparatus to the expected 2:1 hydrogen-to-oxygen ratio and account for any instrumental deviations. Measurements were performed using a pH 10 sodium carbonate / bicarbonate buffer solution at a current density of 5.0 mA / cm^2. The hydrogen production (panel a) was similar for the L-CoO_x (blue) and meso-CoO_x (black) catalysts, however more oxygen (panel b) was produced for the chiral catalyst. Table 5.1 shows the average ratio of H_2 to O_2 production across multiple experiments at pH 10 and pH 13 (0.1 M KOH). Because the formation of hydrogen peroxide is unfavorable at high pH, pK_{a1} of 11.7, the H_2:O_2 ratio for the chiral and meso catalysts are nearly the same; ~2.1:1.0. Thus, the difference in overpotential, arising from the more favorable pathway for O_2 ($^3\sum_g^-$) formation in the chiral catalyst, is compensated for by operating at a fixed current density (higher bias voltage). Conversely, at a lower pH where hydrogen peroxide formation is favorable, the chiral catalyst creates more oxygen (2.4:1.0) than the meso catalyst (3.7:1.0) further corroborating the findings in Figure 5.3c. By fitting the data for oxygen production and averaging across multiple electrodes we find that the oxygen evolution rate for chiral catalysts is ~1.4 times larger than that for meso catalysts.

Table 5.1 Average ratios of hydrogen-to-oxygen production measured using a Hoffman apparatus for multiple L- amd meso-CoOx catalysts in sodium carbonate/bicarbonate pH 10 buffer solutions at a 5.0 mA/cm^2 current density and pH 13 (0.1 M KOH) solutions at 10 mA/cm^2 current densities.

H_2:O_2	**L-CoO_x**	**meso-CoO_x**
pH 10	2.4:1.0	3.7:1.0
pH 13	2.2:1.0	2.1:1.0

5.2.3 A Mechanistic Scheme for OER at Different pH

From our experimental studies at different pH values, we propose a mechanistic scheme that can explain the observed effects (Figure 5.5). Figure 5.5a shows a model lattice representing the polarization of the electron spin of radical intermediates (down, blue ball and up, red ball) on a chiral (left) and achiral catalyst surface (right). For chiral catalysts, the spin at adjacent sites on the lattice of intermediates are mostly aligned, because of the CISS effect. This model is consistent with spin polarization measurements made on other chiral metal oxides.[10] For achiral catalysts, however, CISS does not operate and alignment of the spin at adjacent sites does not occur. When the pH is high (pH 13) the electrochemical intermediates are mostly dominated by radical oxygen formation.[40, 41] For the chiral catalysts at high pH **(1)**, the spins at adjacent reaction sites are aligned parallel (↑O···O↑) and thus favor the formation of triplet oxygen (↑O-O↑). Conversely, for achiral catalysts at high pH **(3)** the spins at adjacent sites on the catalyst are mixed; both parallel (↑O···O↑) and antiparallel (↑O···O↓) configurations exist. Because the ground state of oxygen is a triplet, formation of oxygen from the antiparallel alignment is spin forbidden which decreases the rate constant because of differences in the activation energy and/or the need for transitioning between the triplet and singlet reaction pathways. For example, Chrétien and Metiu[9] calculated more than a 0.5 eV activation barrier difference for the singlet and triplet pathways of O_2 on TiO_2/Au catalytic surfaces. Such differences could account for the change in overpotential between L- and meso-CoO_x, as shown in Figure 5.3 and explain why the ratio of H_2/O_2 is the same at high pH when the same current density is applied (higher bias voltage); see Table 5.1.

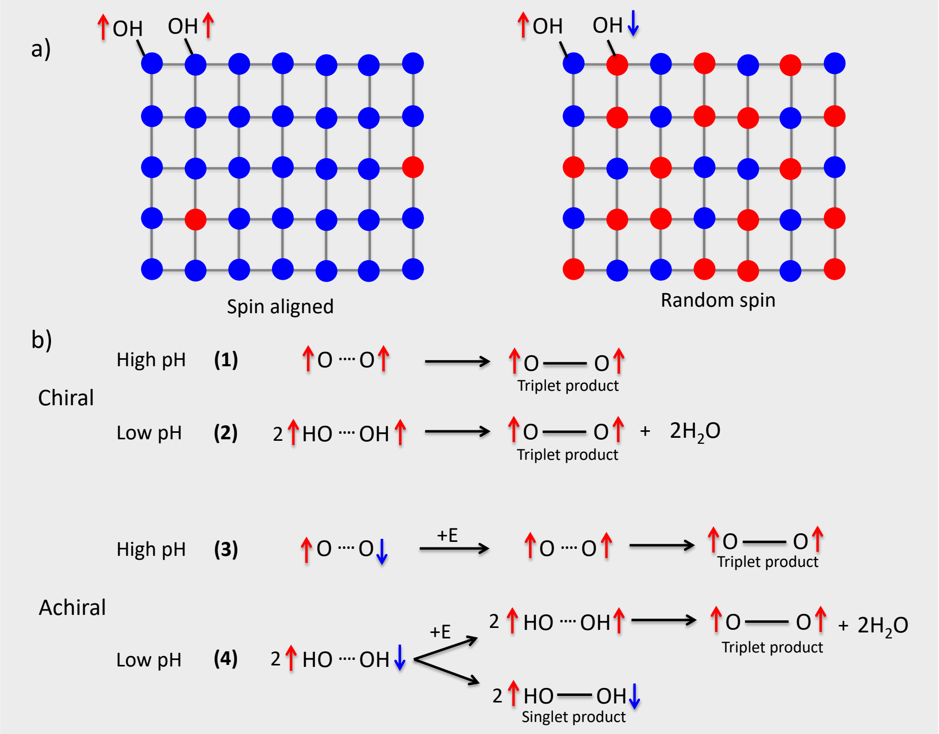

Figure 5.5 Proposed, mechanistic scheme explaining the role of spin polarization during water splitting. (a) model lattice where the color of the ball represents the spin of the radical absorbate (shown here as hydroxyl) at the catalyst side; blue indicates down spin and red indicates up spin. For chiral catalysts (left), because of the CISS effect, the electrons at adjacent sites tend to be spin aligned; and hence the formation of triplet oxygen will be favored. Conversely, for achiral catalysts more spin disorder exists at adjacent sites necessitating either a change in spin state or reaction on a singlet reaction pathway with a higher activation barrier to form triplet oxygen. (b) Mechanism of product formation at different pH valuess. For chiral catalysts, the formation of triplet oxygen is favored at high pH, when the reactant is radical oxygen (1), and at lower pH in which hydroxyl radical intermediates can also occur (2). For achiral catalysts at higher pH (3) the formation of triplet oxygen can proceed, but is slowed by the spin disorder, and at lower pH, (4), the production of H_2O_2 can compete with the more sluggish triplet oxygen. The dotted line between the atoms indicates the intermediate state, the solid line represents a chemical bond, and +E indicates a higher activation barrier.

As the pH decreases (pH 10) both radical oxygen and hydroxyl radicals will contribute significantly to the population of intermediates, and the general mechanistic picture changes because the H_2O_2 reaction pathway becomes more competitive. For chiral catalysts with hydroxyl intermediates **(2)**; spin alignment (↑HO···OH↑) favors the formation of triplet oxygen (↑O-O↑). Whereas for achiral catalysts a new pathway emerges, **(4)**, and competes with the formation of triplet oxygen; the thermodynamically favored pathway for the parallel (↑HO···OH↑) spin alignment is (↑O-O↑) and the thermodynamically favored process for antiparallel (↑HO···OH↓) alignment is (↑HO-OH↓). This new pathway emerges at lower pH because of the stability of the H_2O_2 product and manifests as a difference in oxygen yield, presented in Table 5.1 at pH 10 and the amount of H_2O_2 produced at pH 6.5 in Figure 5.3c. This proposed mechanism is supported by previous studies showing that the reaction leading to molecular intermediates from a separated atom configuration (O···O) at a higher pH is thermodynamically more stable in the case of triplet species compared to singlet species.[9]

5.2.4 Magnetic Field Dependent Water Splitting

An alternative means for controlling the spin alignment of the radical intermediates is through the use of a magnetized electrocatalyst surface. Figure 5.6a shows current *versus* time curves of an L-CoO_x thin film electrode (conditions are 0.9 V vs. NHE at pH 13) with no applied magnetic field (white) and with the application of an external 0.4 T field (pink). The as synthesized CoO_x thin film exhibits very weak, nearly negligible, changes in current density with an external magnetic field. This is because the film comprises mostly Co(III) species which are diamagnetic and therefore no net magnetic moment is generated.[42] Figure 5.6b shows current-time data for a film that was biased at 1.2 V vs NHE for 30 min in 0.1 M KOH, which converts the average oxidation state of the CoO_x catalyst from Co(III) to Co(IV) and forms a paramagnetic material.[43] This change in magnetic properties upon treatment is consistent with the Pourbaix diagram, which indicates the formation of Co(IV) (a paramagnetic species) at higher applied potentials,[44, 45] and with EPR measurements.[11, 46] As Figure 5.6b shows, these films display an apparent increase in the current upon application of a magnetic field. Note that the data sets in Figure 5.6 were obtained sequentially, first the data in Figure 5.6a were collected; and after the electrochemical treatment, the data in Figure 5.6b were collected. The absorbance spectra, circular dichroism, and XPS spectra, which support the change in the film composition, are presented in the Appendix D (Figure D.2, and Figure D.10).

The fact that a magnetic field dependence is observed after the applied voltage treatment, and not before, implies that the magnetic field enhancement of the OER arises from spin polarization properties of the electrocatalyst surface, rather than transport effects, such as diffusion of reagents and gas bubbles because of Lorentz forces acting on the solution - as shown by others.[47] Given that the primary difference in the CoO_x films in Figure 5.6a,b is the Co oxidation state, the emergence of a magnetic field effect must be rooted in the spin alignment of the active sites/species during the reaction. That is, the external magnetic field aligns (spin polarizes) the radical intermediates on the paramagnetic CoO_x, similar to the effect of chirality, and favors the O_2 ($^3\Sigma_g^-$) pathway. These results are consistent with the study of Garces-Pineda[24] for ferromagnetic electrodes and the theoretical work of Gracia who has identified that spin dependent interactions can improve the OER in perovskite electrocatalysts.[22]

Figure 5.6c shows the magnetocurrent (j_m) as a function of the potential used to treat the film. In this study the film is treated with a particular potential for 20 min and the magneto-response was measured. Then, the sample was treated again with a higher potential and followed with another magnetocurrent measurement. This process was repeated from an applied bias of 0.8 V to 2.6 V vs. NHE. Initial treatment of the film results in a higher magneto-response with higher applied potential and indicates that more paramagnetic Co(IV) is produced. Eventually the effect saturates; no further changes in magneto-current with applied bias are observed. To probe the cooperative effects between the paramagnetic Co(IV) with that of chirality, linear sweep voltammograms were measured for treated CoO_x thin films with the application of a North and South external magnetic field (Figure D.11). Despite the thin film still exhibiting chiroptical properties, a difference in overpotential between the external magnetization was not observed. This implies that the magnetic field effect, arising from the spin sub-band splitting of the catalyst, dominates the spin orientation of the electrochemically generated radical intermediates over that of the chirality.

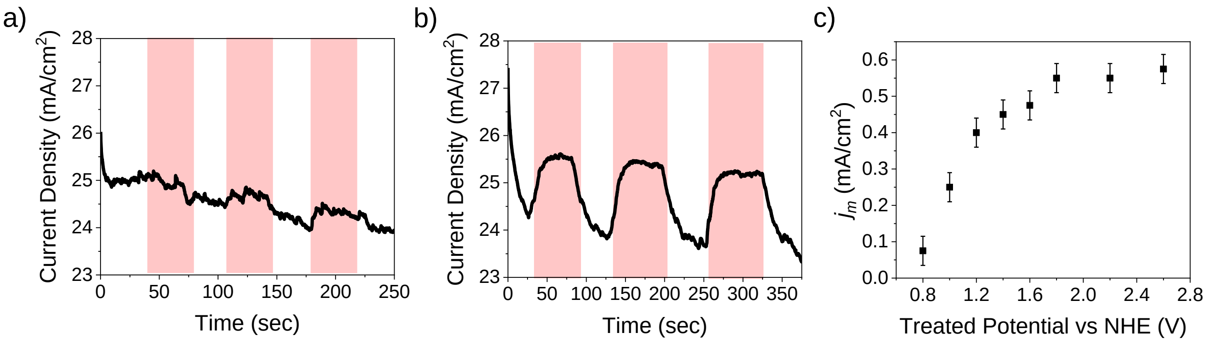

Figure 5.6 Current-time response of CoO_x films before (a) and after (b) treating the film at 1.2 V vs NHE in 0.1 M KOH for 30 min. The light pink region indicates applications of a 0.4 T external magnetic field. (c) change in magnetoresponse (j_m) for L-CoO_x thin films as a function of the potential used to treat the film.

5.3 CONCLUSION

By creating chiral CoO_x electrocatalysts that can support high current densities, this work substantiates and extends earlier claims that controlling the spin polarization of radical intermediates is an important strategy for improving the OER efficiency. Efficiency improvements were demonstrated by using chiral cobalt oxide thin films, which impart a spin polarization through the CISS effect, and by creating paramagnetic CoO_x films which can be spin polarized with an external magnetic field. The improvement in water splitting manifests in two ways. First, the reaction overpotential decreases by 65 mV at a benchmark current density of 10 mA/cm^2. Second, the oxygen yield increased by 1.4 times at pH=10 by reducing the formation of the H_2O_2 side-product. This difference becomes increasingly important at pH=6.5 where a 4-fold decrease in H_2O_2 was observed. These studies are outlined within a proposed mechanistic model that describes how the spin-filtering of electron injection can enhance reaction selectivity and points to a strategy for improving water electrolysis at neutral pH.

5.4 CAVEAT

The experiments shown in this project demonstrate that the catalytic activity of the cobalt oxide made from chiral tartaric acid outperforms the catalysts that are made from meso tartaric acid. Although, the CD spectroscopy confirms the chirality of the film as a whole, the active center of the catalysts might still be achiral. The difference in the catalytic activity between meso and L-catalysts might come from other properties of the active center or because of the different numbers of the active sites in the catalysts. It is certain that the spin plays an important role in the water splitting as shown by the magnetic field dependent OER study with the paramagnetic catalysts. But in order to unequivocally prove that the spins role in the chemical reaction is linked to the chiral nature of the catalyst will require more extensive studies focused on the chirality of the active centers.

5.5 EXPERIMENTAL METHODS

5.5.1 Formation of Cobalt Oxide Thin Film

Cobalt oxide films were prepared using an electrochemical deposition method. For the electrodeposition, 0.8 mmol of L-, D-, or meso-tartaric acid and 0.08 mmol of $CoCl_2 \cdot 6H_2O$ was added to 10 ml of water. Next, 2 mmol of Na_2CO_3 was added to the solution and the total volume was increased to 20 mL. A three electrode electrochemical cell was employed for the deposition in which a fluorine-doped tin oxide (FTO) coated glass substrate, or a 10 nm gold coated quartz substrate, was used as the working electrode. A Pt sheet and Ag│AgCl were used as the counter and reference electrodes, respectively. For the deposition, a constant potential of 0.7 V was applied using a CH Instruments 430a potentiostat, and the thickness of the film was controlled by the deposition time. Following electrodeposition, the film was washed with copious amounts of water and dried under a stream of argon.

5.5.2 Circular Dichroism

Circular dichroism measurements were performed using an Olis DSM 17 CD spectrometer with an integration time of 3 sec and a bandwidth of 1 nm. Measurements were made on gold coated quartz substrates which allow for higher transmission in the UV than FTO.

5.5.3 Oxygen Evolution Studies

Electrochemical measurements for the OER were performed in 0.1 M KOH or pH 10 sodium carbonate / bicarbonate buffer. A three electrode electrochemical cell was used for the electrochemical measurement. An FTO substrate deposited with L-, D-, or meso-CoO_x thin films was used as the working electrode, Ag│AgCl was used as the reference electrode, and a Pt sheet was used as the counter electrode. The electrochemical measurement was performed by using linear sweep voltammetry from 0.5V to 1.2 V vs Ag│AgCl with a scan rate of 20 mV/s

5.5.4 Hydrogen Peroxide Formation

Hydrogen peroxide formation was detected by the addition of a redox indicator o-tolidine. In the presence of hydrogen peroxide o-tolidine forms a yellow colored solution which has an absorption peak at 436 nm. For the hydrogen peroxide formation experiment, L- and meso-CoO_x were deposited on FTO coated glass substrates. Electrochemical experiments were performed in 0.1 M Na_2SO_4 (pH 6.5) solution at a constant potential of 1 V for 45 mins. Following the experiment, 3 ml of the electrolyte solution from the electrochemical cell was mixed with 1 ml of an o-tolidine indicator solution and the absorption was measured using a Model 8453 Agilent UV-Vis spectrometer.

5.5.5 Hoffman Apparatus

A modified Hoffman apparatus was used to measure the hydrogen and oxygen yield during water splitting. An additional port, adjacent to the working electrode was milled into the glass to allow for the presence of an Ag│AgCl reference electrode. First, a linear sweep voltammogram was measured to determine the potential at which a current density of 10 mA/cm^2 (for 0.1M KOH solutions) or 5 mA/cm^2 (for sodium carbonate/bicarbonate solutions) is achieved. Then, a fixed potential was applied and the volume displaced in the Hoffman apparatus was recorded every 10 min for KOH solutions and 30 min for sodium carbonate/bicarbonate solutions. The volume resolution of the instrument is 0.1 mL. To account for any imperfections in the apparatus, the hydrogen to oxygen ratio was standardized using Pt as both the anode and cathode. Deviations from a 2:1 ratio are expected to occur from poor oxygen saturation, and thus the measured volume of the oxygen for electrolysis with CoO_x electrodes was modified to reflect the H_2:O_2 ratio found in the Pt-Pt measurement.

5.5.6 Magnetic Field Effects on the Oxygen Evolution Reaction

Prior to the magnetic field dependent study, the film was first treated with a constant potential of 1.0 V vs Ag│AgCl for 1000 s in 0.1M KOH. Using the treated substrates, the effect of a magnetic field on the current was investigated. A constant potential of 1.2 V was used during the experiment and an external magnet was applied and then removed from the back of the substrate. The magnetic field acting on the surface of the electrode was measured with a gaussmeter to be 350- 400 mT.

5.5.7 Electrochemical Surface Area Calculation (ECSA)

ECSA was calculated using a double layer capacitance (C_{DL}) method following previously published protocols.[6] Briefly,

$$ECSA = C_{DL}/C_s$$

where C_s is the specific capacitance of the sample or the capacitance of an atomically smooth planar surface of the material under identical electrolyte conditions, and C_{DL} is measured using cyclic voltammetry at a potential region where no Faradaic processes occur. Here, cyclic voltammograms were measured at different scan rates (0.05- 3.2 V/s) in 1 M NaOH solutions within a potential range of -0.3 - 0.5V vs Ag/AgCl. The double layer charging current is the product of C_{DL} and the scan rate such that a plot of current vs scan rate gives a slope of C_{DL}.

5.5.8 X-Ray Photoelectron Spectroscopy (XPS)

XPS data were collected on an ESCALAB 250XI instrument. The data were referenced to an adventitious carbon peak of 284.8 eV and measured before and after a soft ion sputter cleaning (1000 eV for 10 seconds) to ensure that the treatment was not changing the oxidation state of the metal oxide. The data were collected while using a flood gun to compensate for surface charging. Each spectrum represents the average of 20 scans.

5.5.9 X-Ray Diffraction (XRD)

Powder XRD patterns were collected using a Bruker AXS D8 Discover XRD (NanoScale Fabrication and Characterization Facility, Petersen Institute of NanoScience and Engineering, Pittsburgh, PA) equipped with a Cu Kα (λ α = 1.5406 Å) X-ray source operating at 40 kV and 40 mA. The diffracted beam was detected using a Bruker AXS Lynxeye (silicon strip) detector. PXRD patterns were collected using a continuous lock-coupled scan with a scan speed of 0.25 Sec/Step from 15.00^o to 95.00^o with a step size of 0.025^o.

5.5.10 SEM Study

Imaging was performed using an FEI Scios focused ion beam (FIB) / scanning electron microscope (SEM) dual-beam system (Nanoscale Fabrication and Characterization Facility, Petersen Institute of NanoScience and Engineering, Pittsburgh, PA).

5.5.11 Atomic Force Microscopy Measurement

Atomic force microscopy measurements were performed using an Asylum Research MFP-3D atomic force microscope. The meso- and L-CoOx samples were prepared on FTO substrates and the surface topography was measured in non-contact mode.

5.6 REFERENCES

1.El-Shafie, M.; Kambara, S.; Hayakawa, Y., Hydrogen Production Technologies Overview. *J. Power Energy Eng.* **2019,** *07*, 107.

2.Turner, J. A., Sustainable Hydrogen Production. *Science* **2004,** *305*, 972.

3.Lewis, N. S., Toward Cost-Effective Solar Energy Use. *Science* **2007,** *315*, 798.

4.McKone, J. R.; Lewis, N. S.; Gray, H. B., Will Solar-Driven Water-Splitting Devices See the Light of Day? *Chem. Mater.* **2014,** *26*, 407.

5.McCrory, C. C.; Jung, S.; Peters, J. C.; Jaramillo, T. F., Benchmarking Heterogeneous Electrocatalysts for the Oxygen Evolution Reaction. *J. Am. Chem. Soc.* **2013,** *135*, 16977.

6.McCrory, C. C. L.; Jung, S.; Ferrer, I. M.; Chatman, S. M.; Peters, J. C.; Jaramillo, T. F., Benchmarking Hydrogen Evolving Reaction and Oxygen Evolving Reaction Electrocatalysts for Solar Water Splitting Devices. *J. Am. Chem. Soc.* **2015,** *137*, 4347.

7.Lin, Y.; Tian, Z.; Zhang, L.; Ma, J.; Jiang, Z.; Deibert, B. J.; Ge, R.; Chen, L., Chromium-Ruthenium Oxide Solid Solution Electrocatalyst for Highly Efficient Oxygen Evolution Reaction in Acidic Media. *Nat. Commun.* **2019,** *10*, 162.

8.Song, F.; Bai, L.; Moysiadou, A.; Lee, S.; Hu, C.; Liardet, L.; Hu, X., Transition Metal Oxides as Electrocatalysts for the Oxygen Evolution Reaction in Alkaline Solutions: An Application-Inspired Renaissance. *J. Am. Chem. Soc.* **2018,** *140*, 7748.

9.Chrétien, S.; Metiu, H., O2 Evolution on a Clean Partially Reduced Rutile TiO2 (110) Surface and on the Same Surface Precovered with Au1 and Au2: The Importance of Spin Conservation. *J. Chem. Phys.* **2008,** *129*, 074705.

10.Ghosh, K. B.; Zhang, W.; Tassinari, F.; Mastai, Y.; Lidor-Shalev, O.; Naaman, R.; Mollers, P.; Nurenberg, D.; Zacharias, H.; Wei, J.; Wierzbinski, E.; Waldeck, D. H., Controlling Chemical Selectivity in Electrocatalysis with Chiral CuO Coated Electrodes. *J. Phys. Chem. C* **2019,** *123*, 3024.

11.Gerken, J. B.; McAlpin, J. G.; Chen, J. Y. C.; Rigsby, M. L.; Casey, W. H.; Britt, R. D.; Stahl, S. S., Electrochemical Water Oxidation with Cobalt-Based Electrocatalysts from pH 0-14: The Thermodynamic Basis for Catalyst Structure, Stability, and Activity. *J. Am. Chem. Soc.* **2011,** *133*, 14431.

12.Smith, A. F.; Nicoll, W. D., Stability of Stability of Dilute Alkaline Solutions of Hydrogen Peroxide. *Ind. Eng. Chem.* **1955,** *47*, 2548.

13.Seabold, J. A.; Choi, K. S., Effect of a Cobalt-Based Oxygen Evolution Catalyst on the Stability and the Selectivity of Photo-Oxidation Reactions of a WO3 Photoanode. *Chem. Mater.* **2011,** *23*, 1105.

14.Torun, E.; Fang, C. M.; de Wijs, G. A.; de Groot, R. A., Role of Magnetism in catalysis: RuO2 (110) surface. *J. Phys. Chem. C* **2013,** *117*, 6353.

15.Suntivich, J.; Gasteiger, H. A.; Yabuuchi, N.; Nakanishi, H.; Goodenough, J. B.; Shao-Horn, Y., Design Principles for Oxygen-Reduction Activity on Perovskite Oxide Catalysts for Fuel Cells and Metal–Air Batteries. *Nat. Chem.* **2011,** *3*, 546.

16.Suntivich, J.; May, K. J.; Gasteiger, H. A.; Goodenough, J. B.; Shao-Horn, Y., A Perovskite Oxide A Perovskite Oxide Optimized for Oxygen Evolution Catalysis from Molecular Orbital Principles. *Science* **2011,** *334*, 1383.

17.Zhou, S.; Miao, X.; Zhao, X.; Qiu, Y.; Hu, Z.; Zhao, J.; Shi, L.; Zeng, J., Engineering Electrocatalytic Activity in Nanosized Perovskite Cobaltite through Surface Spin-State Transition. *Nat. Commun.* **2016,** *7*, 11510.

18.Chen, S.; Kang, Z.; Hu, X.; Zhang, X.; Wang, H.; Xie, J.; Zheng, X.; Yan, W.; Pan, B.; Xie, Y., Delocalized Spin States in 2D Atomic Layers Realizing Enhanced Electrocatalytic Oxygen Evolution. *Adv. Mater.* **2017,** *29*, 1701687.

19.Pan, L.; Ai, M.; Huang, C.; Yin, L.; Liu, X.; Zhang, R.; Wang, S.; Jiang, Z.; Zhang, X.; Zou, J.; Mi, W., Manipulating Spin polarization of Titanium Dioxide for Efficient Photocatalysis. *Nat. Commun.* **2020,** *11*, 418.

20.Sharpe, R.; Munarriz, J.; Lim, T.; Jiao, Y.; Niemantsverdriet, J. W.; Polo, V.; Gracia, J., Orbital Physics of Perovskites for the Oxygen Evolution Reaction. *Top. Catal.* **2018,** *61*, 267.

21.Gracia, J., Spin Dependent Interactions Catalyse the Oxygen Electrochemistry. *Phys. Chem. Chem. Phys.* **2017,** *19*, 20451.

22.Liang, X.; Yang, Z., Self-Magnetic-Attracted NixFe(1–x)@NixFe(1–x)O Nanoparticles on Nickel Foam as Highly Active and Stable Electrocatalysts towards Alkaline Oxygen Evolution Reaction. *Nano Res.* **2020,** *13*, 461.

23.Davodi, F.; Muhlhausen, E.; Tavakkoli, M.; Sainio, J.; Jiang, H.; Gokce, B.; Marzun, G.; Kallio, T., Catalyst Support Effect on the Activity and Durability of Magnetic Nanoparticles: toward Design of Advanced Electrocatalyst for Full Water Splitting. *ACS Appl. Mater. Interfaces* **2018,** *10*, 31300.

24.Garcés-Pineda, F. A.; Blaco-Ahicart, M.; Nieto-Castro, D.; Lopez, N.; Galán-Mascarós, J. R., Direct Magnetic Enhancement of Electrocatalytic Water Oxidation In Alkaline Media. *Nat. Energy* **2019,** *4*, 519.

25.Mtangi, W.; Tassinari, F.; Vankayala, K.; Jentzsch, A. V.; Adelizzi, B.; Palmans, A. R. A.; Fontanesi, C.; Meijer, E. W.; Naaman, R., Control of Electrons' Spin Eliminates Hydrogen Peroxide Formation During Water Splitting. *J. Am. Chem. Soc.* **2017,** *139*, 2794.

26.Zhang, W.; Ghosh, K. B.; Tassinari, F.; Naaman, R., Enhanced Electrochemical Water Splitting with Chiral Molecules-Coated Fe3O4 Nanoparticles. *ACS Energy Lett.* **2018,** *3*, 2308.

27.Mtangi, W.; Kiran, V.; Fontanesi, C.; Naaman, R., Role of the Electron Spin Polarization in Water Splitting. *J. Phys. Chem. Lett.* **2015,** *6*, 4916.

28.Naaman, R.; Waldeck, D. H., Chiral-Induced Spin Selectivity Effect. *J. Phys. Chem. Lett.* **2012,** *3*, 2178.

29.Naaman, R.; Waldeck, D. H., Spintronics and Chirality: Spin Selectivity in Electron Transport through Chiral Molecules. *Annu. Rev. Phys. Chem.* **2015,** *66*, 263.

30.Naaman, R.; Paltiel, Y.; Waldeck, D. H., Chiral Molecules and the Electron Spin. *Nat. Rev. Chem.* **2019,** *3*, 250.

31.Metzger, T. S.; Mishra, S.; Bloom, B. P.; Goren, N.; Neubauer, A.; Shmul, G.; Wei, J.; Yochelis, S.; Tassinari, F.; Fontanesi, C.; Waldeck, D. H.; Paltiel, Y.; Naaman, R., The Electron Spin as a Chiral Reagent. *Angew. Chem., Int. Ed.* **2020,** *59*, 1653.

32.Jamesh, M. I.; Sun, X. M., Recent Progress on Earth Abundant Electrocatalysts for Oxygen Evolution Reaction (OER) in Alkaline Medium to Achieve Efficient Water Splitting—A Review. *J. Power Sources* **2018,** *400*, 31.

33.Klingan, K.; Ringleb, F.; Zaharieva, I.; Heidkamp, J.; Chernev, P.; Gonzalez-Flores, D.; Risch, M.; Fischer, A.; Dau, H., Water Oxidation by Amorphous Cobalt-Based Oxides: Volume Activity and Proton Transfer to Electrolyte Bases. *ChemSusChem* **2014,** *7*, 1301.

34.Casella, I. G., Electrodeposition of Cobalt Oxide Films from Carbonate Solutions Containing Co(II)-tartrate Complexes. *J. Electroanal. Chem.* **2002,** *520*, 119.

35.Huang, Z.; Zhao, Y.; Song, Y.; Li, Y.; Wu, G.; Tang, H.; Zhao, J., Study on the Oxidation of Cobalt Hydroxide to Cobalt Oxides at Low Temperatures. *RSC Adv.* **2016,** *6*, 80059.

36.McCrory, C. C. L.; Jung, S.; Peters, J. C.; Jaramillo, T. F., Benchmarking Heterogeneous Electrocatalysts for the Oxygen Evolution Reaction. *J. Am. Chem. Soc.* **2013,** *135*, 16977.

37.Barreca, D.; Massigan, C., Composition and Microstructure of Cobalt Oxide Thin Films Obtained from a Novel Cobalt (II) Precursor by Chemical Vapor Deposition. *Chem. Mater.* **2001,** *13*, 588.

38.Ravindra, A. V.; Behera, B. C.; Padhan, P., Laser Induced Structural Phase Transformation of Cobalt Oxides Nanostructures. *J. Nanosci. Nanotechnol.* **2014,** *14*, 5591.

39.Kothari, H. M.; Kulp, E. A.; boonsalee, S.; Nikiforov, M. P.; Bohannan, E. W.; Roizot, P.; Nakanishi, S.; Switzer, J. A., Enantiospecific Electrodeposition of Chiral CuO Films from Copper(II) Complexes of Tartaric and Amino Acids on Single-Crystal Au(001). *Chem. Mater.* **2004,** *16*, 4232.

40.Nakabayashi, Y.; Nosaka, Y., The pH Sependence of OH Radical Formation in Photo-Electrochemical Water Oxidation with Rutile TiO2 Single Crystals. *Phys. Chem. Chem. Phys.* **2015,** *17*, 30570.

41.von Sonntag, C., *Free-Radical-Induced DNA Damage and Its Repair*. 2006.

42.Casella, I. G.; Guascito, M. R., Anodic Electrodeposition of Conducting Cobalt Oxyhydroxide Films on a Gold Surface. XPS Study and Electrochemical behavior in Neutral and Alkaline Solution. *J. Electroanal. Chem.* **1999,** *476*, 54.

43.Casella, I. G.; Guascito, M. R., Study of the Electrochemical Deposition and Properties of Cobalt Oxide Species in Citrate Alkaline Solutions. *J. Electroanal. Chem.* **2002,** *534*, 31.

44.Motohashi, T.; Katsumata, Y.; Ono, T.; Kanno, R.; Karppinen, M.; Yamauchi, H., Synthesis and Properties of CoO2, the x= 0 End Member of the LixCoO2 and NaxCoO2 Systems. *Chem. Mater.* **2007,** *19*, 5063.

45.Huang, L. F.; Rondinelli, J. M., Reliable Electrochemical Phase Diagrams of Magnetic Transition Metals and Related Compounds from High-Throughput ab initio Calculations. *npj Mater. Degrad.* **2019,** *3*, 26.

46.Kutin, Y.; CoX, N.; Lubitz, W.; Schnegg, A.; Rudiger, O., In Situ EPR Characterization of a Cobalt Oxide Water Oxidation Catalyst at Neutral pH. *Catalysts* **2019,** *9*, 926.

47.Elias, L.; Hegde, C., Effect of Magnetic Field on HER of Water Electrolysis on Ni-W Alloy. *Electrocatalysis* **2017,** *8*, 375.

6.0 CONCLUDING REMARKS

The work shown in the dissertation has explored fundamental aspects and applications of the chiral induced spin selectivity effect. Advancement of the CISS field depends on the understanding the mechanism and factors that influence the effect, as well as exploring different chiral systems to study various CISS mediated processes. The projects discussed here have explored some very important role of chiral molecules at the ferromagnetic interface that can unravel the mechanism of CISS effect and also investigated spin filtering properties of new types of chiral materials that can have application in memory devices or in electrocatalysis.

Chapter 2 shows a technique to induce magnetism using chiral molecules that occurs via spin exchange interaction between chiral molecules and a metallic surface. The results show that the asymmetric adsorption of chiral molecules onto the surface of superparamagnetic nanoparticles can induce ferromagnetism in those particles and that the magnetization direction depends on the handedness of the chiral molecules. Using this strategy, a stable ferromagnetic domain of 10 nm size, comprising the chiral molecule/nanoparticle, was created. This method promises to be very important for creating magnetic devices of nm size, which is otherwise difficult because of the superparamagnetic nature of materials at smaller sizes. The results introduce a new paradigm to chiral molecules where charge polarization induces spin polarization; a consequence of the CISS effect.

Chapter 3 of this dissertation presents a very important property of chiral molecules at the spinterface (ferromagnetic and chiral molecule interface.). In this project spin dependent charge penetration was studied at the ferromagnetic-chiral molecule interface. Surface potential microscopy measurements show that electron penetration from metal electrode into the chiral molecule depends on the chirality and magnetization direction. This work demonstrates that chiral molecules can control the electron density at the ferromagnetic interface spin dependent charge penetration was also studied with different magnetization strength, thickness of gold overcoat, and the length of the chiral material. Previous results on molecular based spintronics devices show that organic molecules at the ferromagnetic interface can influence the spin polarization and hence controls the device properties. This study show spin polarization at the chiral molecule and ferromagnetic interface can occur even without an external bias. These results might explain why organic spintronics devices sometimes show anomalous behavior.

Chapter 4 has demonstrated the spin filtering efficiency of a chiral cobalt oxide thin film. In this project spin dependent charge transfer through the chiral cobalt oxide thin film was studied using magnetic conductive AFM. It was found that conduction of electrons (or the current) depends on both the chirality and the spin orientation of the transmitted electrons. For L- cobalt oxide the spin down electron was found to be conducted more readily than the spin up electrons, and an opposite behavior was observed with D-Cobalt oxide film. Additional results show that doping the cobalt oxide with paramagnetic species (Mn^{3+}) increases the spin polarization. Efficient spin filtering through this material suggests that thin film chiral material can be used for spintronics type applications. Indeed, a spin valve based magnetoresistance device was also prepared and results show the resistance of the device depends on chirality and the magnetization direction. For future directions, the role of dopant interaction, crystal structure and composition of the film on spin polarization study will be important. The results indicate that paramagnetic species (or dopants) in the film might improve the device spin polarization.

Chapter 5 has demonstrated how controlling of electron spin via the CISS effect, during the oxygen evolution reaction, affects the reaction rate and product formation. The water splitting efficiency and the product formation for chiral and achiral catalysts were studied. Results on the electrocatalytic experiments on the oxygen evolution reaction in water splitting study show that the chiral material acts as a better catalyst than the achiral catalyst. Because the reaction involves hydroxyl radical intermediates, spin polarization (arising from CISS effect) enhances the triplet oxygen and suppresses the singlet mediated process. It was also shown magnetic field can also improve the water splitting efficiency with paramagnetic catalysts by controlling the spin of the surface site. A mechanistic picture of the effect of spin polarization for different product formation at different pH was also discussed. These results show that spin polarization of chiral or magnetic material improves the water splitting efficiencies thereby introducing newer avenues for future researchers to design novel chiral electrocatalysts based on spin polarization. This work suggests that the design principle for enhancing the water splitting activity of metal oxides is to improve their chiral ordered structured for maximum activity, which can be further improved by increasing the paramagnetic species concentration in the catalyst.

The work presented in this dissertation has explored some very important spin dependent properties at the interface between a ferromagnetic surface and chiral molecule. Controlling spin electron density or magnetization by the chiral molecules, as shown in Chapters 2 and 3, not only unveils some important aspects of the CISS effect but also reveals new strategies for creating spintronics devices based on the CISS effect. While these studies certainly help understand the mechanism behind efficient spin polarization of the chiral system, a unifying model is still needed to explain the results more quantitively. Exploring chiral molecules with modulations in the helical pitch and/or diameter along with variations in functional groups remains an open area for further studies. A correlation between the spin polarization and these parameters should unravel some details about the effect and help build a unified model. Another area of interest is utilizing CISS effect to control spin during chemical reactions. Chapters 4 and 5 show how spin dependent charge transport through a chiral thin film facilitates spin dependent chemical reactions. Although proof of principle experiments have been underlined herein, an overall improvement in the chirality of the system under consideration and the effect of paramagnetic ions can further help validate the claims. This dissertation lays a solid groundwork enabling future advancements of the CISS effect and related phenomena.

APPENDIX A

A.1 SUPERPARAMAGNETIC IRON OXIDE NANOPARTICLE (SPION)PREPARATION

Two different types of SPIONs were used for measurements, achiral and chiral. The achiral SPIONs were prepared according to a previously published procedure.[1] More specifically, the nanoparticles were synthesized by adding a degassed solution of $Fe(CO)_5$ in 1-octadecene into a three-necked flask which contained a solution of 1-octadecene, dodecan-1,2-diol, oleyamine, and oleic acid at 250°C under N_2. Then, the mixture was cooled to room temperature in air and purified through precipitation using 2-propanol and acetone. The black solid was separated via centrifugation and dispersed in chloroform to obtain an optically clear, stable colloidal solution. The final achiral SPIONs, of 10 nm in size, were coated with a mixture of oleylamine, oleic acid and dodecan-1,2 diol ligands

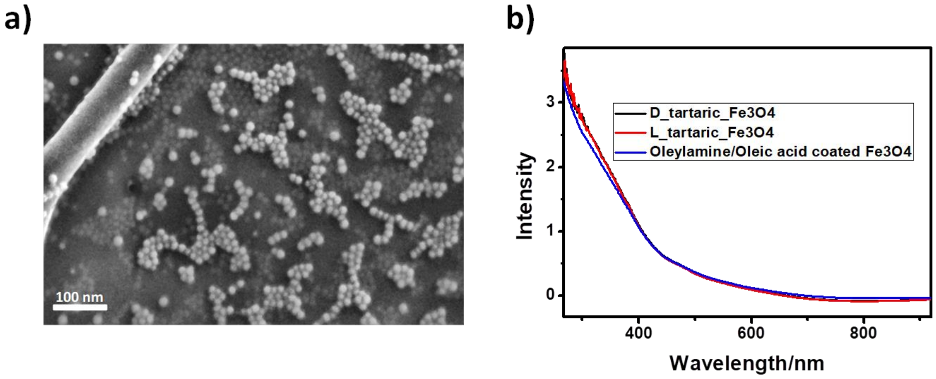

Figure A.1 (a) SEM images (Zeiss Sigma500 VP) of oleylamine/oleic acid coated SPION. (b) UV-Vis spectra of SPIONS. Note that the spectra are shifted upward by an arbitrary amount so that they can be distinguished from one another

Reference measurements were made using SPIONs coated in all directions with left- or right-handed chiral tartaric acid molecules. The chiral SPIONS were prepared by post synthesis ligand exchange of oleylamine/oleic acid coated iron oxide with tartaric acid. For the synthesis of the reference nanoparticles a previously published protocol was followed, based on the thermal decomposition of iron oleate in the presence of oleic acid and oleylamine(1:3).[2] The mixture was heated under argon at 200°C for 2 hours and then the temperature was increased to 300°C for 2 additional hours. The nanoparticles were purified through precipitation with ethanol and washed with hexane and ethanol (1:1 ratio). Figure A.1 shows an SEM image and the absorbance spectrum (Figure A.1b, blue line) of the synthesized particles. For the ligand exchange reaction, 5 mg of synthesized oleylamine/oleic acid iron oxide was dissolved in toluene and 20-30 mg of tartaric acid (dissolved in DMSO) was added. The mixture was vigorously stirred for 48 hours resulting in the formation of a precipitate which was washed with ethanol multiple times to remove excess ligands. Finally, the tartaric acid coated iron oxide nanoparticles were dispersed in pH 9 water.[3] A similar absorbance spectrum before (blue) and after (black, red) ligand exchange indicates that the integrity of the nanoparticles persists (Figure A.1b).

A.2 SAMPLE PREPARATION FOR MAGNETIC MEASUREMENTS

Two types of magnetic measurement techniques were used: SQUID and M-AFM. Preparation of the samples for both systems started by depositing 10 nm of Ti (adhesion layer), followed by 100 nm of Ag onto a Si wafer by evaporation. The Ag coated wafers were then diced into 4 mm x 4 mm chips.

Sample Preparation for SQUID: Samples were prepared under an inert (nitrogen) atmosphere. The chips were immersed in 11.25 M HCl solution (50% v/v) for 10 seconds to remove any native oxide layer formed on the Ag surface. Afterward, the samples were washed with distilled water and then dried with an N_2 gas flow. Additional cleaning was done by soaking the chips in absolute ethanol for 20 minutes and then drying with N_2 gas. For the formation of AHPA-SAMs, the samples were placed in a 1 mM L- (or D-) AHPA solution in ethanol and incubated for 3 hours. After adsorption, the samples were immediately washed in absolute ethanol to remove excess unbound AHPA molecules and dried with N_2. Lastly, a dilute 5 µL SPION chloroform solution was drop cast onto the sample surface and dried with an N_2 gas flow. The preparation of the L- AHPA X2 in which an additional L- AHPA-SAM was formed on top of the SPIONs layer included one additional step. In this case the sample was placed again in the 1 mM L- AHPA solution for 3 hours followed by washing with ethanol and drying with N_2 gas flow. Figure A.2 illustrates the main preparation stages of these samples.

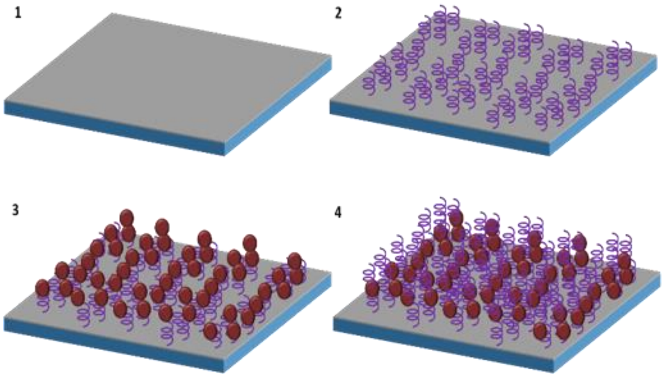

Figure A.2 Illustration of the preparation of the L- AHPA + SPIONs (achieved at stage 3) and the L- AHPA X2 + SPIONs reference sample (achieved at stage 4); 1- preparation of clean 4mm X 4mm Ag substrate, 2- formation of the AHPA-SAM (purple helical molecules), 3- adsorption of SPIONs (red spheres), 4- deposition of a top layer of AHPA molecules.

Sample Preparation for M-AFM: An additional lithography process was performed to pattern areas of the substrate with the AHPA SAM. Following the Ag layer evaporation, an optically active resist (AR-P 7400.23) was spin coated onto the sample. Line and square patterns were written in the resist using a Laser writer (LW405-A) and then developed. The adsorption procedure of the AHPA-SAM was carried out in the same fashion as the SQUID samples. After the formation of the AHPA-SAM, the resist was removed by immersing in acetone for 1 minute. Thus, the regions in which resist was present resulted in bare substrate with no SAM formation. Despite the lift-off process, some AHPA molecules re-adsorbed outside the AHPA-SAM areas, but with a much lower density. The SPIONs were then drop cast onto the chips (Figure A.2b outlines the steps in this procedure).

Additional reference samples of SPIONs covered with L- or D-tartaric acid were carried out in an analogous manner on a mica or plasma cleaned SiO_2 substrates. The mica substrate was cleaved three times to achieve a clean surface before drop casting a 5 µL solution of tartaric acid coated SPIONs and drying with a N_2 gas flow.

A.3 MEASUREMENT SYSTEMS

Superconductive quantum interference device (SQUID) measurements were done using MPMS3 LOT Quantum Design Inc. in vibrating sample magnetometry (VSM) mode to characterize the magnetization hysteresis loop of the SPIONs on the AHPA-SAM. The samples were mounted such that their surface was perpendicular to the direction of the magnetic field. The magnetic field was applied between -500 Oe to +500 Oe on a logarithmic scale to obtain higher resolution near zero field. The baseline was taken using a sample with only the Ag layer (no AHPA molecules or SPIONs). This substrate baseline was subtracted from all other measurements (Figure A.3).

M-AFM measurements were made using an AIST-NT SmartSPM^{TM} 1000 Scanning probe Microscope under ambient conditions with a cobalt alloy coated M-AFM tip (BudgetSensor MagneticMulti75-G, coercive field of ~300 Oe, K~2.8 N/m, F~75 KHz). A 5000 Oe magnetic field was applied with a home-made electromagnet to magnetize the tip either normal (up) or anti-normal (down) to the substrate. Interleaved topography and magnetic interaction images were taken. The topography was measured in tapping mode at an average tip distance of ~30 nm from the sample, while the magnetic interaction was measured at an additional height of 100 nm (a total distance of ~130 nm) to avoid Van der Waals interactions that can influence the measurements. The magnetic interaction image measures the relative phase of the oscillating tip; a positive phase (brighter spots) indicates a repulsive interaction between the tip and the surface and a negative phase (darker spots) indicates an attractive interaction. Additional measurements on the all covered SPIONs were also conducted on an Agilent 5500 scanning probe microscope with a Co-Cr magnetic tip (coercive field of ~400 Oe, K~3 N/m, F~75 KHz). The magnetic phase signal is measured in a interleave scan mode with a interleave pull away distance of 100 nm.

Transmission electron microscopy investigation of the achiral SPIONs was accomplished by a Joel Jem-1011 microscope operating at an accelerating voltage of 100 kV and equipped with a W source and a Quemesa Olympus CCD 11 Mp Camera for the image acquisition. The SPIONs dispersion was deposited on a 300 mesh amorphous carbon coated Cu grid by dipping. Freeware imageJ analysis program was used to determine the size of the nanoparticles.

For the achiral SPIONs on patterned AHPA-SAM, SEM images (Figure 2.2) were taken on a Magellan^{TM} 400L XHR-SEM instrument under 2.0 kV accelerating voltage, 13 pA current, at a 1.9 mm working distance and using a TLD detector in secondary electrons mode.

For the chiral SPIONs, SEM images (Figure A.1) were taken on a ZEISS Sigma500 VP instrument at a 3.0 kV accelerating voltage and 2.4 mm working distance using an InLens Duo detector. The samples were deposited on a lacy carbon copper grid through four sequential soaking / drying stages in a dilute iron oxide solution.

A.4 ADDITIONAL RESULTS

Figure A.3 shows the magnetic hysteresis loop measurement of clean Ag surface. In which the Ag diamagnetic baseline response is achieved and was subtracted from all other magnetic hysteresis loop measurements.

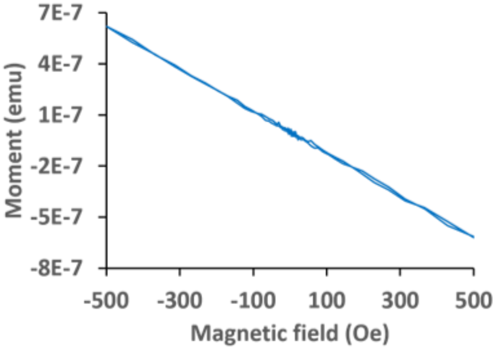

Figure A.3 Diamagnetism baseline measurement of clean Ag which was subtracted from all other magnetization hysteresis loop measurements**.**

Figure A.4 presents magnetic interaction measurements of individual SPIONs on L-AHPA. This picture was taken from the same samples measured in Figure 2.4 using areas with sparse SPIONs adsorption. As in the dense SPION adsorption (Figure 2.4) a repulsive interaction is observed for downward magnetization of the M-AFM tip (Panel a) and an attractive interaction is observed for upward magnetization of the M-AFM tip (Panel b)

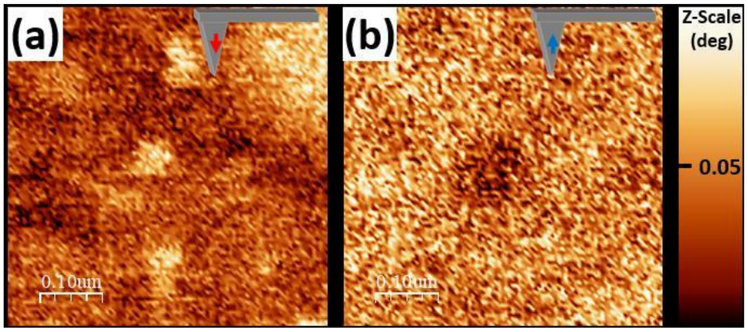

Figure A.4 Magnetic Interaction measurements of individual SPIONs on L-AHPA. Panel (a) shows repulsive interaction for downward magnetization of the M-AFM tip (red arrow) and Panel (b) shows attractive interaction for upward magnetization of the M-AFM tip.

Figure A.5 panels a) and b) shows an enlargement of the topography images and cross sections of only SPIONs on Ag sample presented in the insets of figure 5 panels b) and c) respectively. The cross sections show that the nano objects on the surface are of ~10 nm average height, in agreement with the size of the SPIONs measured by TEM, indicating the presence of monolayers of SPIONs on the surface.

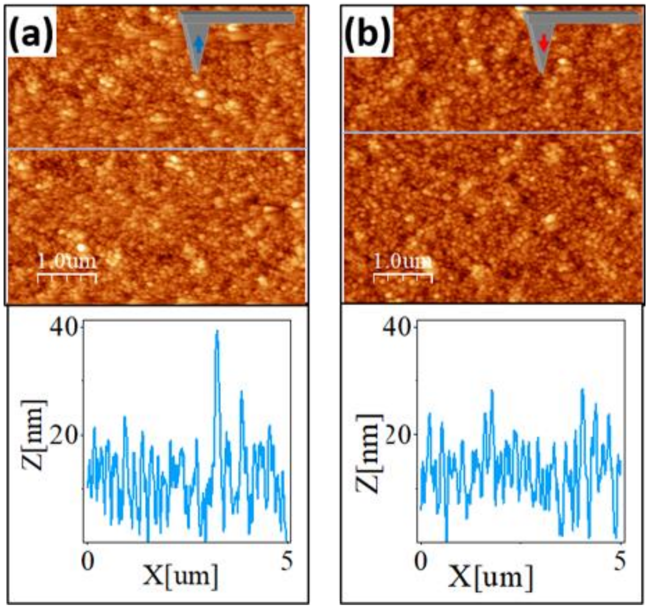

Figure A.5 Panels a) and b) are the enlarged topography images of the sample of only SPIONs on Ag substrate presented in Figure 5 b&c repectively. Cross sections were taken on each of the images to show that the objects on the substrate are of ~10 nm averaged height which correspond to the size of the SPIONs.

Figure A.6 shows the magnetic phase shift of the L- and D-tartaric acid coated iron oxide nanoparticles. The coating is covering the nanoparticles from all directions. The magnetic phase shift value was taken from M-AFM measurements on single nanoparticles. A distribution of magnetic phase shift per unit volume against the size of the nanoparticles is plotted in Figure A.5 panels a) and b). The black symbols are for measurements in which the tip was magnetized in the north direction (N) and the red symbols are for measurements in which the tip was magnetized in the south direction (S). Histograms of the magnetic phase shift are presented for both chiralities and magnetizations in Figure A.5 panels c) and d). The overlapping distribution of the phase shift for north and south pole tip magnetization indicates that no clear MIPAC effect is evident. This behavior is attributed to a frustrated magnetic dipole in the iron oxide nanoparticles, as are the SPIONS in the L- AHPA X2 + SPIONs sample (Figure 2.3b). While the majority of the data indicates random orientations, the tail of the histograms indicates that some asymmetry exists. The origin of this effect may arise from asymmetric surface coverage of the nanoparticles, which creates a principal axis to stabilize the frustrated magnetic dipole.

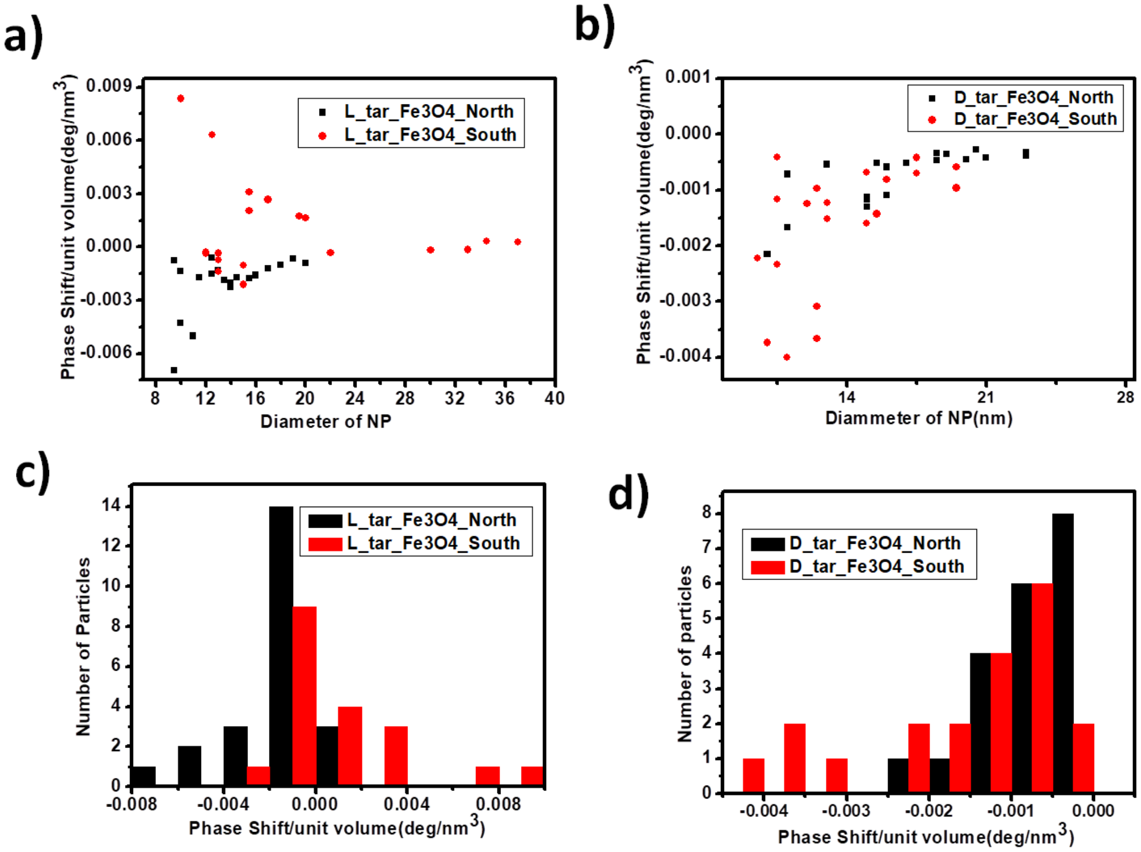

Figure A.6 Panels a) and b) show the magnetic phase shift signal per unit volume against the diameter of the nanoparticle for L-tartaric acid coated iron oxide (a) and D-tartaric acid coated iron oxide nanoparticles (b). N and S represent north and south pole magnetization of the AFM tip, respectively. Panel c) and d) show a corresponding histogram of the phase shift signal per unit volume for L- and D-tartaric acid coated iron oxide nanoparticless respectively.

A.5 REFERENCES

1.Depalo, N.; Carrieri, P.; Comparelli, R.; Striccoli, M.; Agostiano, A.; Bertinetti, L.; Innocenti, C.; Sangregorio, C.; Curri, M. L., Biofunctionalization of Anisotropic Nanocrystalline Semiconductor–Magnetic Heterostructures. *Langmuir* **2011,** *27* (11), 6962-6970.

2.Xu, Z.; Hou, Y.; Sun, S., Magnetic Core/Shell Fe3O4/Au and Fe3O4/Au/Ag Nanoparticles with Tunable Plasmonic Properties. *Journal of the American Chemical Society* **2007,** *129* (28), 8698-8699.

3.Calero, M.; Gutiérrez, L.; Salas, G.; Luengo, Y.; Lázaro, A.; Acedo, P.; Morales, M. P.; Miranda, R.; Villanueva, A., Efficient and safe internalization of magnetic iron oxide nanoparticles: Two fundamental requirements for biomedical applications. *Nanomedicine: Nanotechnology, Biology and Medicine* **2014,** *10* (4), 733-743.

APPENDIX B

B.1 SAMPLE PREPARATION

Different types of magnetic samples were used for the KPFM measurements; however, all of the experiments showed similar magnetization trends. For the experiment illustrated in Figure 3.1 in the main text ITO substrate were coated with 3 nm of Ti buffer layer, followed by 10 nm of polycrystalline Ni, and 10 nm of Au using a Plassys evaporator. For the experiments describe in Figure 3.4 e-beam evaporation of Ti/Ni/Au-10nm/120nm/10nm on Si-100 was used as the substrate

Epitaxial thin films with cobalt ferromagnetic layer were used in all figures 3.2 and 3.3. The films were grown using PREVAC molecular beam epitaxy method (MBE) with base pressure 10^{-10} Torr, according to the following configuration Al_2O_3 (0001)/Pt (5 nm)/Au (20 nm)/Co (1.5nm)/Au (5 nm). A Pt buffer layer was deposited at 650 °C to ensure an atomically flat buffer layer surface allowing the epitaxial growth of consecutive layers. Sharp streaks were visible in the in-situ obtained RHEED images for each growth step. The crystallographic orientation of the epitaxially grown layers was as follows: Pt(111), Au(111), Co(0001), and Au(111). The Pt buffer and Co layers were deposited using an electron gun; Au layers were deposited from high temperature effusion cells. Sample with the flat uniform Co thickness of 1.5 nm has a perpendicular anisotropy, featured rectangular hysteresis loop for a magnetic field direction perpendicular to the plane, which is characteristic of the out-of-plane easy axis. Wedge type samples were also studied and they were deposited using a movable shutter controlled by a step motor. Two types of wedge samples were also grown - Au wedge and Co wedge.

- Al_2O_3 (0001)/Pt (5 nm)/Au (20 nm)/Co (1.5nm)/Au wedge (2-10 nm)

  Al_2O_3 (0001)/Pt (5 nm)/Au (20 nm)/Co (1.6 -3 nm)/Au (5 nm),

For Co layer thickness above 2 nm the spin reorientation transition occurs, magnetization easy axis changes from perpendicular to in-plane direction, resulting in the in-plane anisotropy. Hysteresis loops were measured by the polar magneto-optic Kerr effect (P-MOKE) along the Co wedge direction and by SQUID, for the sample with flat Co layer (see Figure B.1).

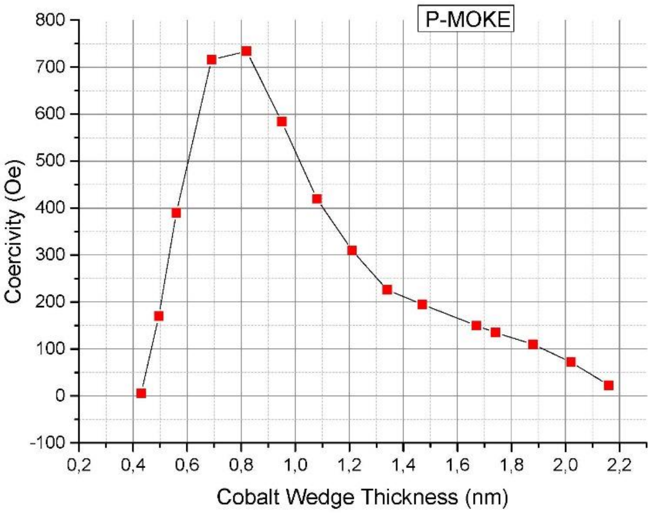

Figure B.1 Coercivity dependence on the thickness of the cobalt layer for epitaxial Au/Co/Au substrates. Co was deposited as a wedge using a computer controlled movable shutter.

The standard, phenomenological relation based on Neel predictions $K_{1\mathrm{eff}}(d) = -2\pi Ms^2 s + K1v + 2K1s/d$, where d denotes thin film thickness and Ms a saturation magnetization, is used for anisotropy description in thin films, containing the demagnetization term (shape anisotropy) and two anisotropy terms: volume $K1v$ and mean surface $K1s$ originating from the interfaces with buffer and over layer. As the K1s is inversely proportional to the thin film thickness *d* for higher value of d a SRT (Spin Reorientation Transition) takes place and the easy axis direction rotates from perpendicular to in-plane direction.

B.2 KPFM MEASUREMENT

KPFM measurements were made using an Asylum Research MFP-3D atomic force microscope. Experiments were done under ambient conditions in a nitrogen atmosphere. Electric cantilevers, ELEC-01 silicon chip with a Titanium/Iridium coating (K~2.8 N/m, F~75 KHz) from Asylum Research, were used to conduct the experiments. The surface potential measurements were performed at a 20 nm distance from the surface. Because of the dielectric nature of the monolayers, the sample was not grounded. For the magnetic field experiments, a permanent magnet was placed underneath the substrate such that ~ 200 mT magnetic field (measured using a Gauss meter) was applied to the substrate. Because the measurements are susceptible to environmental conditions and dust, the acquired data are only used for measurements with reproducible KPFM scans. Figure B.2 shows an example of a topography and KPFM image for one of the samples.

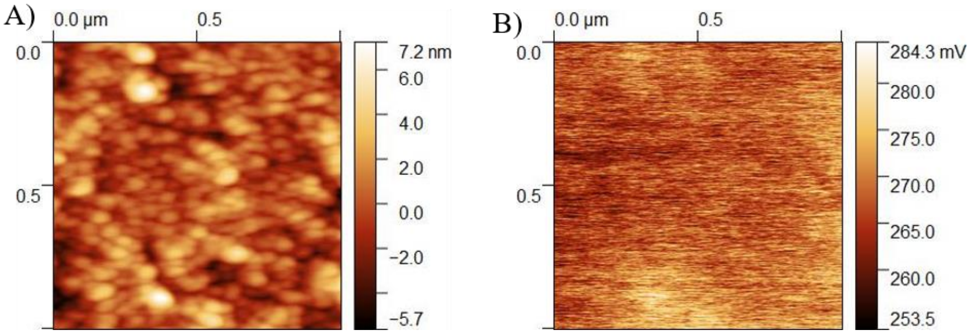

Figure B.2 The left panel shows a representative topographic image corresponding to an L-Ala5 coated ferromagnetic Ni substrate. The right panel image shows an electrostatic potential map corresponding to the image in the left panel

B.3 PEPTIDE SAM PREPARATION

Measurements were performed on two different peptides (D and L-HS-CH_2-CH_2-(Ala-Aib)$_5$-COOH) and an achiral molecule (HS-(CH_2)$_{15}$-COOH). The D- and L-peptides were synthesized by Genemed Synthesis, Inc. and the achiral molecules were purchased from Sigma Aldrich.

To prepare the SAM, the substrates were first cleaned by immersing them in absolute ethanol for 10 minutes and then drying them under a stream of argon gas. The substrates were then incubated in a 1mM peptide / achiral molecule ethanoic solution for 48 hours. After adsorption, the samples were washed in absolute ethanol to remove excess unbound molecules and dried with argon. All of the substrates were stored under vacuum prior to KPFM measurements.

B.4 PEPTIDE MACROSCOPIC CPD MEASUREMENT

The CPD of the surfaces was determined using a commercial Kelvin probe instrument (Delta Phi Besocke, Jülich, Germany) within a Faraday cage at atmospheric pressure. The reference probe consisted of a gold grid. The CPD signal was allowed to stabilize before recording, where ΔCPD is the difference in the direction of magnetic field.

Substrate Preparation and Cleaning*:* Substrates used for the CPD measurement are grown by e-beam (ODEM evaporator) where Si-100 wafer used as a substrate to grow Ti/Ni/Au- 10 nm/120 nm/10 nm with 0.5 Ǻ/sec deposition rate at 10^{-8} Torr pressure The surfaces were cleaned by first boiling in acetone and then boiling in ethanol for 10 minute each. The surfaces then underwent UV-Ozone treatment for 10 minutes and then subsequently immersed in ethanol for 30 minutes. Immediately afterwards, the substrates were dried with a nitrogen stream and then used for monolayer deposition.

DNA SAM Preparation*:* The self-assembled monolayers (SAM) of DNA were prepared using DNA oligomers 3'- functionalized with thiol groups on one strand. DNA duplexes were used for monolayer preparation and spin polarization studies in the following way: First, a 100 µM stock solution of DNA was prepared in deionized water. Before monolayer preparation, the stock solution was mixed with 0.8 M PBS (K_2HPO_4/KH_2PO_4) buffer (pH = 7.2) in equal quantity – thus making a 50 µM DNA solution in 0.4 M PBS buffer. The solution was then mixed with the same quantity of 10 mM Tris(2-carboxyethyl)phosphine hydrochloride (TCEP, purchased from Sigma Aldrich) in 0.4 M PBS buffer (pH 7.2). The solution was left in Tris buffer for 2 hours, then was purified by filtering through a Micro Bio-Spin P-30 column (purchased from Bio Rad). The final concentrations of all DNA were measured with UV-vis spectroscopy using a Nanodrop spectrometer and was found to be between 20-30 µM. This DNA solution was drop cast onto the substrate The sample was left for 20 to 24 hours in humid environment and then rinsed twice with 0.4 M PBS and twice in deionized water.

DNA Sequence*:*
20bp dsDNA:
5'-CGC TTC GCT TCG CTT CGC TT/3ThioMC3-D/-3'
5'-AAG CGA AGC GAA GCG AAG CG-3'
30bp dsDNA:
5'-CGC TTC GCT TCG CTT CGC TTC GCT TCG CTT/3ThioMC3-D/-3'
5'-AAG CGA AGC GAA GCG AAG CGA AGC GAA GCG-3'
40bp dsDNA:
5'-CGC TTC GCT TCG CTT CGC TTC GCT TCG CTT CGC TTC GCT T/3ThioMC3-D/-3'
5'-AAG CGA AGC GAA GCG AAG CGA AGC GAA GCG AAG CGA AGC G-3'

50bp dsDNA:
5’-CGC TTC GCT TCG CTT CGC TTC GCT TCG CTT CGC TTC GCT TCG CTT CGC TTC GCT TCG CTT CGC TT/3ThioMC3-D/-3’
5’-AAG CGA AGC GAA GCG AAG CGA AGC GAA GCG AAG CGA AGC GAA GCG AAG CG-3’

Oligopeptide SAM Preparation*:* For growing monolayers of oligopeptide, the substrates were prepared using the same cleaning procedure as that used for DNA. Following cleaning in a peptide solution (0.625 mg mL^{-1}, using a 1:1 mixture of pH 7.0, 10 mm sodium phosphate buffer and TFE). The substrate was incubated for 36 hours and then rinsed twice with de-ionized water

Oligopeptide Sequence**:**

$SHCH_2CH_2CO$-(Ala-Aib)$_3$-COOH

$SHCH_2CH_2CO$-(Ala-Aib)$_4$-COOH

$SHCH_2CH_2CO$-(Ala-Aib)$_5$-COOH

$SHCH_2CH_2CO$-(Ala-Aib)$_6$-COOH

$SHCH_2CH_2CO$-(Ala-Aib)$_7$-COOH

APPENDIX C

C.1 X-ray DIFFRACTION (XRD)

Powder XRD patterns were collected using a Bruker AXS D8 Discover XRD (NanoScale Fabrication and Characterization Facility, Petersen Institute of NanoScience and Engineering, Pittsburgh, PA) equipped with a Cu Kα (λα = 1.5406 Å) X-ray source operating at 40 kV and 40 mA. The diffracted beam was detected using a Bruker AXS Lynxeye (silicon strip) detector. PXRD patterns were collected using a continuous lock-coupled scan with a scan speed of 0.25 s/step from 15.00 to 95.00° with a step size of 0.025°

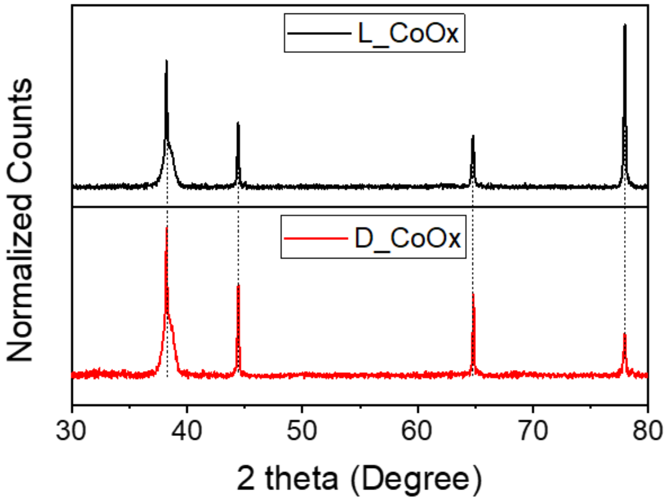

Figure C.1 XRD specta of L- (black, top) and D-(red, bottom) chiral cobalt oxide thin films.

C.2 X-ray PHOTOELECTRON SPECTROSCOPY

XPS data were collected on an ESCALAB 250XI instrument. The data were referenced to an adventitious carbon peak of 284.8 eV and measured before and after a soft ion sputter cleaning (1000 eV for 10 s) to ensure that the treatment was not changing the oxidation state of the metal oxide. The data were collected while using a flood gun to compensate for surface charging. Each spectrum represents the average of 20 scans.

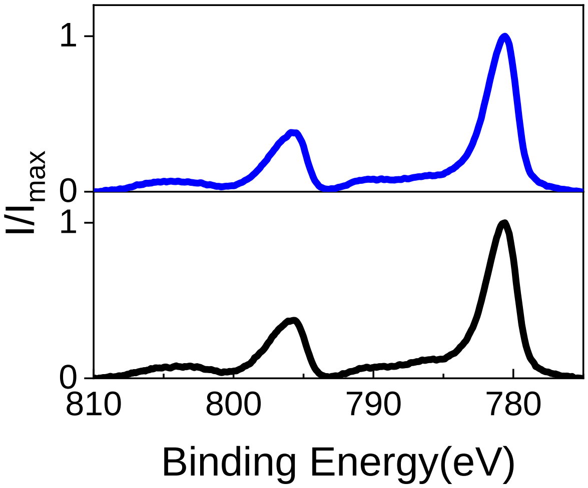

Figure C.2 XPS spectra of L-(black) and meso-CoOx (blue)

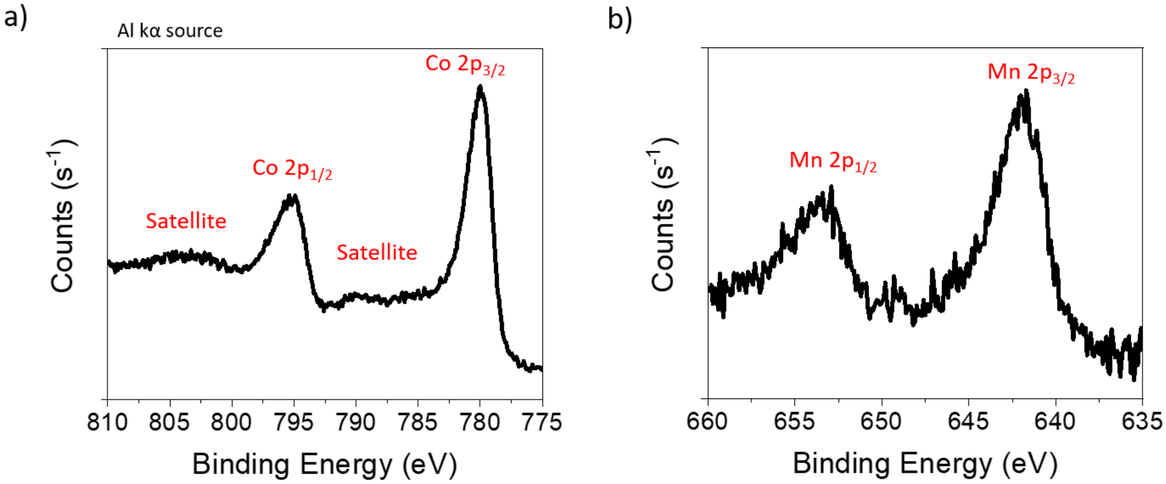

Figure C.3 XPS PS spectra of 5 % Mn doped L-CoOx thin film in the in the Co2p$_{3/2}$ region (Panel a) and in the Mn2p3/2 region (panel b).

APPENDIX D

D.1 THICKNESS DETERMINATION

Figure D.1 shows a thickness calibration plot of L-CoO$_x$ thin films using profilometry and UV-Vis spectroscopy. The thickness of the film was modified through the deposition time. The relationship between thickness and absorptivity at 368 nm was fit to an exponential function (red line). The same thickness dependence with deposition time was observed for meso-CoOx.

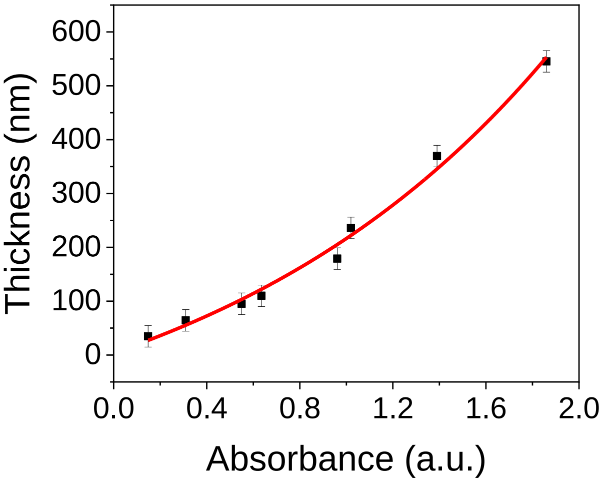

Figure D.1 Calibration plot showing the change in thickness of L-CoOx thin films measured using a profilometer to a change in absorbance. The change in thickness was achieved by changing the duration of the electrodeposition.

D.2 XPS CHARACTERIZATION

Figure D.2 shows X-ray photoelectron spectra (panel a) and difference spectra (panel b) in the Co2p$_{3/2}$ region for L-CoO$_x$ (black), meso-(CoO$_x$) (blue), and L-CoO$_x$ after treatment at 1.2 V vs NHE (orange). The data in panel a) are offset for clarity. For the difference spectra the data were first normalized to the Co2p$_{3/2}$ peak before subtraction. The satellite structure plotted between 782 -794 eV is reflective of the valence state of the cobalt in the catalysts.

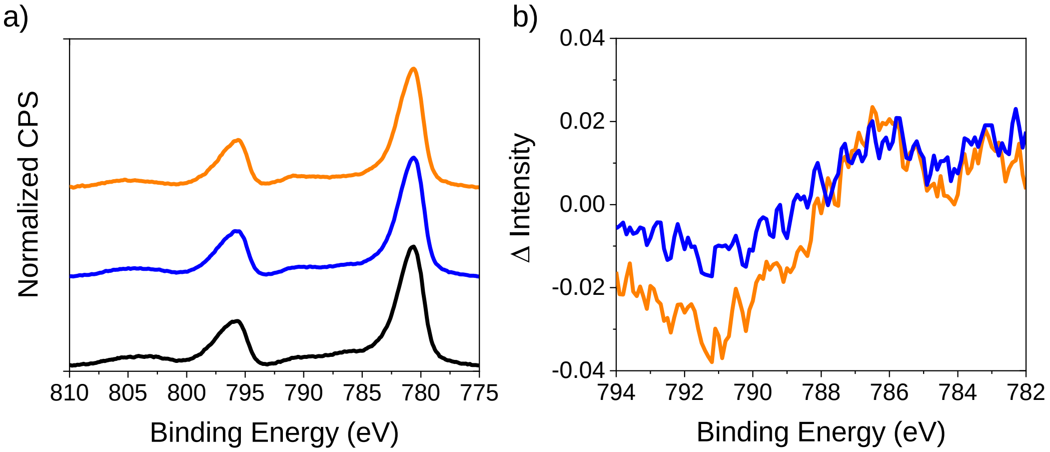

Figure D.2 Panel a) shows thin film XPS data of L-CoO$_x$ (black), Meso-CoO$_x$ (blue), and L-CoO$_x$ after the application of 1.2 V vs NHE in 0.1M KOH for 30 min (orange). Panel b) shows difference spectra in the satellite region between L-CoO$_x$ and Meso-CoO$_x$ (blue) and L-CoO$_x$ and the same film after the application of 1.2 V vs NHE in 0.1M KOH for 30 min (orange). The data were normalized to the Co2p$_{3/2}$ peak.

Figure D.3 shows XPS spectra and corresponding fitting of L-CoO$_x$ (A), meso-CoO$_x$ (B), and L-CoO$_x$ after treating the film at 1.2 V vs NHE in 0.1 M KOH for 30 min (Mag-CoO$_x$). The Co 2p$_{3/2}$ and 2p$_{1/2}$ peak maximum splitting is ~15 eV in all three samples and is consistent with the presence of Co_3O_4.[1] Conversely, the O1s spectrum is fit to a sum of 4 peaks and is consistent with reports indicating that cobalt is bound to both oxides (blue peak) and hydroxides (orange peak); see Figure D 4.[2] This may indicate that one, or both, of $Co(OH)_2$ and CoOOH are present. Because of the overlapping behavior of the different cobalt oxide/hydroxide peaks, stoichiometric quantification of these catalyst components is not possible. Instead, the cobalt XPS data is fit to a sum of five peaks and only the differences between the catalyst peak intensity, specifically in the sattelite region, are considered. The fitting parameters are shown in Table D.1.While the peak position can change with the type of oxide/hydroxide, the majority of the peak contribution for the satellite structures at ~786 eV and ~790 eV are attributed to Co(II) and Co(III), respectively.[1, 2]

The data are quite similar between L- and meso-CoO$_x$; only slight differences in the ratio of the purple:organge satellite peaks occur. Conversely, a modest change arises upon treating the film at 1.2 V, the orange sattelite peak becomes somewhat more intense than the the purple satelite peak. We attribute this change to a decrease in Co(II) content and the formation of CoO_2 based on a Pourbaix analysis at the applied potential and the magnetic properties that manifest. While the Pourbaix diagram also indicates the possible formation of CoOOH, SQUID measurements performed by other groups indicate that the Co(III) in this material is diamagnetic[3] and thus, magnetic field effects are not expected. A magnetic field response can arise from the tetrahedral Co(II) , however it is unlikely that more Co(II) is formed upon treating the film at oxidizing potentials; evidenced by the decrease in intensity of the sattellite peak (purple).

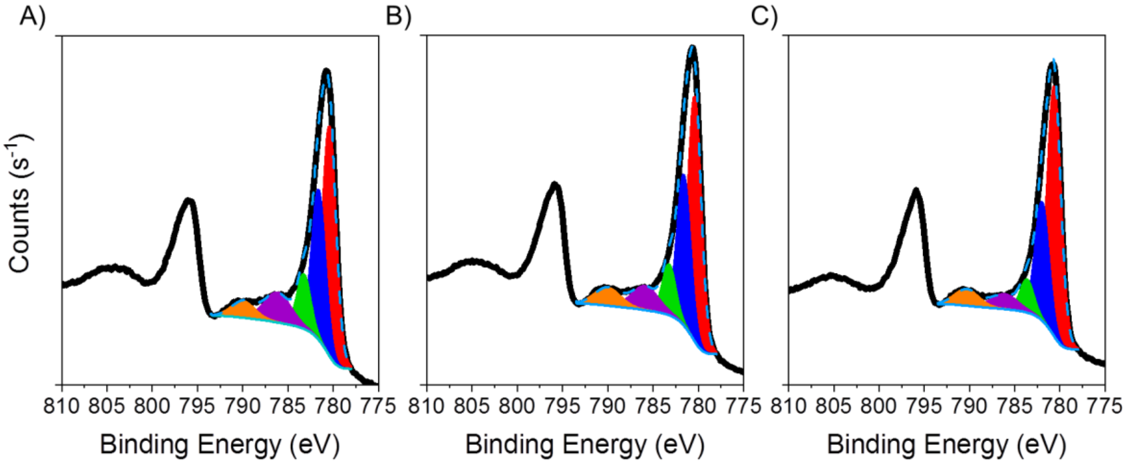

Figure D.3 shows XPS spectra of L-CoO$_x$ (A), meso-CoO$_x$ (B), and L-CoO$_x$ after treating the film at 1.2 V vs NHE in 0.1 M KOH for 30 min (Mag-CoO$_x$). Each spectrum was fit to a sum of 5 peaks and the envelope is plotted as a blue-dashed line.

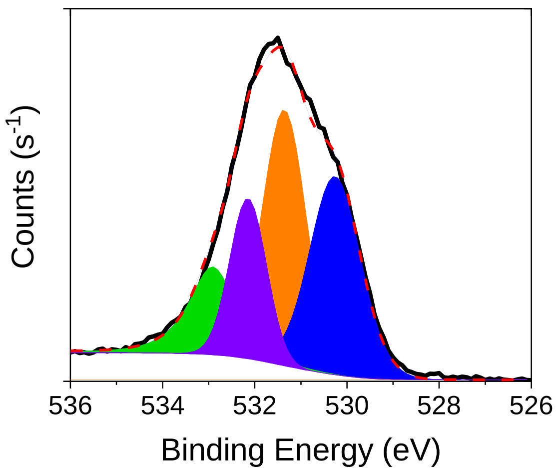

Figure D.4 O1s XPS spectra of an L-CoO_x catalyst. The blue and orange peaks are consistent with reports (see reference 3) indicating cobalt-oxide and cobalt-hydroxide contributions, respectively.

Table D.1 Fitting parameters for the XPS spectra shown in Figure D.4. The peak positions were contrained to have the same binding energy in L-CoOx and meso-CoOx whereas for the treated sample only the orange and purple peaks could be constrained to give a quality fit.

	L-CoO_x		meso-CoO_x		Treated	
	BE (eV)	AP (%)	BE (eV)	AP (%)	BE (eV)	AP (%)
Red	780.41	43.92	780.41	46.34	780.65	55.16
Blue	781.62	28.71	781.62	28.43	782.02	25.46
Green	783.25	10.45	783.25	9.95	783.74	7.33
Purple	786.15	11.35	786.15	9.02	786.15	5.03
Orange	789.96	5.58	789.96	6.27	789.96	7.01

The change in composition of the L-CoO_x catalyst after 210 min of water splitting at 5 mA / cm^2 is shown by Figure D.5 (before (black) and after (green)). The loss of the satellite feature at ~786 eV, presumably from oxidation, is consistent with a decrease in Co(II) content. Conversion of the catalyst during electrolysis for CoO_x is common,[4] however the implication for chiral effects upon transformation in OER remains unclear. It is important to note that some chiral effects must persist to account for the large differences in the Faradaic efficiency reported using Hoffman apparatus measurements (Figure 4.4).

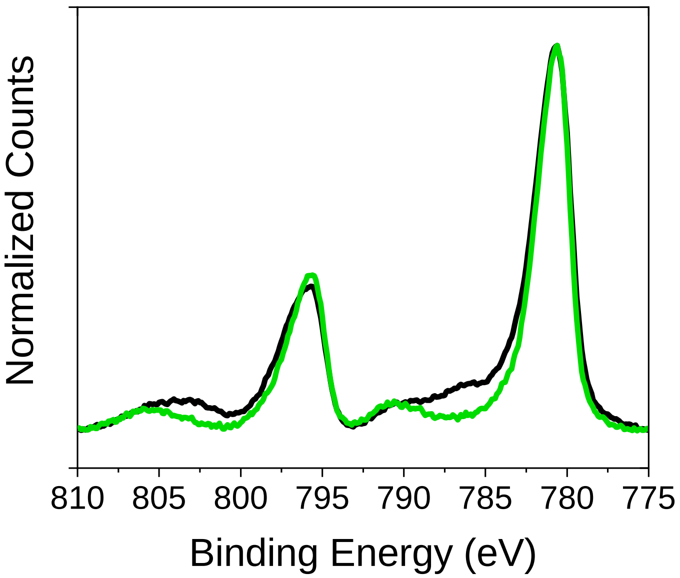

Figure D.5 XPS spectra of L-CoO$_x$ before (black) and after (green) electrolysis at 5 mA / cm^2 for 210 min.

D.3 ELECTROCHEMICAL SURFACE AREA

Figure D.6 shows the electrochemical surface area determination on L-CoO$_x$ (a) and meso-CoO$_x$ (b) thin films, respectively. Voltammograms were collected at different scan rates (0.05 - 3.2 V/s) in a 1 M NaOH water solution and the change in the non-Faradaic current of the cathodic (absolute value) and anodic wave at -0.4V is plotted as a function of scan rate, panel c. A linear fit to the data gives a slope of 9.9 μF for L-CoO$_x$ (black) and 10.2 μF meso-CoO$_x$ (blue), which implies that the two films (chiral and achiral) have similar electrochemical surface areas.

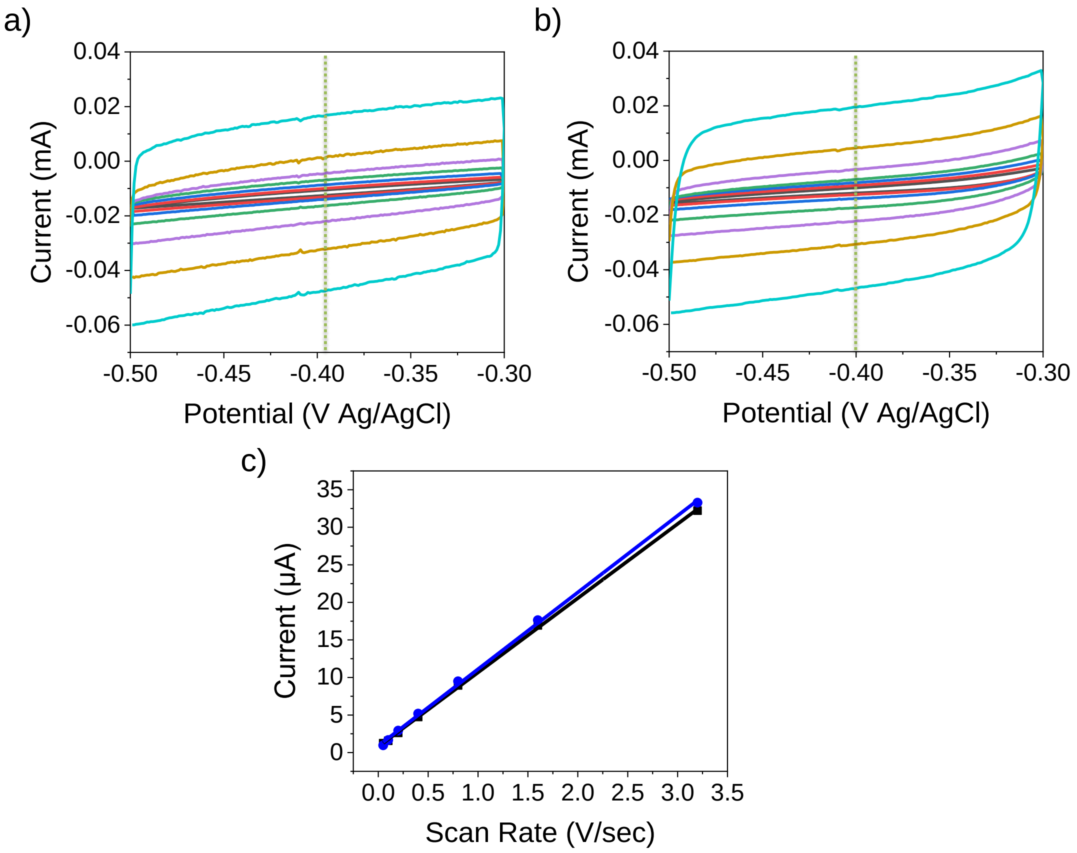

Figure D.6 Double layer capacitance measurements. Panel a) and b) show voltammograms of L-CoOx and meso-CoOx, respectively. Experiments were performed at different scan rates (0.05- 3.2 V) in 1 M NaOH. Panel c) shows the change in current (at -0.4 V) as a function of scan rate for L-CoOx(black) and meso-CoOx(blue). The slope of the line is proportional to C_{DL}.

D.4 ATOMIC FORCE MICROSCOPY

Atomic force microscopy measurements were done on L and meso cobalt oxides films deposited on FTO substrates. Figure D.7 show the surface topography and roughness of the film. A very similar roughness (± 30nm) is observed for L- and meso CoO_x films.

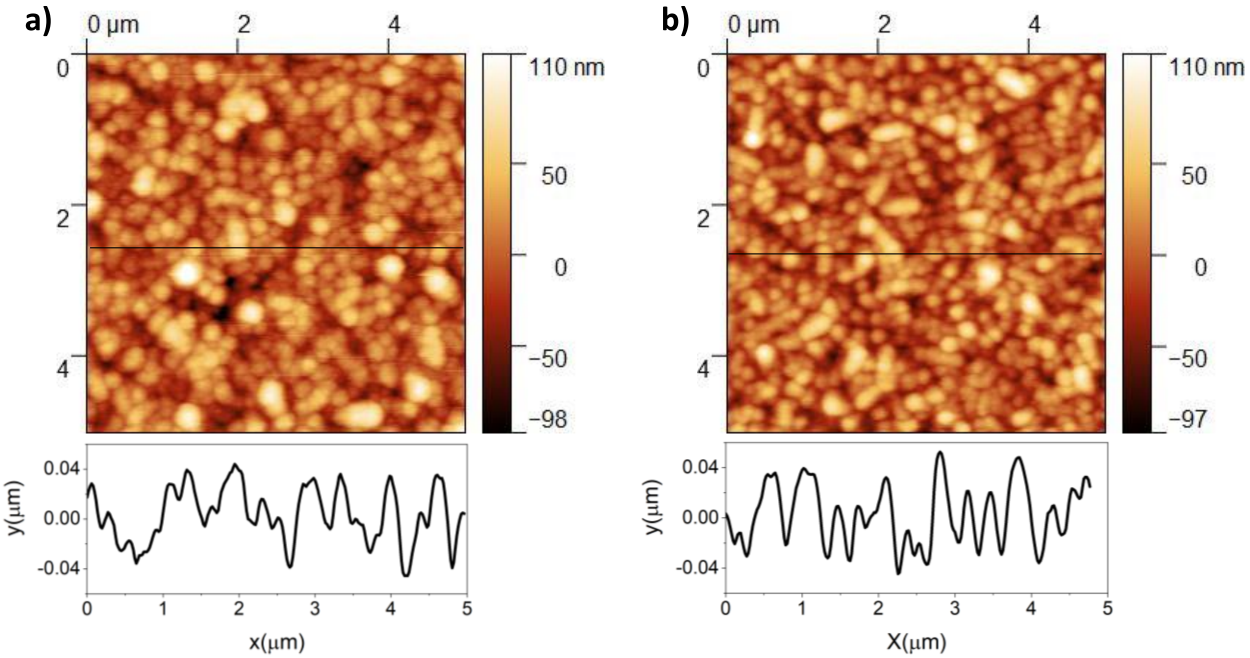

Figure D.7 Surface topography of a) L-CoOx film and b) meso CoO_x film. Corresponding roughness of the films were also shown by drawing a line on the topography images (below image).

D.5 TAFEL ANALYSIS

Figure D.8 shows Tafel plots for L- (black) and meso-CoO_x (blue) measured in 0.1M KOH solutions. A linear fit to the data are represented by a red dashed line. The Tafel plot relates the amount of overpotential required to increase the current density by a factor of 10.

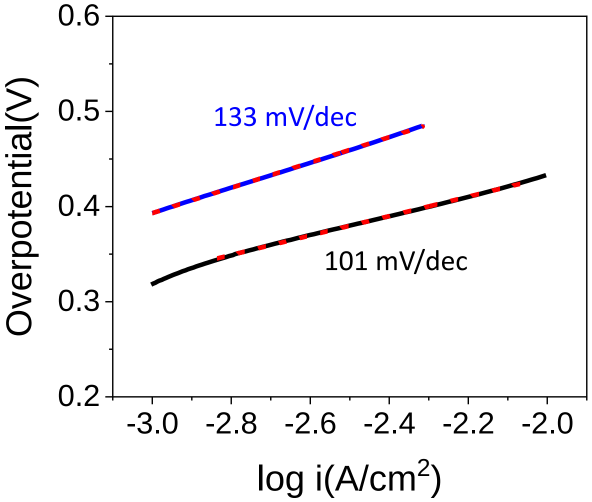

Figure D.8 Tafel plots of L- (black) and meso-CoO$_x$ (blue) thin film catatalysts measured in 0.1 M KOH solutions. The dashed red line is a linear fit to the data.

D.6 OER WITH D-CoO$_x$

Figure D.9 show the linear sweep voltammograms of thin film D-CoO$_x$(red) along with meso-CoO$_x$ (blue) catatalysts measured in 0.1 M KOH solutions. The D-CoO$_x$ film was prepared using the same condition as L-CoO$_x$ (see methods). The enhancement in OER is for D-CoO$_x$ over meso-CoO$_x$ is consistent with that shown for L-CoO$_x$.

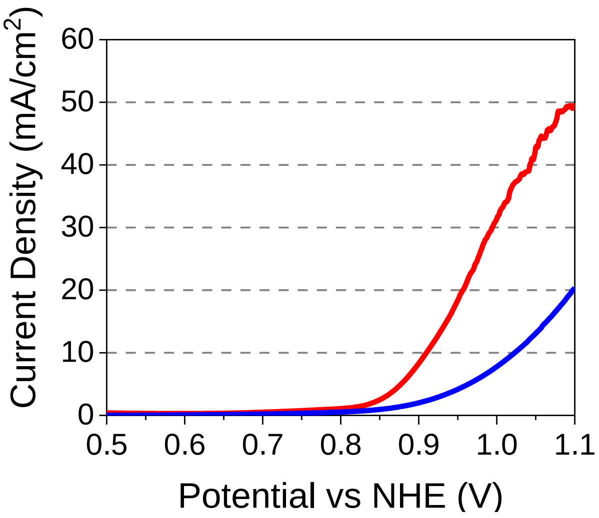

Figure D.9 shows linear sweep voltammograms for the OER using D-CoO$_x$ (red) and meso-CoO$_x$ (blue) in 0.1M KOH

Table D.2 Comparison of OER at 5 mA/cm2 for L-CoOx, D-CoOx and meso CoOx films

Metal Oxide	L-CoOx	D-CoOx	meso-CoOx
Potential vs NHE	427±32	436±18	489±47

Table D.2 shows the average potential vs NHE of at least 5 measurements in which a current density of 5 mA/cm2 is achieved in 0.1 M KOH for L-, D-, and meso-CoOx films

D.7 CHARACTERIZATION OF MAGNETIZED ELECTRODE

Figure D.10. shows absorbance (a) and circular dichroism (b) spectra of L-CoO$_x$ (black) and L-CoO$_x$ after being treated at 1.2 V vs NHE for 30 min (orange). The change in absorbance and decrease in circular dichroism response correlates to a change in the oxidation state of the thin film.

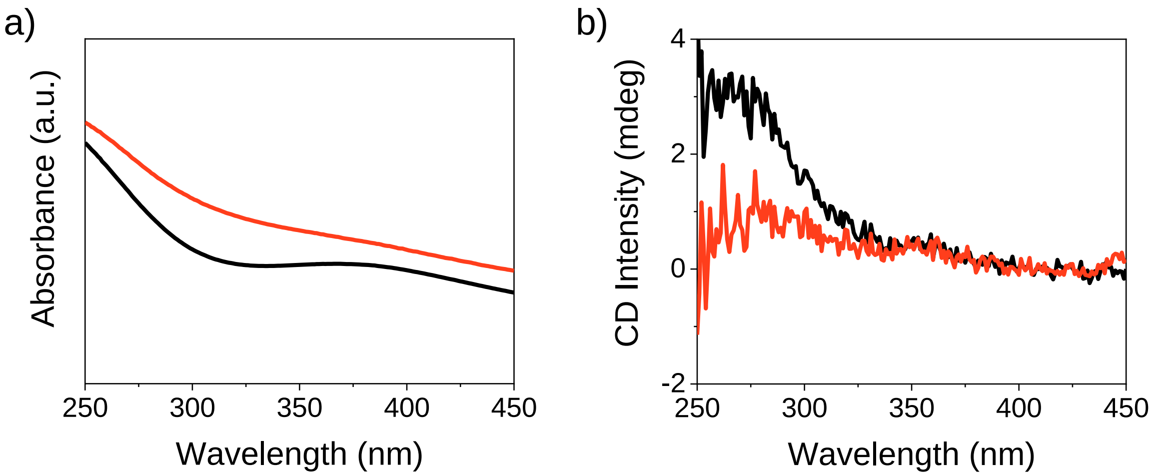

Figure D.10 Absorbance (a) and circular dichroism spectra (b) of L-CoO_x thin films before (black) and after (orange) treatment of 1.2 V vs NHE in 0.1M KOH for 30 min.

Figure D.11. shows linear sweep voltammograms for a treated CoO_x thin film with application of a North (red, dashed-line) and South (blue, solid-line) external magnetic field. Despite the thin film still exhibiting chiroptical properties, a difference in overpotential between the external magnetization was not observed.

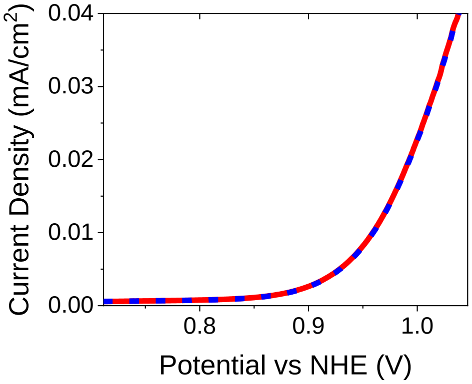

Figure D.11 Linear sweep voltammograms of treated CoO_x thin film with applied external magnetic field pointing north (red) and south (blue dash).

D.8 REFERENCES

1.Biesinger, M. C.; Payne, B. P.; Grosvenor, A. P.; Lau, L. W. M.; Gerson, A. R.; Smart, R. S. C., Resolving surface chemical states in XPS analysis of first row transition metals, oxides and hydroxides: Cr, Mn, Fe, Co and Ni. *Applied Surface Science* **2011,** *257* (7), 2717-2730.

2.Yang, J.; Liu, H.; Martens, W. N.; Frost, R. L., Synthesis and Characterization of Cobalt Hydroxide, Cobalt Oxyhydroxide, and Cobalt Oxide Nanodiscs. *The Journal of Physical Chemistry C* **2010,** *114* (1), 111-119.

3.Kudielka, A.; Bette, S.; Dinnebier, R. E.; Abeykoon, M.; Pietzonka, C.; Harbrecht, B., Variability of composition and structural disorder of nanocrystalline CoOOH materials. *Journal of Materials Chemistry C* **2017,** *5* (11), 2899-2909.

4.Bergmann, A.; Jones, T. E.; Martinez Moreno, E.; Teschner, D.; Chernev, P.; Gliech, M.; Reier, T.; Dau, H.; Strasser, P., Unified structural motifs of the catalytically active state of Co(oxyhydr)oxides during the electrochemical oxygen evolution reaction. *Nature Catalysis* **2018,** *1* (9), 711-719.

APPENDIX E LIST OF PUBLICATIONS

At University of Pittsburgh

1. Ghosh, S.; Bloom, B. P.; Lu, Y.; Lamont, D.; Waldeck, D. H., Increasing the Efficiency of Water Splitting through Spin Polarization Using Cobalt Oxide Thin Film Catalysts. *The Journal of Physical Chemistry C* **2020,** *124* (41), 22610-22618.

2. Sun, M.; Gottlieb, E.; Yuan, R.; Ghosh, S.; Wang, H.; Selhorst, R.; Huggett, A.; Du, X.; Yin, R.; Waldeck, D. H.; Matyjaszewski, K.; Kowalewski, T., Polyene-Free Photoluminescent Polymers via Hydrothermal Hydrolysis of Polyacrylonitrile in Neutral Water. *ACS Macro Letters* **2020,** *9* (9), 1403-1408.

3. Ghosh, S.; Mishra, S.; Avigad, E.; Bloom, B. P.; Baczewski, L. T.; Yochelis, S.; Paltiel, Y.; Naaman, R.; Waldeck, D. H., Effect of Chiral Molecules on the Electron's Spin Wavefunction at Interfaces. *The Journal of Physical Chemistry Letters* **2020,** *11* (4), 1550-1557.

4. Koplovitz, G.; Leitus, G.; Ghosh, S.; Bloom, B. P.; Yochelis, S.; Rotem, D.; Vischio, F.; Striccoli, M.; Fanizza, E.; Naaman, R.; Waldeck, D. H.; Porath, D.; Paltiel, Y., Single Domain 10 nm Ferromagnetism Imprinted on Superparamagnetic Nanoparticles Using Chiral Molecules. *Small* **2019,** *15* (1), 1804557.

5. Bloom, B. P.; Liu, R.; Zhang, P.; Ghosh, S.; Naaman, R.; Beratan, D. N.; Waldeck, D. H., Directing Charge Transfer in Quantum Dot Assemblies. *Accounts of Chemical Research* **2018,** *51* (10), 2565-2573.

6. Georgieva, Z. N.; Bloom, B. P.; Ghosh, S.; Waldeck, D. H., Imprinting Chirality onto the Electronic States of Colloidal Perovskite Nanoplatelets. *Advanced Materials* **2018,** *30* (23), 1800097.

7. Bloom, B. P.; Graff, B. M.; Ghosh, S.; Beratan, D. N.; Waldeck, D. H., Chirality Control of Electron Transfer in Quantum Dot Assemblies. *Journal of the American Chemical Society* **2017,** *139* (26), 9038-9043.

Before University of Pittsburgh

8. Schnitzler, E. G.; Seifert, N. A.; Ghosh, S.; Thomas, J.; Xu, Y.; Jäger, W., Hydration of the simplest α-keto acid: a rotational spectroscopic and ab initio study of the pyruvic acid–water complex. *Physical Chemistry Chemical Physics* **2017,** *19* (6), 4440-4446.

9. Ghosh, S.; Thomas, J.; Huang, W.; Xu, Y.; Jäger, W., Rotational Spectra of Two Hydrogen-Bonded Methyl Salicylate Monohydrates: Relative Stability and Tunneling Motions. *The Journal of Physical Chemistry Letters* **2015,** *6* (16), 3126-3131.

10. Ghosh, S.; Dixit, M. K.; Bhattacharyya, S. P.; Tembe, B. L., Franck–Condon Factors for Diatomics: Insights and Analysis Using the Fourier Grid Hamiltonian Method. *Journal of Chemical Education* **2013,** *90* (11), 1463-1471